

TOWARD OPTIMAL BEAM BRIGHTNESS FROM HIGH VOLTAGE DC PHOTOELECTRON SOURCES

A Dissertation

Presented to the Faculty of the Graduate School

of Cornell University

in Partial Fulfillment of the Requirements for the Degree of

Doctor of Philosophy

by

Jared Michael Maxson

August 2015

© 2015 Jared Michael Maxson

ALL RIGHTS RESERVED

TOWARD OPTIMAL BEAM BRIGHTNESS FROM HIGH VOLTAGE DC

PHOTOELECTRON SOURCES

Jared Michael Maxson, Ph.D.

Cornell University 2015

High voltage DC photoelectron guns generating beams of 100s of kV are the sources of choice for a wide array of linear accelerators. The beam's brightness is the principal figure of merit for DC gun-driven, GeV-scale synchrotron light sources and meter-scale ultrafast electron diffraction beamlines alike. Irrespective of the machine size, the beam brightness is limited by the parameters of the source: the extraction field and voltage, the drive laser 3D pulse shape, and the intrinsic momentum spread of the electrons leaving the photoemitting material. This thesis describes a new experimental DC gun and beamline constructed at Cornell which has demonstrated the state of the art in each of these parameters. Concepts to allow next generation photoguns to simultaneously achieve higher photocathode fields and total voltages are discussed. To conclude the thesis, a calculation of the fundamental limit on photoemitted beam brightness is given, which arises in cold, dense beams for which strong individual electron interactions result in beam heating.

BIOGRAPHICAL SKETCH

Jared Michael Maxson was born on July 23, 1987 in Mt. Vernon, Ohio. For the decade after that, he and his family executed a semi-random walk around the states of Pennsylvania and New Jersey. Settling down in Catasauqua PA, he played quite a bit of variably good rock and roll with variably talented bands, until he graduated college with a bachelor of science in physics from Lehigh University in 2009. Thinking himself a theorist, he arrived at Cornell to quickly find out that he was much better at measuring things, and should probably focus on that. One tour of the Wilson lab, Cornell's accelerator facility, was all he needed for a full conversion to accelerator physics. He obtained his Ph.D. from Cornell in the summer of 2015.

For my grandparents: Ward & Helen Maxson, Bobbie & Virginia Rogers, for their love,
lessons, and limitless support.

ACKNOWLEDGMENTS

There may come a time a graduate student's career in which she or he begins to feel that they are doing a job—that studenthood is gone and that merely a process separates them from their degree. I'm convinced that these people are missing out on a wonderful experience. I have learned much from my professors, but I have also learned much from the technicians and staff who helped me. I hope they both feel that I have been their student.

Specifically, there have been people who helped me become a better scientist: Ivan Bazarov, my advisor; Bruce Dunham, my informal advisor; Colwyn Gulliford, for whom no question was too dumb, and Adam Bartnik, for whom many questions are too dumb; and Luca Cultrera and Siddharth Karkare, perhaps two of the most peaceful personalities in this lab.

There have been many people who helped me to be more practical: Tobey Moore, perhaps the most handy and hardworking human I have ever met; Jeff Mangus, Mitch Bush, and Ed Foster, who could literally move anything; Karl Smolenski, who is both eminently practical and sincerely helpful; Xianghong Liu, a man who can do all mechanical jobs in the lab; John Dobbins, who could speak the language of any electronic device he ever met.

There have been people who just simply made me a better person: Ivan, Adam, Colwyn, Bruce, Karl. Outside of the lab: Matt Bierbaum, Nic Eggert, Sam Posen, Corky Wharton, Veronica Pillar.

My fianceé Erin Wissink , and my parents Phil and Rhonda deserve the most thanks of all.

The peculiarities of Wilson lab are only outclassed by the caliber of people who work

here. This is only a small subset of the people who actually deserve thanking. To see what I mean, stop by Wilson lab some Tuesday morning, and ask someone to show you around.

This work was supported by the National Science Foundation grants DMR-0807731, DGE-0707428 and PHY-1416318, as well as by the Department of Energy grant DE-SC0003965.

TABLE OF CONTENTS

Biographical Sketch	iii
Dedication	iv
Acknowledgments	v
Table of Contents	vii
List of Figures	ix
CHAPTER	
	PAGE
1 Introduction: The Shape of DC guns	1
1.1 The DC Photoelectron Source, Among Others	1
1.2 A Very High Voltage Diode	5
1.3 Electrode Material and Surface Preparation	12
1.4 Field vs. Voltage: Effects on Emittance Compensation	15
1.5 Overview of This Thesis	18
2 Design, conditioning, and performance of a high voltage, high brightness dc photoelectron gun with variable gap	21
2.1 Abstract	21
2.2 Introduction	22
2.3 Mechanical and HV Design	25
2.3.1 Segmented Insulator, Stalk, and Vacuum chamber	25
2.3.2 Electrode Design	29
2.4 Surface Preparation and Clean Construction	30
2.5 HV Conditioning	32
2.6 Optimized Simulated Emittance at Various gaps	37
2.7 Future Outlook and Conclusions	42
3 Efficient and accurate laser shaping with liquid crystal spatial light modulators	44
3.1 Preface: Laser shaping for photoinjectors	44
3.2 Abstract	46
3.3 Introduction	46
3.4 Holographic Shaping	49
3.5 Polarization Subtractive Shaping	53
3.6 A New Method for Refractive Shaping	55
4 Adaptive electron beam shaping using a photoemission gun and spatial light modulator	58
4.1 Abstract	58
4.2 Introduction	59
4.3 Polarization-Subtractive SLM Transverse Laser Shaping	62
4.4 Transmission of shaped laser light to the photocathode	68

4.5	Active electron beam feedback	71
4.6	Conclusions and Outlook	76
5	Measurement of the tradeoff between thermal emittance and quantum efficiency from a NaKSB photocathode near threshold	77
5.1	Abstract	77
5.2	Introduction	78
5.3	Measurement Methods	79
5.4	QE and MTE of NaKSB near threshold	82
5.5	Discussion and Conclusions	85
6	Fundamental Photoemission Brightness Limit from Disorder Induced Heating	87
6.1	Preface	87
6.2	Abstract	88
6.3	Introduction	88
6.4	Failure of Analytic models for Coulomb Collisions	91
6.4.1	Unbound Trajectories	93
6.4.2	Scaling with Density	94
6.5	Disorder Induced Heating	96
6.6	Conclusion	103
7	Conclusion: the Future of DC Guns	105
7.1	Higher Voltage <i>and</i> Field	107
7.2	Lower MTE	111
7.3	Conclusion	112
APPENDIX		PAGE
A	The Geometric Emittance of Needle Photocathodes	114
A.1	A Boundary Element Poisson Solver	115
A.2	Emittance as a Function of Tip Shape	118
References		124

LIST OF FIGURES

Figure		Page
1.1	a) A simple diode. b) A simple diode with a hole for beam transmission. c) The addition of an insulator (orange) and a photocathode (blue) with insertion mechanism make a viable dc gun.	7
1.2	High voltage photogun schematic for an on-axis insulator, including SF ₆ enclosure.	9
1.3	Photoguns with insulator symmetry axis perpendicular to that of the beam. a) A design utilizing a stalk. b) The so-called “inverted” design, which uses a high voltage cable, rather than a stalk. Though compact, the cable and small insulator will then directly limit the maximum voltage.	10
1.4	The in-vacuum protection rings in a segmented insulator intercept field emitted electrons (red arrow) before they strike the insulator body. Cornell design shown.	11
1.5	Data taken on a test field emission chamber, illustrating the performance difference between various metals and surface preparation techniques. Here EPION is a proprietary gas cluster ion beam technique, SS = stainless steel, EP = electropolish, HPR = high pressure rinse.	14
1.6	Data compiled from [1; 2] on maximum voltage attainable at a given gap for vacuum interrupters. Cornell MK I dc gun performance shown in red.	16
1.7	Emittance increases due to a) nonlinear correlations (space charge or geometric aberrations) or b) projected effects (chromatic aberration or space charge slice mismatch)	17
2.1	Top: A labeled 3D model of the gun, showing important components described in the text. Bottom: A labeled close-up of the cathode-anode gap.	26
2.2	Simplified HV model made in the software Opera 2D. Shown is the HV stalk, insulator, and guard rings for the gun operating at 750 kV. Color corresponds to the magnitude of the electric field in MV/m. For simplicity, this HV model is monolithic, rather than made of two insulator assemblies (as built), and similarly does not show the triple point protection rings. Note the tendency of field emission to come from the stalk at the base of the insulator, and that the field on the lowermost ring to be significantly higher than others. For this reason, the angle of the lowermost rings was increased from the nominal $\phi = 67.5^\circ$ to $\phi = 72.0^\circ$	27
2.3	The voltage applied to the gun during conditioning, corrected for the voltage drop across the processing resistor. Data points are colored for UHV (blue dot) and helium gas (green x) conditioning.	33

2.4	The total excess current as measured by a floating ammeter at HV (blue), and the excess current as measured by an ammeter on the resistor chain. The excess current is defined as the total current drawn minus the expected current from the insulator resistor chain. The floating ammeter saturates at a total current of $\sim 150 \mu\text{A}$, and a red x denotes a point where the ammeter was saturated and the max value of excess current that could be read at that point.	34
2.5	The vacuum pressure in the gun as measured by ion gauge during HV conditioning.	35
2.6	Upper pane: Stability test of the gun at various gaps. The overcurrent trip level is set to the minimum value for a given voltage, such that any $\sim \mu\text{A}$ scale current emission causes a trip. Thus, in this case, the trip rate is nearly equivalent to the discharge rate. After a trip, the vacuum was allowed to recover. Errors bars assume the trip process is random, Poissonian process. Lower pane: The same data, plotted as a function of the associated photocathode field.	36
2.7	Schematic of the Cornell ERL injector showing the location of the emittance compensation solenoids (S), the normal conducting buncher cavity (B), the 5 SRF cavities (1-5) in a single cryomodule, and the emittance minimization point (E). The overall length of the injector is 20 m.	38
2.8	Electric fields on axis for the gun with 50mm and 30mm gaps, as well as a hypothetical 500 kV, 70 mm gun.	38
2.9	Optimal fronts of the 100% normalized rms emittance for various gun gaps used as the source for the Cornell ERL injector plotted as a function of charge.	40
2.10	The core emittance of each solution shown in figure 2.9, computed in the manner described in the text.	41
2.11	Laser rms spot size used in the solution of 2.9 for both gaps.	42
3.1	Layouts for the A) diffractive/refractive and B) subtractive methods. For both, 532 nm light polarized in the plane of the page enters from the right, with a Gaussian spatial distribution. In A, after the SLM the beam is transported to either the camera (CCD), or the adjustable pinhole (APH) and power meter (PM) via a flip mirror (FM). See text for a description of B.	48
3.2	OMRAF efficiency vs. rms error for input beam sizes of $\sigma = 0.24 \text{ mm}$ (full SLM) and 0.8 mm ($1/3$ full SLM), for various target sizes. A) 2.5 mm target showing the SR/NR boundary (dotted line) and the offset from zero inside the SR. B-D) Example median-filtered CCD images, scaled to their respective global maxima.	50
3.3	OMRAF Efficiency vs. mix parameter for a $\sigma = 2.4 \text{ mm}$ input, and 2.5 mm output for $f = 30\text{cm}$ and $f = 55 \text{ cm}$. Inset: the average phase difference between adjacent pixels, $\langle \Delta\Phi \rangle$, versus m.	52

3.4	The subtractive method efficiency as a function of error using input rms size of $\sigma = 0.8$ mm and a $D = 2.17$ mm output flattop, with example CCD images. The intensity colormap is the same as in figure 3.2A.	54
3.5	A) The method of azimuthal particle binning and radial linking of particles within a bin in PTP. B) $D = 2.5$ mm intensity obtained with PTP prior to feedback. C) Intensity after PTP feedback.	56
4.1	532 nm diode laser light enters from the bottom along z and is polarized along x . A quarter wave plate and SLM act as a polarization rotator with spatial dependence, which shapes the light when used with a polarizing beam splitter (PBS). The surface of the SLM is then 4-f imaged onto an intermediate plane to preserve the beam divergence, and then this intermediate plane is imaged with a single long focal length lens onto either the photocathode or a CCD. An ultra high vacuum (UHV) mirror reflects light to the center of the photocathode. A dc bias of 300 kV accelerates the photoemitted electrons.	63
4.2	Coordinate systems of both the SLM and target planes, showing a possible skew transformation between the two.	64
4.3	A: The initial near-Gaussian unshaped laser profile, U . B: Shaped profile, a 2mm diameter flat-top, prior to feedback , I^0 . C: After 7 feedback iterations, the rms error is reduced to 10%. Each image is scaled to its respective maximum.	65
4.4	Layout of the electron beamline, including the photogun (purple equipotential lines), imaging solenoid, and BeO fluorescent viewscreen and fluorescence profiling camera.	68
4.5	A: Resultant beam profile when the flat-top shown in figure 4.3C is transported to the cathode and the beam imaged on the viewscreen. B: Beam result when a pinhole is placed in the image plane of the second lens downstream of the SLM. C: 1D profiles along the lines shown in A and B. D: Background of A, taken from yellow boxed region. E: Background of E, taken from yellow boxed region.	70
4.6	A: Laser target (see text for details) B: Final measured laser distribution C: Resultant beam distribution, rotated by 47 degrees in after acquisition, with no median filter.	72
4.7	A: Initial unshaped electron beam imaged on the fluorescent screen B: Final output of electron beam-based feedback, with no profiling of the drive laser. C: Progress of feedback vs. iteration. The distribution shown in B is circled.	73
4.8	A: Electron beam distribution created with beam feedback: A truncated Gaussian. B: A beam shape for a hypothetical photocathode with a local QE dip, thus requiring a local maximum on the laser power (electron beam shown).	75

4.9	A: Phase applied to the SLM to create the shape in B. The phase ranges from $[0, \pi]$. B: Electron beam distribution created with electron beam feedback, which does not directly profile the laser. The target distribution is that of figure 4.6A, scaled by the electron magnification.	75
5.1	Beamline used for the measurement. The high voltage dc gun, not shown, is directly upstream of the solenoid.	80
5.2	The measured MTE at various wavelengths as a function of field at the cathode surface. Both solenoid scan (solid) and EMS (dotted) are shown.	83
5.3	Quantum efficiency at various wavelengths as a function of the field at the cathode surface.	84
5.4	MTE at 4.4 MV/m, inferred from the straight line trend of solenoid scan data in figure 5.2, included with the solenoid scan measurement result at 2.3 eV. The red curve is Eqn. 5.2, assuming a Schottky reduction of the nominal work function of $\phi_{\text{eff}} = (1.95 - 0.08)$ eV. The blue curve is the simple model for large photon energy, $MTE = (h\nu - \phi_{\text{eff}})/3$	85
6.1	Final coupling Γ_f , vs initial coupling Γ_i , given by 6.8 (blue line), with $\Gamma_f = \Gamma_i$ for $\Gamma_i \rightarrow 0$ (red, dotted), and $\Gamma_f = 2.23$ for $\Gamma_i \rightarrow \infty$. Dots are simulation results of a fully contained, equipartitioned electron sphere, density $n_0 = 10^{20} \text{ m}^{-3}$, and initial temperatures between $kT=0.25 \text{ meV}$ and 20 meV . Squares are simulation results for multiple densities, where $kT_z = 0$, and $kT_x = kT_y$, and where Γ is calculated from the average of the three directions. Error bars are an estimate of the uncertainty in final temperature determination due to the residual oscillations, as in figure 6.2.	99
6.2	Temperature vs. number of plasma periods from treecode simulation using 10^5 contained electrons, and $n_0 = 10^{20}$ (top curve), 10^{19} , 10^{18} , 10^{17} m^{-3} (bottom curve), with zero initial temperature, $\Gamma_i \rightarrow \infty$. The equilibrium value predicted by 6.8, $\Gamma_f \approx 2.23$ is shown (dotted lines).	100
6.3	RMS velocity spread of a spherical bunch undergoing coulomb expansion, treecode data (circles), and prediction of 6.9. The inset shows the overall expansion of the bunch in normalized units, both analytic prediction (solid line), given by Gauss's Law, and treecode data (dots). Uniform bunches remain uniform, and the normalized bunch size $R(\tau)/R_0$ is independent of density.	103
6.4	Pair correlation function $g(r)$, computed at multiple simulation times for a bunch undergoing coulomb explosion. Both the initial "shock" profile and the freezing out of correlations despite increasing Γ is visible.	104
7.1	a) Example of the dual gap geometry, using two voltage dividing resistors, $R_1 < R_2$. b) The dual gap geometry does not easily lend itself to the off-axis insulator, as it requires another large electrode.	108

7.2	Example of a field enhancement feature, here shown for $\beta \sim 20$, and a nominal field of $E_0 = 3 \text{ MV/m}$. The base of the tip is not shown. Magnitude of the electric field and electron trajectories from various positions on the tip are shown.	109
A.1	The setup of the boundary element method. The method solves for unknown σ_i that generate required potential on the other segments. The needle geometry can be simplified into two simpler problems, wherein the middle diagram has an approximate analytic solution.	115
A.2	The geometries evaluated by the solver. Inset: closeup on the endcap, where a semicircular cap is deformed in several intermediate geometries to produce a square cap.	119
A.3	Left: Emittance versus flatness of the tip. $f/R = 0$ is round, $f/R = 1$ is flat. Right: Phase spaces at $z = 15 \mu\text{m}$ used to calculate emittances, with fully flat and fully round cases highlighted.	120
A.4	A set of focusing needle geometries used to mitigate the phase space curvature of figure A.3.	121
A.5	Left: Emittance at different evaluation planes for focusing geometries.	121
A.6	Field enhancement parameter β along the surface of flat and focusing tip.	122
A.7	Emittance at $z = 2 \text{ cm}$ for both flat and focusing cases, versus the maximum emission radius. The maximum emission radius is the radial position at the tip source above which particles are removed from the emittance calculation.	123

CHAPTER 1

INTRODUCTION: THE SHAPE OF DC GUNS

1.1 THE DC PHOTOELECTRON SOURCE, AMONG OTHERS

Direct current (dc) photoemission gun as the sources of electrons for larger accelerator structures have existed since the 1970's [3]. Owing to the ability of GaAs photocathodes to produce electron beams that are partially spin-polarized [4; 5], dc photoemission sources, the only sources with vacuum levels low enough for GaAs, enjoyed a long tenure as the electron sources of choice for nuclear physics experiments with polarized electrons [6]. In such experiments, which continue today most notably at the Continous Electron Beam Accelerator Facility at Jefferson Laboratory [7], the dc gun, the photoemission drive laser, and the beam they produce is not a focus of fundamental research, but rather is considered only a tool or technology to accomplish a task. Their intrinsic nature as a tool or technology has not changed. However, the interest in using dc guns for high average brightness photoinjectors to drive next generation synchrotron light sources such as Energy Recovery Linacs (ERL) [8; 9] and Free electron lasers (FELs) [10–12], has prompted a new interest in the fundamental performance maxima of dc guns relative to other types of sources. In both GeV-scale ERLs and FELs, bunched beams are typically produced from a single gun and accelerated in a kilometer-scale linear accelerator. The bunches typically contain 10s to 100s of picocoulombs (pC), and in the low energy portion of the accelerator (< 100 MeV) they

typically have millimeter-scale transverse and longitudinal size. In existing machines, the bunch phase space distribution never equilibrates or thermalizes throughout its transport, given that their total time of flight is microseconds, rather than the millisecond-scale thermalization processes (such as intrabeam scattering) beams undergo in storage rings [13; 14]. The focus of this work will be restricted to such non-equilibrium linacs.

The beam dynamics region of a dc gun is simply a vacuum diode, with a hole in the anode for the beam exit. As such, it directly contrasts with a radio frequency (rf) gun, where instead of a simple diode configuration, a resonant cavity supports either a standing or (less commonly) a traveling rf mode. Normal conducting rf (NC-rf) guns may support electric fields nearly an order of magnitude higher than dc guns, given that the fields are transient and do not have time to prompt breakdown processes inherent to dc guns [15; 16]. However, the ohmic losses in rf guns, particularly at high frequency (> 1 GHz) [17; 18], prohibit their continuous operation. Thus, from the beam dynamics considerations below, it will become clear that such NC-rf guns are more optimal than dc guns for applications only requiring high peak brightness, and low average beam brightness. Furthermore, the high vacuum level ($> 1 \times 10^{-9}$ torr) of NC-rf guns prohibits the use of high efficiency semiconductor photocathodes, and hence currently prohibit the production of polarized electrons. A continuous duty rf electron source would be one that is superconducting, in which the cavity wall losses are small, and for which the vacuum is naturally low ($< 1 \times 10^{-10}$ torr) due to the inherent cryogenic pumping. Such guns have been designed and built for high brightness applications [19; 20], but numerous technical details concerning the mating of a normal conducting semiconductor photocathode to the superconducting cavity wall prevent their widespread usage [21]. Given that this is simply a technological setback, it may be overcome in the future.

The brightness figure of merit has multiple forms. One may consider either the peak

or the transverse brightness, and one may consider the brightness of the beam in any Cartesian plane. For high average or peak brightness applications, it is the transverse (perpendicular to the beam direction, z) brightness that is most often considered, which can be defined rigorously as [22; 23]:

$$\mathcal{B}_{4D} = \frac{I_{av/pk}}{\epsilon_{nx}\epsilon_{ny}}, \quad (1.1)$$

where $I_{av/pk}$ is either the average current (the bunch repetition rate times the bunch charge) or the peak current (dq/dt for one bunch), and ϵ_{nx} is the root-mean-squared (rms) normalized emittance in the x direction. The emittance is a fundamental measure of beam quality, defined as $\epsilon_x = \frac{1}{mc} \sqrt{\langle x^2 \rangle \langle p_x^2 \rangle - \langle xp_x \rangle^2}$. Here $\langle \chi \rangle$ is the average of any quantity χ over the electron beam or bunch, using a one-particle distribution function in 6D phase space $\rho_6(x, y, z, p_x, p_y, p_z)$, where p stands for the mechanical momentum along a given direction. Thus, the emittance can be viewed as an area in projected (lower dimensional) phase space defined by the rms moments of the phase space density, wherein any linear correlation between the phase space coordinates is subtracted. Linear correlations of position and momenta are subtracted because they are of little consequence in accelerator systems with adequate focusing, in that an electron lens (such as a quadrupole or solenoid electromagnet) applies a linear force $f_x \propto x$, and hence any existing linear correlation can be removed at a desired target plane with an appropriate lens. However, any deviations from linearity in the phase space will cause the emittance to grow and, for example, will cause the beam waist size to increase. Thus, any phenomena that grows the emittance is a phenomenon that decreases brightness. Our definition of brightness not only carries information about the average density of the phase space, but also its particular shape, as this shape has implications for practical figures of merit such as x-ray brightness or collider luminosity, for example.

If individual electron-electron interaction is insignificant, and the beam self-forces only arise through a mean potential, Liouville's theorem requires that the 6D phase space density of a bunch (ρ_6) behaves as an incompressible fluid. This approximation of electron interaction as arising from only a mean potential is called the space charge approximation, and is valid for beams of bunch densities and temperatures such that the electron Debye length is much larger than the average interparticle separation. This is an excellent approximation for currently achieved photoemitted beams, as is shown in [13], and as will be discussed in detail later. Thus, the initial emittance at the source, governed by both the intrinsic Maxwellian momentum distribution of the electrons leaving the photocathode, as well as the real space laser intensity distribution (which effectively serves as the initial continuous spatial probability distribution for electrons), is the smallest it may ever be. Since in high brightness linacs these bunches never equilibrate or thermalize, one may suspect that this initial brightness could be preserved to a large degree with adequate transport. The initial emittance at the cathode, often called the thermal emittance, is therefore defined as:

$$\epsilon_{th} = \sigma_x \sqrt{\frac{\text{MTE}}{mc^2}}, \quad (1.2)$$

where here σ_x is the square root of the second moment of the initial laser transverse profile, and where MTE is the mean transverse energy of emission, and characterizes the transverse temperature of the photoemitted electrons. Thus, aside from comparing the relative performance of individual sources, we may define the quality of a source absolutely by considering the amount by which the source preserves the initial phase space density and shape.

The construction of dc guns has always sought to produce higher and higher beam

voltage. This is because the electron interaction force, which if left unchecked can induce various brightness diluting effects, decreases approximately as $F \propto \gamma^{-2}$, where γ is the normalized relativistic energy of the beam [13]. The emittance diluting effects of the self interaction include the production of nonlinear position-momentum correlations [24], as well as the “mismatch” of different *longitudinal* sections of the beam having different linear correlations, which when projected into the lower dimensional space of $x - p_x$, make the apparent phase space area increase [25; 26]. Thus, a higher energy source, such as an rf source, which in practice can achieve 5-10 times more beam energy given a sufficiently low repetition rate, is often the most desirable. However, it is clear from the above discussion that a dc gun is chosen out of necessity – some applications simply preclude the use of rf sources. Here we arrive at two central questions that drive this work: What is the ultimate brightness performance of a dc-gun driven high average brightness photoinjector, such as the one operated at Cornell [27]? What are the steps to achieve that brightness in practice?

1.2 A VERY HIGH VOLTAGE DIODE

Unfortunately, though the conceptual basis of dc gun is simply a vacuum diode, the final high voltage design is often relatively complex. In order to understand the structure of the modern dc photoemission gun, it is instructive to begin with a diode, and then to subsequently introduce complicating factors, such as the ability to use a retractable photocathode, or to reach several hundreds of kilovolts (kV) of beam energy.

A simple diode is shown in figure 1.1 a). In this cartoon, electrons emitted via an unspecified process at the negative electrode (cathode), are accelerated through a potential V , and are re-absorbed at the anode, typically at ground potential. A hole in the anode (figure 1.1 b) allows electrons with kinetic energy qV to escape the diode region where they

may be used or accelerated further. As electron beams must be transported in high vacuum, often preferably ultra high vacuum (UHV, $< 10^{-10}$ torr), the diode must be enclosed in a vacuum-tight structure. Furthermore, once this is done, the two electrodes must remain electrically isolated from each other. These two tasks are usually accomplished simultaneously using a vacuum-suitable insulator [28], such as alumina, which is brazed onto the metal conductors, as depicted in figure 1.1 c).

Photoemission can then take place using the metal of the electrode as the photocathode emitter, and it is not explicitly necessary to have a removable photocathode emitter assembly. This is a common practice in rf guns, either superconducting or otherwise [29]. However, pure metals or simple alloys often have a quantum efficiency, defined as the number of emitted electrons per incident photon, several orders of magnitude lower than the highest efficiency semiconductor photocathodes, such as GaAs:Cs [30], or multialkali photocathodes [30], such as NaKSB. Furthermore, as demonstrated in [30; 31], such higher efficiency cathodes can be operated at much longer wavelengths (visible) than metal photocathodes (UV), and thus their momentum spread upon photoemission can be much smaller, thereby increasing the initial brightness. Given that these cathodes rely on the presence of alkali metals in vacuum, they are very sensitive to vacuum contamination, and are not suitable for GHz scale NC-rf guns. Though dc guns do not increase the vacuum level during typical operation, one must still design the photocathode assembly to be retractable and replaceable because the photocathode efficiency may decay to unusable levels after long or heavy use [32; 33]. Thus, the photocathode assembly must be inserted into the cathode electrode using a vacuum translation arm, as depicted in figure 1.1 c) [34]. At this point, we have not specified the connection of the vacuum translation arm to the rest of the vacuum structure.

The insulator in figure 1.1 must be chosen to be large enough to withstand the high voltage required by the beam application. For bunch charges spanning the pC to nC range,

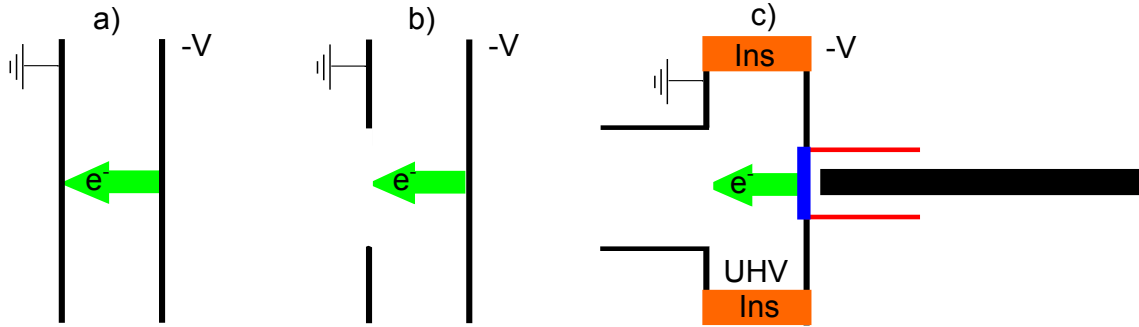


Figure 1.1: a) A simple diode. b) A simple diode with a hole for beam transmission. c) The addition of an insulator (orange) and a photocathode (blue) with insertion mechanism make a viable dc gun.

this voltage has generally been chosen in gun designs to be > 200 kV, an effort to make γ appreciably larger than 1. Though the dielectric strength of the insulating material (often alumina) is relatively large, in the range of 30 kV/mm (see Chapter 2), the fields at the insulator braze joint must be small enough not to put the joint at risk of stress or heating due to field emission. In order to accommodate 100s of kV, this requires increasing the length of the insulator in most gun cases to more than 0.5 m [35]. However, in the design of figure 1.1 lengthening the insulator also requires lengthening the cathode-anode gap, thereby reducing the photocathode field.

Reduction of the photocathode field has a significant effect on the maximum performance of the beam from the gun. For laser pulses that are much shorter in time than their spatial extent, it is the photocathode field that determines the maximum bunch charge than can be extracted from the gun. A pancake-like bunch of charge density σ at the surface of the photocathode will feel both the photocathode accelerating field (defined to be along $+z$), as well as force along $-z$ due to its image charge. Furthermore, as it travels away from the cathode, the bunch exerts a repulsive ($-z$) force on newly emitted electrons. When the sum of the space charge forces equals that of the applied photocathode field, charge emission stops. Thus, the maximum charge that can be emitted in a pancake-style bunch

temporal profile is $\sigma_{max} = \epsilon_0 E_c$, where E_c is the photocathode field, and ϵ_0 is the vacuum permittivity. This value, along with the MTE of the photocathode, can therefore define the maximum brightness for pancake bunches [36]. This result has recently been expanded to include the maximum current deliverable for “cigar-shaped” beams, in which the longitudinal size is comparable or larger than the transverse dimensions. Here, as above, the electric field is the parameter that determines the maximum extractable current [37].

Since the metallic electrodes themselves are less susceptible to damage from electrostatic stress and field emission, the “beam region” containing the electrodes is often spatially separated from the insulator. This is usually accomplished using a high voltage conductor, called a stalk, that passes through the elongated insulators and physically holds the cathode electrode. This complicates the diode structure greatly, in that the photocathode retraction mechanism must be lengthened significantly. This structure is then further complicated by the high voltage power supply (HVPS). To supply 100s of kV, a typical HVPS is a variant of the Cockcroft-Walton voltage multiplier circuit, and are designed to be operated in within a buffer gas environment, usually several atmospheres of SF₆ [38], to suppress arcing in the HVPS itself. Thus, the exterior of the gun where the HVPS mates to the HV surface must also be encased in dielectric buffer gas.

Figure 1.2 shows a version of the above design which, as in figure 1.1 c), uses an insulator with symmetry axis along that of the beam. This design has been used in an operational photogun for the Jefferson Laboratory FEL program [39]. The photocathode movement mechanism in this design is always in contact with the cathode electrode and thus is also biased to the cathode potential. Having the retraction mechanism biased to the high voltage has a number of practical drawbacks. First, the size of the SF6 enclosure must be increased to accommodate the movement mechanism, and secondly, the SF6 envelope must be broken each time a photocathode is installed or removed. The photocathode

movement mechanism of course may also be separated from the cathode potential via an additional insulator, as was done in the case of one 200 kV polarized electron photogun [40]. However, as the insulators often represent a significant fraction of the cost of the device, this practice is uncommon.

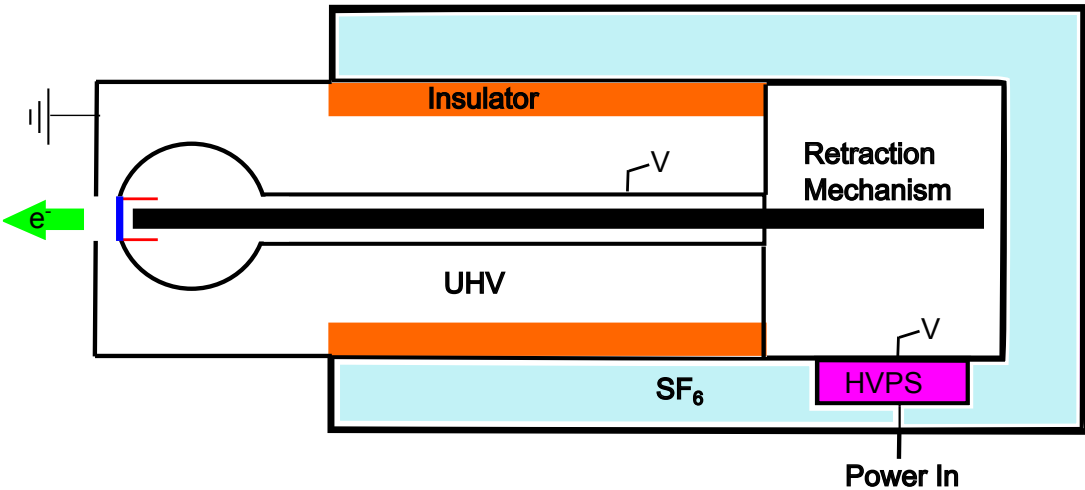


Figure 1.2: High voltage photogun schematic for an on-axis insulator, including SF₆ enclosure.

Placing the photocathode transfer mechanism at ground potential can be accomplished without additional insulators by relocating the single insulator so that it is no longer on the axis of the beam, such as shown in figure 1.3. In each of these designs, the load lock, the shorthand term for the photocathode loading and transfer mechanism, remains on the axis of the beam, but is attached to the grounded vacuum chamber. The insulators and high voltage are supplied to the cathode along a perpendicular axis. The second of these designs, called an “inverted” ceramic gun [41], is unique in that it does not require a stalk tube to hold the photocathode; the cathode electrode is held by the insulator itself. Furthermore, the SF₆ enclosure is limited only to the power supply. However, the shorter length of the insulator, and the requirement of power transfer via a high voltage cable (which itself is subject to breakdown) has limited the voltage capability of such guns to < 250 kV.

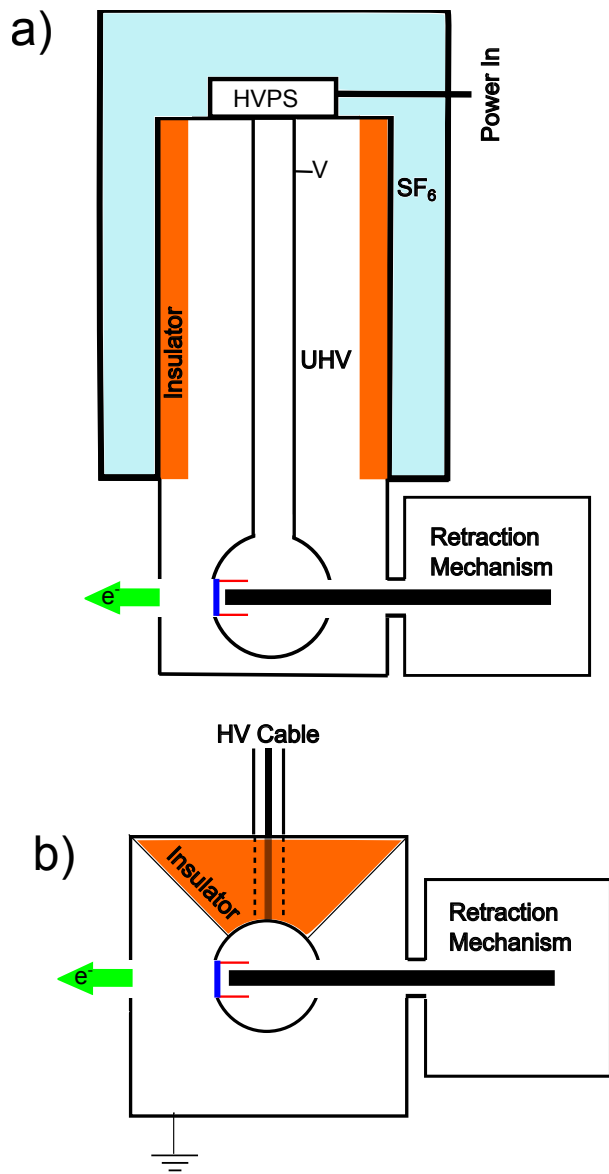


Figure 1.3: Photoguns with insulator symmetry axis perpendicular to that of the beam. a) A design utilizing a stalk. b) The so-called “inverted” design, which uses a high voltage cable, rather than a stalk. Though compact, the cable and small insulator will then directly limit the maximum voltage.

Despite its present voltage limitations, the inverted design is attractive as it greatly reduces the surface area of metal at high voltage. Furthermore, field emission from the stalk can strike the insulator, depositing charge and heating the insulator body. If the

charge deposited on the insulator from the stalk via field emission is large enough, the heating and dielectric stress can cause puncture the insulator. This puncture, often called “punch-through” is a vacuum to SF₆ leak, and prohibits further operation until the puncture can be repaired [42]. Prior to the recent development of shielded insulators [43], this was the major voltage-limiting phenomenon in all dc photoemission guns with a stalk.

The major development of [43] (see also [44–46]), was to introduce protective rings for the interior surface of the insulator. This used a segmented insulator, as opposed to a single-body insulator, in which each segment of alumina is brazed to a conducting ring which penetrates the vacuum. See figure 1.4. These rings brazed between segments allow the connection of larger guard rings in vacuum which shield the full interior surface of the insulator body from field emission. In the SF₆ environment, one may then attach a resistor chain along to the brazed rings to explicitly define the voltage across each segment. This design was shown to be successful, allowing beam operation at 500 kV without punch-through.

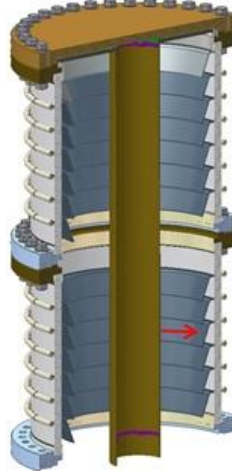


Figure 1.4: The in-vacuum protection rings in a segmented insulator intercept field emitted electrons (red arrow) before they strike the insulator body. Cornell design shown.

1.3 ELECTRODE MATERIAL AND SURFACE PREPARATION

The choice of electrode material and its surface finish can have a strong impact on the ultimate sustainable field of high voltage electrodes. It is well known that small protrusions on the surface of electrodes can enhance the local field above the nominal flat-surface value. The electrostatic field enhancement can be calculated for a number of protrusion shapes, but each essentially is an order-unity constant multiplied by the aspect ratio of the emitter, which is often in the range 10-100, but can be much higher [1; 47]. Hence, enhancement features arising from either the roughness of the material or particulate on the surface must be avoided. Often, for a well-prepared smooth surface that still field-emits at uncharacteristically low fields, values in excess of 100 can be calculated from the traditional Fowler-Nordheim analysis of the field emitted current vs. the applied field, though profilometry of the surface reveals that no such high aspect ratio feature exists on the sample. In these cases, one must also consider alterations to the workfunction due to impurities in the material [47–49], such as dielectric inclusions in the metal. These impurities vary with respect to forging processes, and thus can vary with material vendor. Coupled with the inherent variation in the work function of different atomically pure metals, the choice of metal for the dc gun electrodes is best determined empirically. This is usually done in a test high voltage chamber, using small test electrodes machined from the same material stock as the hypothetical gun electrode. A test high voltage chamber is often maximally simple: two removable planar electrodes (one isolated from the chamber ground with an insulator) in vacuum and a high voltage power supply. The gap between the cathode and anode is often variable, to allow the surface field be varied at a constant potential difference. The field emitted current is read as a function of the applied field using a picoammeter.

Aside from differences in material, a high voltage test chamber allows the testing of various surface preparation techniques. The goal of surface preparation techniques is twofold. First, the preparation should produce a smooth (e.g. polished, mechanically or otherwise) electrode surface. Secondly, the surface preparation should remove microparticle surface contamination, as microparticles could serve as field enhancement and emission sites. Options for surface smoothing for machinable metals include standard mechanical polishing (with silicon carbide or diamond paste or both), electropolishing for applicable metals, and gas cluster ion beam bombardment (GCIB) [50]. In GCIB, a cluster of ionized gas molecules (typically Argon) are accelerated to 10's of keV, and strike the metal surface, creating an impact crater. The craters often have a nm scale depth and diameter, and can be used to smooth materials down to the scale of the crater depth via removal of material [51]. The process has been previously shown to reduce field emission in SRF cavities [50].

To reduce the incidence of microparticle contamination, electrodes have a final surface preparation step performed in an air-filtered clean enclosure. Examples of this final step include dry ice blasting of the electrodes (a common practice for wafers in semiconductor devices) as well as high pressure rinsing (HPR) of electrodes, in which a jet of water at several hundred pounds per square inch purges adsorbed foreign material from the electrode surface [52].

A sample of data taken previously on a field emission test chamber at Cornell is shown in figure 1.5, adapted from data taken from [53]. While not exhaustive, the data is illustrative of the main points. First, it is clear that any smoothing surface technique increases the field emission threshold appreciably. Second, when the smoothing technique is coupled with the use of a microparticle removal step (here HPR) the performance can be improved further.

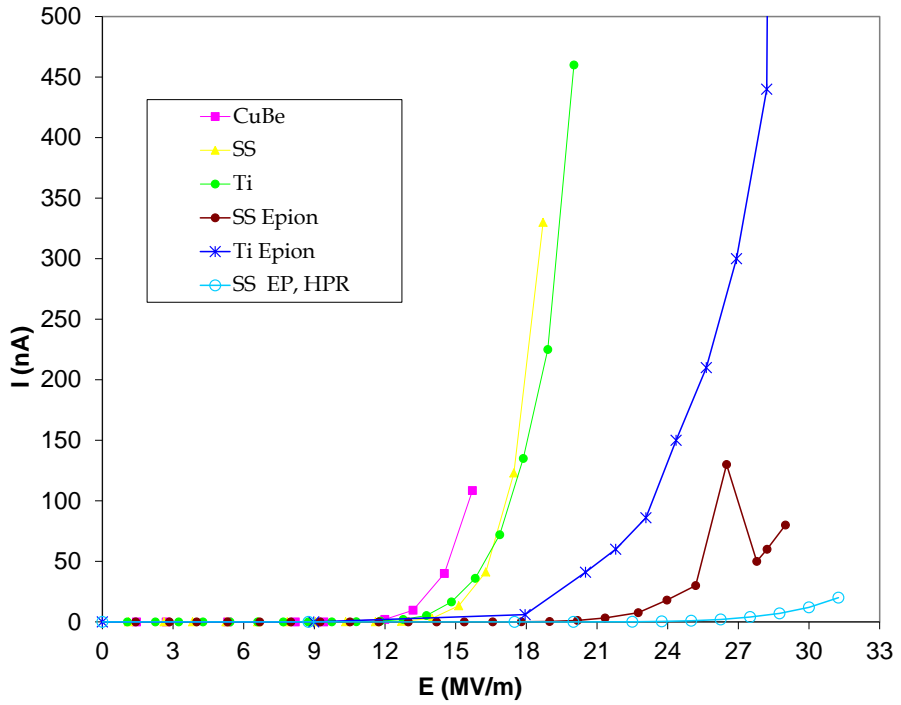


Figure 1.5: Data taken on a test field emission chamber, illustrating the performance difference between various metals and surface preparation techniques. Here EPION is a proprietary gas cluster ion beam technique, SS = stainless steel, EP = electropolish, HPR = high pressure rinse.

It is important to note here that the area of the test electrodes in such systems is often at least an order of magnitude smaller than the area of the metal at high voltage in an actual dc gun. The nature of vacuum breakdown with small versus large area electrodes can be very different [1; 47], and so the test chamber does not offer a reliable measure of the ultimate breakdown voltage sustainable by an actual dc gun. However, field emission is the first process (of several, depending on electrode area) to prompt breakdown in all high voltage systems. Thus, relative performance differences between metals or surface treatments that are measured in a field emission test chamber are likely to translate to performance differences in an actual photogun.

1.4 FIELD VS. VOLTAGE: EFFECTS ON EMITTANCE COMPENSATION

The above discussion has argued that maximizing both the photocathode field (to permit a larger charge density extracted) and the overall voltage (to reduce all effects of space charge) are both beneficial to beam brightness. With the use of a segmented insulator, it is now possible to have a voltage and a field constrained by the breakdown of the electrodes in the physics region. In practice, the complex phenomena associated with high voltage vacuum breakdown generally require that when maximizing one parameter, either field or voltage, one must reduce the other. Rather than justifying this statement based on a model including the many pertinent breakdown processes (including residual gas ionization, x-ray production, secondary electron generation [1; 47; 54], and others), it is more productive to analyze the empirical trends across many high voltage systems in use. In general, the number of high voltage dc photoemission guns that have ever constructed is small, and so we use an analog system for which many devices have been made.

Perhaps the best candidate for such an analog system is the vacuum interrupter, a commercially available class of high voltage switch, with electrode gaps (10s of mm) and voltages (200-600 kV) comparable to those used in dc photoemission guns. Furthermore, the electrodes are separated by a large insulator in the manner of figure 1.1c), and as such the vacuum interrupter resembles the high voltage test stand described earlier. The largest discrepancy between the two systems is the lack of a high voltage stalk in the vacuum interrupter. Thus, if using similar materials and surface preparation techniques, the performance in field and voltage of the vacuum interrupters (and other simple electrode geometries) can be viewed as an upper bound on the performance of the dc gun, considering that such systems has been extremely well studied and optimized [1].

Using data compiled from many high voltage test chambers, one can construct the expected maximum voltage as a function of the gap between two electrodes. This data was compiled in a seminal vacuum interrupter textbook [1], see also [2]. The data is shown in figure 1.6. For comparison, the operational voltage and gap of the first Cornell University dc photoemission gun [55] is also shown. It lies below the maximum performance of the simpler geometry by only ~ 50 kV.

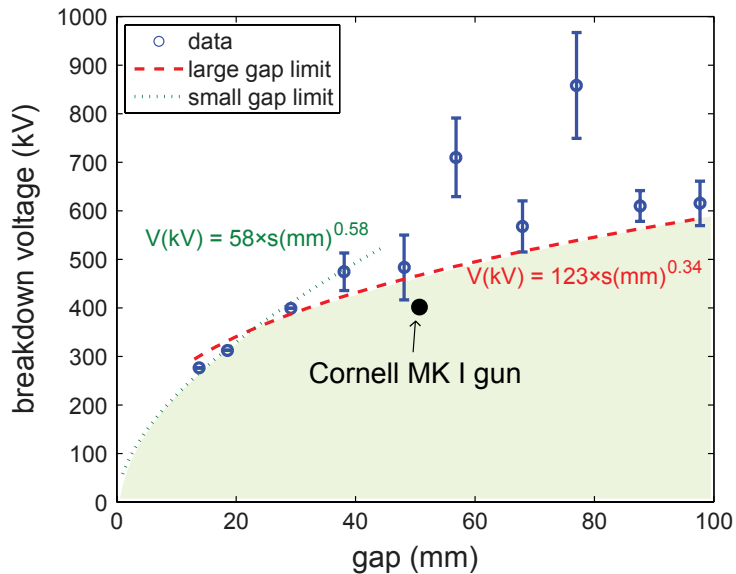


Figure 1.6: Data compiled from [1; 2] on maximum voltage attainable at a given gap for vacuum interrupters. Cornell MK I dc gun performance shown in red.

The maximum voltage V as a function of gap s is not linear, as would be the case if there were a single maximum electric field value that prompted breakdown. The host of effects mentioned above conspire to produce a scaling that is closer to $E \propto V^{-2}$, and thus the field must trade off strongly with the voltage.

Thus, the question arises: what combination of field and voltage in a gun yields maximal beam brightness in a dc gun photoinjector? The answer is not *a priori* clear. First, if the beam transport system is flexible enough, it is in general possible to eliminate

the effect of the bunch head-tail mismatch in the transverse phase space caused by space charge. This elimination process is called emittance compensation [25; 26], and uses a combination of constant lenses (solenoids) and time-varying lenses (rf cavities, which are also used for acceleration), to produce alignment of each longitudinal “slice” in transverse phase space at a given distance from the source. If the slice mismatch can be fully compensated, it is clear that maximizing the voltage is less important, and a larger photocathode field, which increases the initial density of the beam, is more desirable.

However, a lower energy beam for a given bunch charge is in general physically larger in size and likely contains a larger relative energy spread induced by space charge. The larger physical size may cause the lenses to induce nonlinear correlations in the phase space, called geometric aberrations. Also, given the dependence of a magnetic lens’ focal length on beam momentum, a larger energy spread in a lower voltage beam can induce a significant chromatic aberration, which increases emittance much in the same way that space-charge slice mismatch does. Furthermore, space charge can impart a nonlinear phase space correlation, which is difficult to remove. The general form of these effects on the phase space is summarized in figure 2.9.

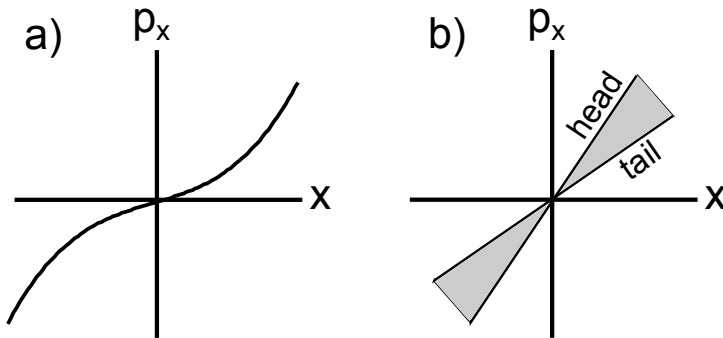


Figure 1.7: Emittance increases due to a) nonlinear correlations (space charge or geometric aberrations) or b) projected effects (chromatic aberration or space charge slice mismatch)

For voltages usually attained in dc guns (several hundred kV), the increase in emittance

from space charge slice mismatch (poor emittance compensation) and from geometric and chromatic aberrations can be of the same scale (~ 1 mm-mrad) [2]. Given the complex interplay between these effects, it is common to determine the best performance of an space charge dominated linac using a simulation optimization scheme. In such a scheme, a full space charge simulation of a parameterized beamline is used to model the beam dynamics, and an appropriate multivariate optimizer [56] adjusts the beamline parameters to simultaneously maximize and/or minimize a given set of figures of merit. For high brightness photoinjectors, it is common to minimize the emittance while maximizing the bunch charge, as an inverse relationship exists between them. To determine the optimal photocathode field and voltage, the gun geometry itself can be parameterized in the optimization, constrained to obey a realistic tradeoff between field and voltage [2]. A modified version of this procedure will be performed in Chapter 2.

1.5 OVERVIEW OF THIS THESIS

It is clear that the field and the voltage of the gun can heavily impact the beam brightness, and that in practice they will trade off with each other. When this work was begun, it was clear that Cornell would build another dc gun. Furthermore, given the desire for maximal voltage, it was decided that the gun would employ a segmented insulator design as shown in figure 1.4, given its previous success. Considering the utility of the grounded cathode translation mechanism, the overall gun geometry was chosen to be of the form shown in figure 1.3 a). Furthermore, to be able to experimentally map out the tradeoff between cathode field and voltage, a movable anode was designed that would allow the electrode gap to vary. The construction and commissioning of this new experimental gun, as well as its high voltage performance, is described in the next chapter. After the description of the

commissioning of the gun, we will describe multivariate optimizations of the gun with different gaps serving as the source for the Cornell ERL injector, to demonstrate the effect of the varying the voltage and the field on the brightness at a given charge.

Each of these optimizations, and the beam brightness in general, depend significantly on a larger set of gun parameters than just the shape of the fields. Chief among these parameters are the 3D laser distribution and the intrinsic photoemission momentum spread (MTE). The 3D laser distribution is significant to beam brightness in that it directly maps to the initial density distribution of electrons, and thus influences the space charge emittance dilution as the beam propagates. Secondly, with adequate space charge emittance compensation, the ultimate emittance performance of photoinjectors currently determined by the photoemission momentum spread, which is a function of both the laser wavelength and the photoemitting material properties.

Having determined the optimum performance of the gun and hypothetical photoinjector given current technology in simulation, advancements in the state of the art is demonstrated for these other gun parameters. First, a new high accuracy method for transverse laser shaping is demonstrated and applied to the electron beam, and compared with existing methods. Secondly, the measurement of near minimal thermal emittance (for a photocathode at room temperature) from the photoemitting material NaKSb is described.

Given the demonstrated ability to access small photoemission temperatures and high beam densities with semiconductor photocathodes, it now possible to produce electron beams that violate the space charge approximation, in that the Debye length may be on the order of the interparticle separation. In this case, the beam temperature is altered by the effects of strongly coupled individual electron interactions. Before concluding, the scale of this heating due to individual interactions is calculated for beams of varied temperature and

density. Finally, to conclude the thesis, possible avenues for next-generation guns to achieve both high photocathode field and accelerating voltage are described. With the exception of this introduction, conclusion, and the appendix, each chapter is adapted from previously published work. Deviations from the published work, and the published reference, is given at the beginning of each chapter.

CHAPTER **2**

DESIGN, CONDITIONING, AND PERFORMANCE OF A HIGH VOLTAGE, HIGH BRIGHTNESS DC PHOTOELECTRON GUN WITH VARIABLE GAP

Portions of this chapter (sections 2.1 to 2.5) were published in Reference [57]. Section 2.6 has been updated from the published version with additional data.

2.1 ABSTRACT

A new high voltage photoemission gun has been constructed at Cornell University which features a segmented insulator and a movable anode, allowing the cathode-anode gap to be adjusted. In this work we describe the gun's overall mechanical and high voltage design, the surface preparation of components, as well the clean construction methods. We present high voltage conditioning data using a 50mm cathode-anode gap, in which the conditioning voltage exceeds 500 kV, as well as at smaller gaps. Finally, we present simulated emittance results obtained from a genetic optimization scheme using voltage values based on the conditioning data. These results indicate that for charges up to 100 pC, a 30 mm gap at 400 kV has equal or smaller 100% emittance than a 50 mm gap at 450 kV, and also a smaller core emittance, when placed as the source for the Cornell energy recovery linac photoinjector with bunch length constrained to be < 3 ps rms. For 100pC up to 0.5 nC

charges, the 50 mm gap has larger core emittance than the 30mm gap, but conversely smaller 100% emittance.

2.2 INTRODUCTION

Direct current (dc) photoemission electron guns offer a robust option for photoelectron sources, with applications such as Energy Recovery Linacs (ERLs) [58], free electron lasers [39], ultrafast electron diffraction [59], and ultrafast electron microscopy [60]. In this paper we will focus on the design and use of dc guns for high brightness photoinjectors as sources for larger accelerators, such as next-generation light sources or colliders, for which beam brightness is a principle figure of merit. The technology for such guns was developed in the 1970’s [3], and the simple conceptual design has remained relatively unchanged.

A dc gun for a high brightness, high intensity photoinjector consists of a high voltage power supply (HVPS), usually some variant of the Cockcroft–Walton multiplier, supplying hundreds of kV to the high voltage (HV) surfaces of the gun. The power supply and outer gun structures at HV are often enclosed by a chamber pressurized with sulfur hexaflouride (SF_6) as a dielectric buffer gas to suppress arcing in the HVPS. The HV surfaces of the gun chamber are held off from the grounded chamber surfaces via an insulator structure. Inside the chamber, the cathode electrode is suspended in the chamber center via a support stalk, which also transmits the HV to the cathode electrode. An alternative “inverted” design exists in which the cathode electrode is supported by the insulator itself [41]. We will restrict our focus in this work to “standard” designs using a stalk, as to date higher voltage has been achieved with them.

The anode electrode is attached to the grounded surfaces of the gun chamber, onto

which the vacuum chamber of the beamline is connected. The rear of the gun, as defined by the beam direction, includes a vacuum load-lock system so that the photocathode structures, containing the active photoemitting surface, can be mounted in and removed from the cathode electrode. The photocathode can be illuminated with laser light from the front (opposing the beam), or from the rear (in the direction of the beam, termed “transmission mode” photocathodes).

The main failure mechanism of dc guns is field emission. Field emission can generate spurious beam, or the field emitted electrons can strike the insulator, causing a puncture, often called punch-through. The puncture is a vacuum to SF₆ leak, and precludes further operation until the puncture can be repaired. This method of failure will often limit the operational voltage. The field emitted electrons that cause punch-through usually originate from the HV stalk. Recently, a solution to the problem of punch-through was suggested in [45] (and associated references therein), in which the traditionally monolithic insulator is redesigned to be segmented. This design was repurposed for very high voltage photoemission guns based on the success of similar designs in lower voltage guns [61]. The interface of these segments is designed to allow the attachment of interior guard rings, which entirely shield the ceramic from any field emitted electrons. The design improvement proved robust, and the authors of [45] demonstrate stable voltage and beam above 500 kV without punch-through.

In this paper we report on the design and construction of a new high voltage dc photoemission gun at Cornell University also with segmented insulator and guard rings. As in the above result, we also report no occurrence of punch-through, despite applying conditioning voltages in excess of 500 kV in ultra-high vacuum (UHV). An additional novel feature of this gun is a movable anode, which adjusts the cathode-anode gap, and thereby changes the field on the photocathode. While the adjustable cathode-anode gap has been

previously realized to facilitate HV processing [62; 63], the importance of this parameter for beam emittance was realized in simulation studies [64] with realistic breakdown conditions later [2].

The cathode-anode gap is significant for beam dynamics because it defines the photocathode field. The photocathode field has been shown to be linearly proportional to the maximum achievable transverse beam brightness, qualitatively defined as the density of particles in transverse phase space [36]. The photocathode field affects the phase space density because a higher electric field on the photocathode increases the maximum charge density supportable without introducing time-dependent space charge instabilities, such as the virtual cathode instability [65]. A larger cathode-anode gap can in general support a higher total voltage, but a correspondingly smaller photocathode field than a gun with a smaller gap. Conversely, the non-linear (thus emittance-diluting) component of the space charge force will scale with the beam energy as $1/\gamma^2$, where γ is the normalized relativistic energy [13]. Furthermore, bunch dimensions tend to be larger at low energy making emittance worse due to aberrations. A larger voltage is desired to reduce these effects. Thus, a trade-off exists between higher voltage and higher photocathode field, directly controlled by the cathode-anode gap. A principle aim of the beam measurements with this gun will be explore these trade-offs.

We will begin our discussion of the new Cornell University gun with a description of its mechanical and HV design. We then describe the HV surface preparation and clean room construction techniques used. We then present data from the HV conditioning process, including the operational stability of the gun at various gun gaps. We stress here that conditioning is still ongoing, and thus these results do not indicate the final voltage of operation. Finally, we present results of an emittance optimization in which this gun for varied gaps and realistic voltage settings is simulated as the source of the existing Cornell

ERL photoinjector, described in great detail in [27], with optimization procedures similar to those described in [2].

2.3 MECHANICAL AND HV DESIGN

2.3.1 SEGMENTED INSULATOR, STALK, AND VACUUM CHAMBER

An overview of the gun and its major components is shown in figure 2.1. One of the most salient design differences between this gun and the previous Cornell dc gun [66] is the use a segmented insulator structure (figure 2.1[E]). The entire insulating structure is composed of two smaller insulator assemblies. Both insulator assemblies were manufactured by Friatec AG. Each insulator assembly has 7 segments, or 14 in total installed on the gun. Each segment is a ring of Al_2O_3 with an inner diameter of 435 mm, 50 mm tall, and 20 mm thick. The dielectric strength of the Al_2O_3 is quoted by Friatec to be beyond 30 kV/mm, with a resistivity of 10^{15} $\Omega\text{-cm}$ at room temperature. The top segment and bottom segment of each assembly is brazed into a 22.125" wire seal flange of 316 stainless steel.

A kovar ring is brazed in at the interface of two segments. In vacuum, the kovar ring allows the attachment of the aforementioned ceramic-guarding rings. These rings also extend outside the insulator body into the SF_6 environment. In the SF_6 , a resistor chain from HV (at the top) to ground (at the bottom) connecting to each kovar ring directly defines the voltage on all segment interfaces and inner guard rings. Kovar was chosen as the interface ring material for its similar linear coefficient of thermal expansion to that of the Al_2O_3 , so that the braze joint would be minimally stressed during vacuum bake-out.

The guard rings were made of copper due to its ease of machining and high thermal conductivity, thereby minimizing the heating of the ring and nearby braze joints from any

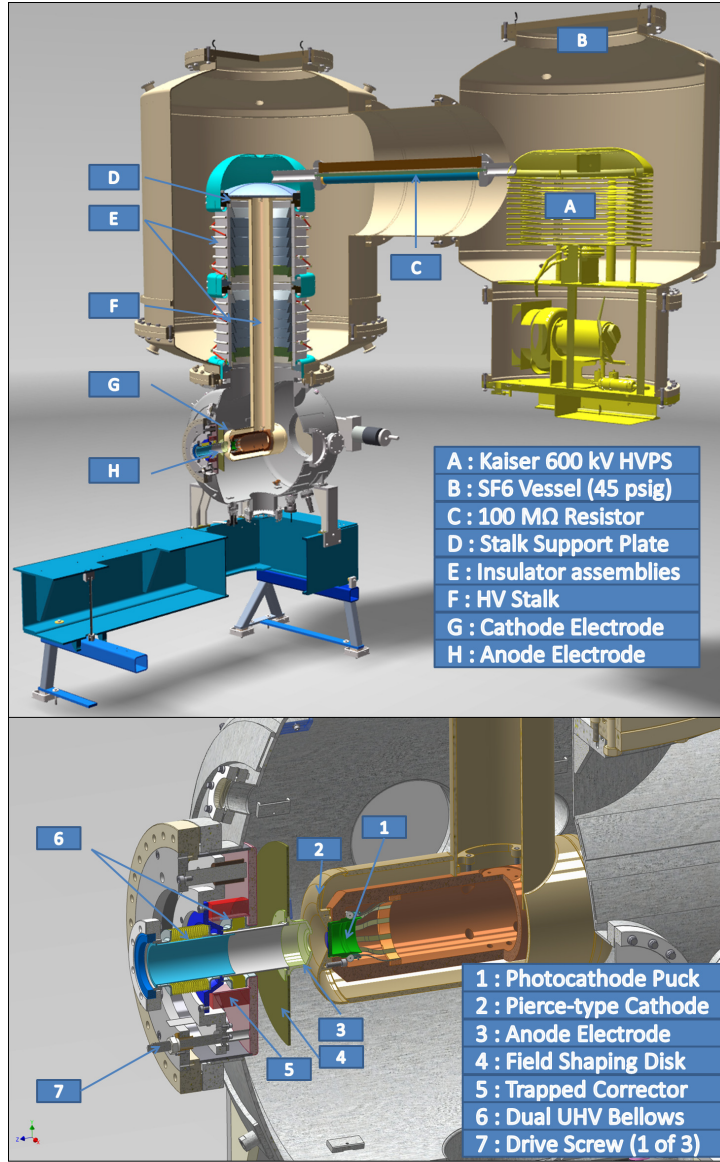


Figure 2.1: Top: A labeled 3D model of the gun, showing important components described in the text. Bottom: A labeled close-up of the cathode-anode gap.

stray field emission. A simplified high voltage model of the guard rings, insulator, and HV stalk are shown in figure 2.2. The angle of each ring with respect to the horizontal, $\phi = 67.5^\circ$, was chosen such that no path of field emitted electrons could strike the insulator surface, based on particle tracking. As visible in figure 2.2, the lowermost ring has an

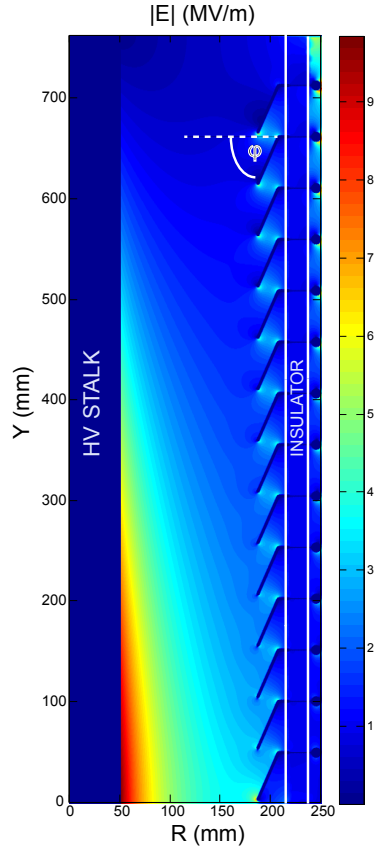


Figure 2.2: Simplified HV model made in the software Opera 2D. Shown is the HV stalk, insulator, and guard rings for the gun operating at 750 kV. Color corresponds to the magnitude of the electric field in MV/m. For simplicity, this HV model is monolithic, rather than made of two insulator assemblies (as built), and similarly does not show the triple point protection rings. Note the tendency of field emission to come from the stalk at the base of the insulator, and that the field on the lowermost ring to be significantly higher than others. For this reason, the angle of the lowermost rings was increased from the nominal $\phi = 67.5^\circ$ to $\phi = 72.0^\circ$.

elevated field as compared to all others, which could itself precipitate field emission. For this reason, the angle of the lowermost ring was increased to $\phi = 72.0^\circ$.

One of the most vulnerable locations with respect to field emission on any vacuum insulator is the so-called triple point junction, which is the interface between the stainless steel, ceramic, and vacuum. These junctions are shielded by additional triple point

protection (TPP) rings which attach directly to the interior of the flanges, and are also made of stainless steel.

The HV stalk (figure 2.1[F]) is a 1.25 m hollow cylinder with 125 mm outer diameter. The stalk center axis is co-linear with the insulator's center axis (in figure 2.2, the line at $R=0$), and is attached to a support plate (figure 2.1[D]) which rests on top of the uppermost TPP ring, a region of very small electric field, as shown by figure 2.2. As the stalk supports the cathode electrode, its height, angle with respect to the Y axis, and rotation angle about the Y axis are of direct importance for the symmetry of fields in the photoemission region. Thus, adjustment screws on the stalk plate permit the adjustment of height, both angular offsets from the y axis, and the rotation of the stalk.

The insulators and stalk rest on the gun vacuum chamber, which is held at ground potential, along with the SF_6 chamber walls. The gun chamber is a 600 mm diameter cylinder shell, 5 mm thick, with its symmetry axis along the direction of the beam. UHV pumping is provided by a two non-evaporable getter (NEG) modules (1300 l/s) and two 40 l/s ion pumps (not shown in figure 2.1). Each ion pump is placed behind a NEG module in a single assembly, so that any gas load produced by the ion pumps would first be pumped by the NEG modules before entering the gun chamber. Each of these “combined pumping” assemblies is attached to a 8” conflat flange on either side of gun chamber. A leak valve manifold (not shown in figure 2.1) with both a turbomolecular pump and a source of ultra-pure noble gas is attached to a UHV right-angle valve on the gun chamber for noble gas processing.

2.3.2 ELECTRODE DESIGN

The cathode electrode (figure 2.1[G]) design is identical to that of the previous Cornell gun [66], as this design was shown to be an effective balance between providing optimal focusing and high photocathode field strength while having minimal electric fields outside of the photoemission region [67]. Furthermore, this cathode design was shown to give excellent emittance for bunch charges up to 80 pC [27], for a gun operating at 350 kV. The cathode design is Pierce-type, with a focusing angle of 25°. The focusing introduced by this electrode angle serves to counteract the initial space charge expansion of an intense photoemitted beam.

The cathode electrode is made of vacuum remelt 316 LN stainless steel. It features a leaf spring assembly inside the cathode interior to hold and register a removable photocathode puck (figure 2.1[1]) in the center of the Pierce electrode. The back of the cathode electrode is terminated with a half-torus to keep electric fields minimal, with the torus hole permitting the transfer of photocathodes in and out of the interior holder.

The movable anode, shown in figure 2.1 (bottom) is the second major design difference between this gun and the previous Cornell gun. The anode electrode itself has the same angle of inclination as the Pierce focusing in the cathode. The anode electrode is attached to a field shaping disk, which helps smooth the electric fields on the face of the cathode just outside the photoemission region. The movement mechanism has a simple two bellows design, which allows movement without the force of the vacuum, as the total length of the two bellows is constant through the range of motion. The anode can change the cathode-anode gap from 20 mm to 50 mm. The movement is driven by three drive screws, which are constrained to drive together using a cog on each screw and a chain. The chain also allows for a simple measurement system for how much the anode has moved, as each

chain link corresponds to $120 \mu\text{m}$ of anode movement, which is the resolution of our measurement of the gap. A corrector magnet is usually installed in close proximity to the anode, for beam alignment in the downstream beampipe. As the moving mechanism extends well beyond the anode flange, a trapped corrector magnet pair was installed inside the mechanism itself, shown in figure 2.1[5].

2.4 SURFACE PREPARATION AND CLEAN CONSTRUCTION

The gun was constructed a first time in a clean room environment, but during the heated activation of the one NEG pumps, a nearby vacuum window cracked from thermal stress. This caused the de-sintering of NEG material into the vacuum chamber, and HV conditioning after the window repair was not successful. After this, all surfaces were re-cleaned and re-assembled. It is only this second assembly that we will describe in this work.

In general, we follow the procedures developed for cleaning superconducting radio frequency (SRF) cavities whenever possible for surfaces supporting high dc electric fields. Although field emission is a poorly understood process [58], it is well known that the condition of the HV surface in terms of both roughness and contaminants strongly affect the fields at which field emission or pre-breakdown activity begins. Both particulate contaminants and scratches or roughness can cause field enhancements which precipitate field emission or vacuum breakdown [1; 47]. Furthermore, both surface contaminants and dielectric inclusions in the metal can alter the work function of the material.

First, all metallic HV surfaces of the gun, including stalk, cathode electrode, copper rings, TPP rings, and anode, were mechanically hand-polished using silicon carbide. For the

stainless steel electrodes, an additional polishing with diamond paste is performed. After mechanical polishing, all stainless steel vacuum components (including chamber, stalk and electrodes) are baked in air at 400 C for 100 hours to reduce hydrogen outgassing. Then, a chemical polishing step was applied to all mechanically polished parts. For stainless steel parts (stalk, cathode electrode TPP rings), standard electropolishing was performed, removing 10 μm of material. For the copper rings, a weak citric acid etch was performed, as this was shown via interferometric microscopy to produce a surface with smaller RMS roughness than a more powerful copper etchant (such as nitric and sulfuric acid).

After surface treatment, all vacuum surfaces (including the chamber itself, but excluding the vacuum pumps) in the gun were high pressure rinsed with reverse osmosis purified water in clean room conditions equivalent to ISO 5 or better, to remove particulate contamination. The insulator itself was rinsed with \sim 300 psi water, whereas all metallic surfaces were rinsed with pressures \geq 600 psi, for approximately 3 hours per part. Both copper and TPP rings were rinsed on a separate rinse stand, apart from the insulator.

After a full air dry of all parts, the insulators were populated with rings manually. The cathode electrode was assembled on a test stand, and then suspended in the chamber via a temporary support. The insulators were installed on to the chamber and cathode assembly via a clean room crane. The stalk without top plate was similarly lowered through the insulators via the crane, and was attached to the cathode and temporary cathode support. Finally, the top plate was installed and attached to the stalk, allowing the cathode electrode support to be removed. Using surveying mounts installed in the photocathode holding structure, the height and angle of the electrodes were adjusted to be concentric with the axis defined by the anode and load-lock chamber flanges. The gun was then sealed and put under vacuum, and transferred from the clean room to the gun's diagnostic beamline. A

vacuum bake was performed at 150 C for approximately two days, followed by NEG activation at 500 C for 1 hour. The final vacuum prior to processing was 5×10^{-11} torr.

2.5 HV CONDITIONING

HV conditioning to date has continued over 150 hours, and is still ongoing. The gun was installed with a 600 kV dc power supply from Kaiser Systems, in an SF₆ environment at 3 bar. The gun is connected to the power supply via three 300 MΩ nichrome film resistors (figure 2.1[C]), each 1 m long, connected in parallel for redundancy. This processing resistor limits the current applied to the gun in case of a short through an arc in the gun. Each segment of the insulator has two parallel sets of 500 MΩ resistors, giving the insulator a total resistance of 7 GΩ, as verified by electrometer. Thus, a given voltage V applied by the power supply corresponds to a voltage across the gun of $(1 - 0.014)V$, as 1.4% of the supply voltage is dropped across the processing resistor.

A principle figure of merit during HV conditioning is the current drawn by stable field emitters or by fast emission events often called pre-breakdown events [47]. This current is read by a floating ammeter attached to the HVPS at high voltage. The floating ammeter is powered by infrared diode laser and photocell, via a fiber optic feedthrough in the SF₆ tank. Data from the ammeter is also transmitted via fiber optic cable. In principle the total current could be read from the power supply itself, however the power supply has an associated leakage current which makes this value difficult to interpret. However, this value is used to trip off the gun during a pre-breakdown event. The value was chosen such that the vacuum and emitted currents were within acceptable levels, as shown in figures 2.4 and 2.5.

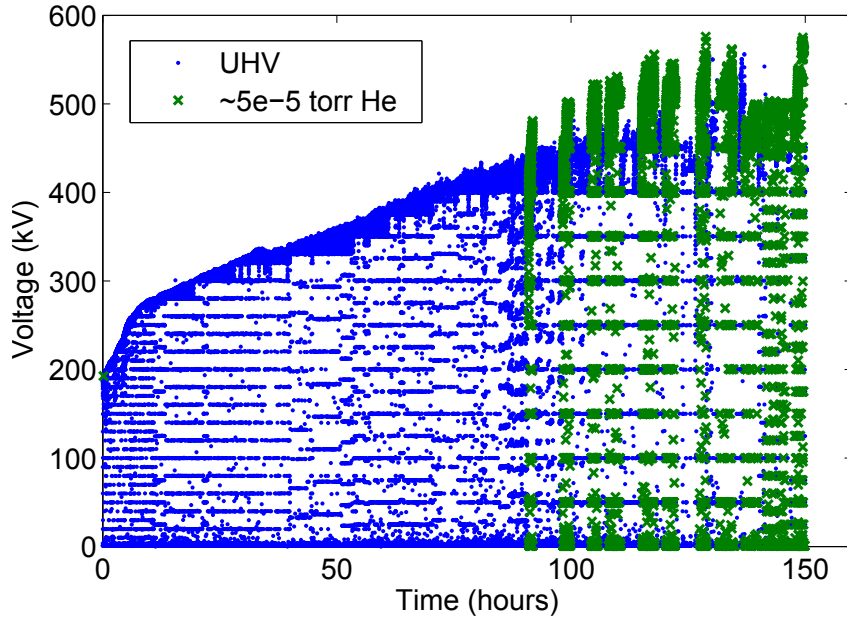


Figure 2.3: The voltage applied to the gun during conditioning, corrected for the voltage drop across the processing resistor. Data points are colored for UHV (blue dot) and helium gas (green x) conditioning.

The floating ammeter has a maximum readable current of $\sim 150 \mu\text{A}$. Furthermore, the insulator resistor chain has an expected current draw for a given voltage of several 10's to $100 \mu\text{A}$. Thus, there is limited headroom for the measurement of any excess current, defined as the difference of the expected current to the actual current, which decreases with increasing voltage. As such, many pre-breakdown events saturated the floating current monitor, and these events, along with the maximum value of total excess current that could be read at that time, are shown in red in figure 2.4. This saturation does not affect the reading of the resistor chain excess current monitor.

The conditioning was performed with a gap of 50 mm unless otherwise noted. The voltage across the gun was slowly increased to a state of pre-breakdown, most often to the point of tripping off due to the maximum current level, with subsequent attempts permitting higher and higher voltages before tripping. The first voltage at which vacuum

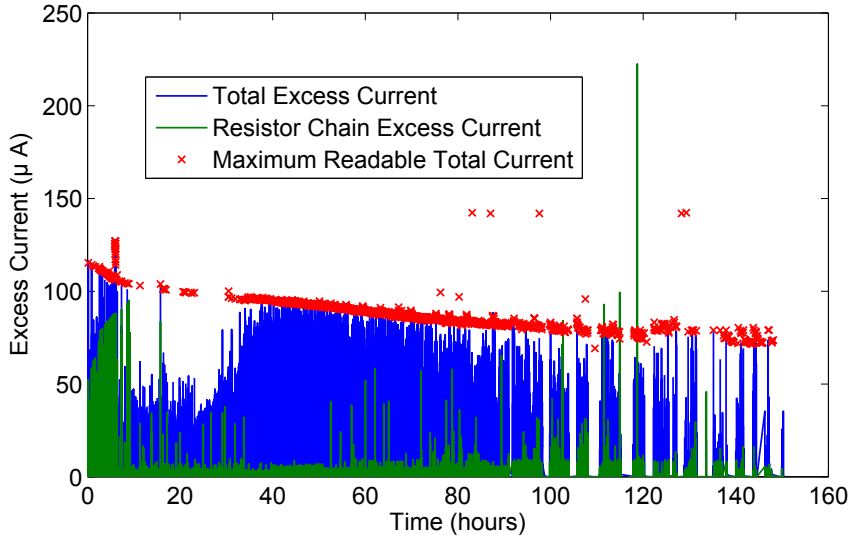


Figure 2.4: The total excess current as measured by a floating ammeter at HV (blue), and the excess current as measured by an ammeter on the resistor chain. The excess current is defined as the total current drawn minus the expected current from the insulator resistor chain. The floating ammeter saturates at a total current of $\sim 150 \mu\text{A}$, and a red x denotes a point where the ammeter was saturated and the max value of excess current that could be read at that point.

disturbance was detected was approximately 185 kV. Figure 2.3 shows that the majority of our voltage progress was linear with time. Spikes of the resistor chain excess current correspond to emission from the HV stalk surface to the copper insulator guard rings, and was treated with extra caution, as such emission had previously caused punch-through in unprotected insulators. Large emission to the rings in the first 10 hours of conditioning were found to abruptly cease, and the overall emission to the rings from then was usually less than $50 \mu\text{A}$.

After approximately 30 hours of conditioning, we found that the integrated gas load on the NEG pumps was nearing saturation. At this time we also observed a downturn in the slope of progress. We believed this to be due to the increased gas load in chamber, as residual gas that is not pumped can be ionized to initiate prebreakdown events, as demonstrated in [45]. This downturn in progress is seen as a small bump in figure 2.3.

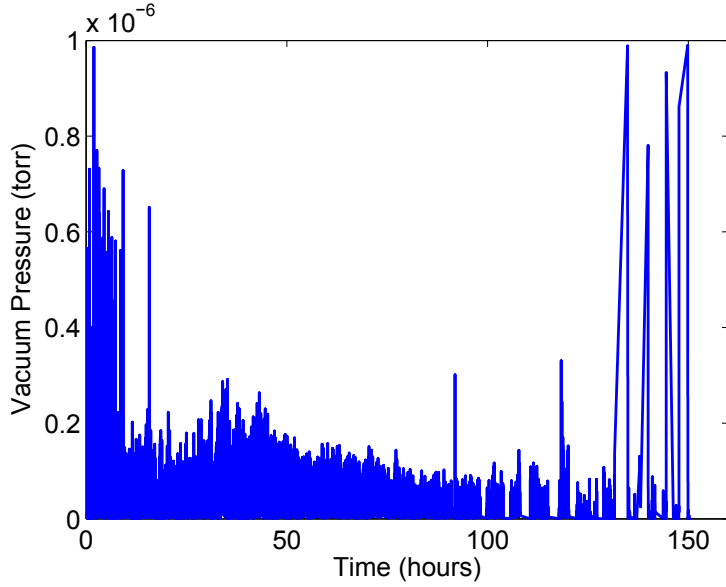


Figure 2.5: The vacuum pressure in the gun as measured by ion gauge during HV conditioning.

However, after NEG reactivation, the conditioning resumed without issue, and the slope of voltage progress increased back to its original value. Furthermore, after this time, the vacuum spikes (shown in figure 2.5) from each high voltage event began to decrease, likely due to the conditioning of the vacuum chamber walls.

At voltages above 400 kV, field emitters began to be created that could not be pacified by normal UHV conditioning. We found helium gas processing to be effective in suppressing these emitters (shown in green in figure 2.3) [39]. For gas processing, $\sim 5 \times 10^{-5}$ torr of helium gas was introduced into the gun via leak valve, with ion pumps off. The He is not pumped by the NEG. The gas routinely allowed a voltage setting above 500 kV, at which fields the more stable field emitters would show a gradual decrease in current drawn, and ultimately each one is eliminated. Conditioning then continued with alternating rounds of UHV and gas conditions, allowing us to apply conditioning voltages of > 500 kV in UHV.

After approximately 120 hours of conditioning, a stability test was performed for various

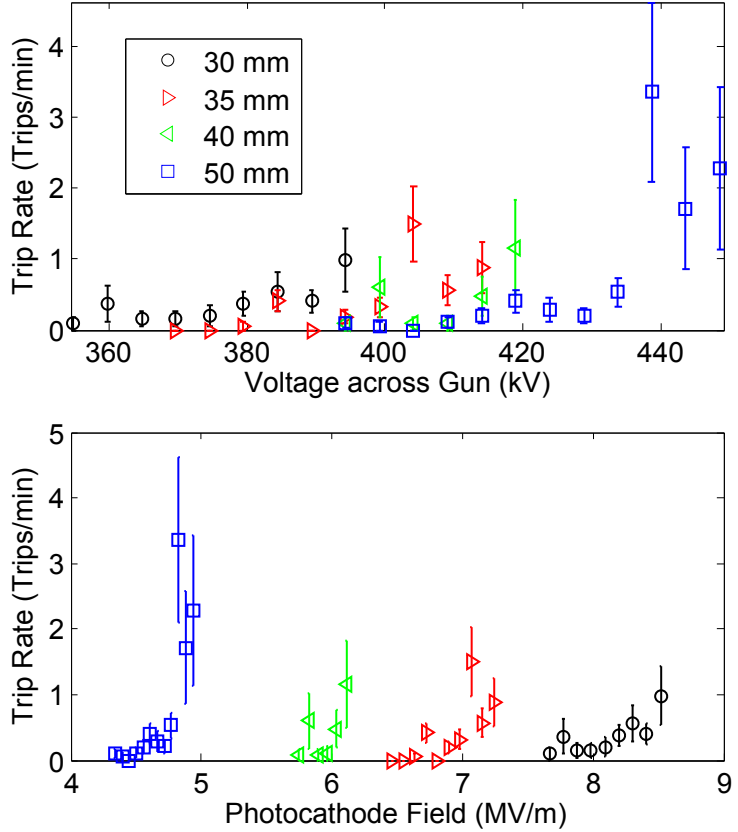


Figure 2.6: Upper pane: Stability test of the gun at various gaps. The overcurrent trip level is set to the minimum value for a given voltage, such that any $\sim \mu\text{A}$ scale current emission causes a trip. Thus, in this case, the trip rate is nearly equivalent to the discharge rate. After a trip, the vacuum was allowed to recover. Errors bars assume the trip process is random, Poissonian process. Lower pane: The same data, plotted as a function of the associated photocathode field.

gaps. The trip current level was reduced to the minimum for a given voltage, such that any discharge on the μA scale would cause a trip. The voltage was stepped up in 5 kV steps from a region of zero prebreakdown events to voltages at which the gun would discharge and trip off. After each discharge, the gun vacuum was allowed to recover. Approximately 15 min of on-time was spent per voltage per gap. We may get an estimate of the error associated with this discharge rate by assuming it is a Poissonian process, and thus for N trips, the associated error in the rate is $\propto \sqrt{N}$. This data is plotted as a function of the

applied voltage and the associated photocathode field achieved in figure 2.6. It should be emphasized that these discharges may be small enough that they do not preclude beam operation, as many discharges $< 10 \mu\text{A}$ have no effect on the vacuum level.

2.6 OPTIMIZED SIMULATED EMITTANCE AT VARIOUS GAPS

The highest voltage photoemission gun [46] used an increasingly larger cathode-anode gap ($> 100 \text{ mm}$) to achieve its highest voltages [45]. However, as per the discussion of the importance of the photocathode field in Chapter 1, this may not necessarily be optimal for beam brightness. To determine the optimal emittance performance of various gaps in a photoinjector, we follow a genetic optimization procedure very similar to that described in [2]. One dimensional field maps for the gun for both a 30 mm gap and a 50 mm gap are placed as the source of the Cornell ERL injector (shown in figure 2.7) in the space charge tracking software ASTRA [68], where the model features two emittance compensation solenoids, a normal-conducting buncher cavity, and 5 two-cell SRF cavities capable of producing a beam of up to 15 MeV. Both cavity types operate at 1.3 GHz. The on-axis field maps for each gun gap are shown in figure 2.8. The radial focusing force provided by the cathode is proportional to the derivative of the on-axis field, dE_z/dz , which is not only a function of the Pierce angle, but of the gap as well, as the Pierce angle is held constant at 25° in all maps. In all cases below, the mean transverse energy of the photoemission is 120 meV.

The gun voltage in the 30 mm and 50 mm case is fixed to 400 kV and 450 kV respectively. Whereas this setpoint is not currently stable with respect to discharge according to figure 2.6, conditioning progress continues, and we believe these values represent a good estimation of operational voltages. Along with the 30 mm and 50 mm

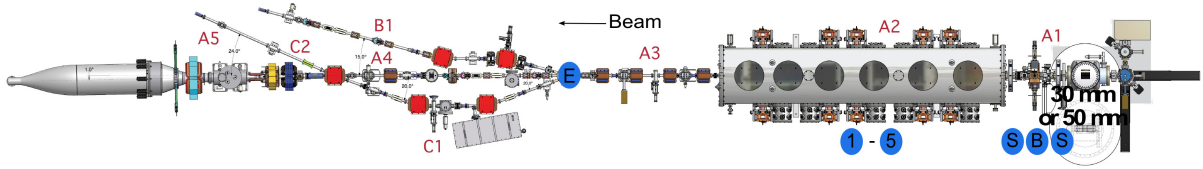


Figure 2.7: Schematic of the Cornell ERL injector showing the location of the emittance compensation solenoids (S), the normal conducting buncher cavity (B), the 5 SRF cavities (1-5) in a single cryomodule, and the emittance minimization point (E). The overall length of the injector is 20 m.

configuration, we also include a hypothetical 500 kV gun at 70 mm, to better determine the general trend in emittance with increasing energy and decreasing photocathode field, see figure 2.8. Note that each of these values roughly corresponds to the ultimate performance given by the vacuum interrupter data, described in Chapter 1, figure 1.6, illustrating a good correspondence between the systems. This correspondence suggests that the voltages at the different gaps attained in the gun in figure 2.6 are near ($\sim 50\text{kV}$) the ultimate breakdown limits.

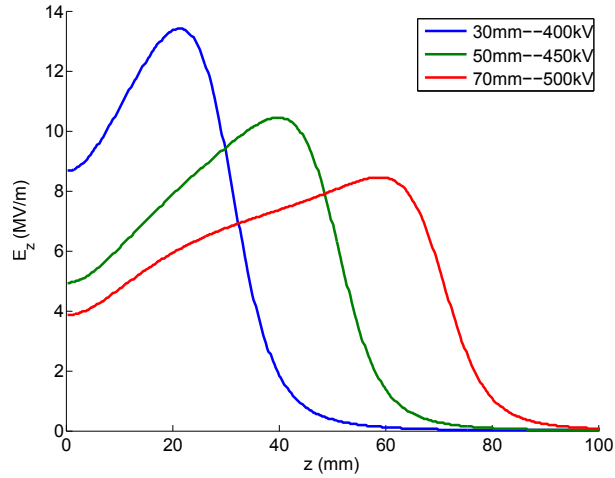


Figure 2.8: Electric fields on axis for the gun with 50mm and 30mm gaps, as well as a hypothetical 500 kV, 70 mm gun.

The optimization objective is the minimization of the root-mean-square (rms) normalized emittance, defined as

$$\epsilon_{nx,\text{rms}} = \frac{1}{mc} \sqrt{\langle x^2 \rangle \langle p_x^2 \rangle - \langle xp_x \rangle^2} \quad (2.1)$$

where m is the electron rest mass, and x and p_x are a transverse coordinate and mechanical momentum, respectively. The charge is scanned from 0 to 500 pC. Each of the elements downstream of the gun has a fixed position but varied amplitude, and for cavities, phase.

Optimizations ran until the optimal front of emittance vs. bunch charge reached sufficient convergence, wherein subsequent progress of optimization was smaller than the intrinsic noise in the front. In general, this involves optimizing each gap for roughly 500 generations each with population size of 75 simulations, all using 2×10^3 macroparticles. Finally, each gun gap optimization ran for 100 extra generations using 1×10^4 macroparticles, also with population size of 75 simulations. The laser temporal distribution was constrained to be 8 ps rms, but all other properties of the laser shape were allowed to vary in the same way as in [2]. All cavities and solenoids can only take values less than the maximum demonstrated in the Cornell ERL injector. For instance, the on axis field of the SRF cavities is constrained to be below 30 MV/m, and the buncher on axis field constrained to be below 5 MV/m. All final solutions end with beam energy above 10 MeV, owing to the beneficial relativistic cancellation of the space charge force.

Many interesting beam dynamics phenomena are present in the optimal solutions. We will give a brief overview of the main emittance results here. The optimized emittance as a function of charge for both gaps is shown in figure 2.9. For charges up to ~ 100 pC, the 30mm gap gun has nearly equal or slightly less 100% rms emittance than the other two higher voltage guns. For charges above ~ 100 pC, the higher-voltage (yet lower photocathode field) solution performs definitively better in 100% emittance. The behavior

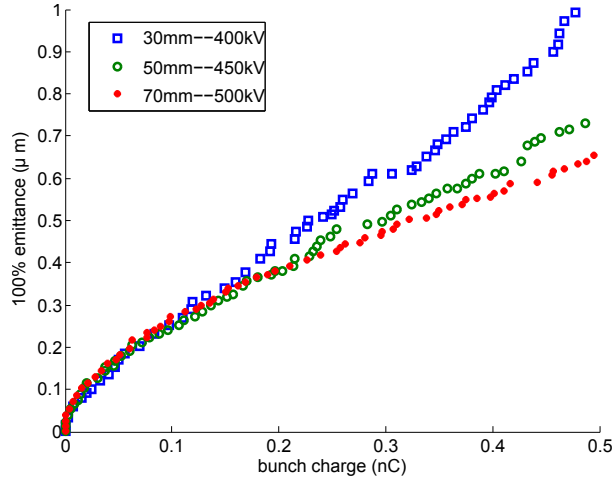


Figure 2.9: Optimal fronts of the 100% normalized rms emittance for various gun gaps used as the source for the Cornell ERL injector plotted as a function of charge.

that higher and higher voltage gives progressively less emittance reduction, i.e. diminishing returns with higher voltage, is one that has been noted before [2].

The opposite trend is true if one plots the core rms emittance of each of the above solutions. The core emittance can be computed simply from $\epsilon_c = 1/4\pi\rho_0$, where ρ_0 is the maximum transverse phase space density. The core emittance is then proportional to the peak (central axis) brightness. Furthermore, the core emittance is Liouville invariant (so long as there is no coordinate coupling) and thus insensitive to the shape of the fields, whereas the rms emittance is invariant only in the case of linear fields. The core emittance can be calculated by first computing the rms emittance vs. fraction function, $\epsilon_{x,\text{rms}}(f)$ for a given solution [27]. For a given fraction of the beam particles f , one searches all subsets of particles f such that the rms emittance is minimal, and this minimal emittance is then $\epsilon_{x,\text{rms}}(f)$. Then, the core emittance is given by:

$$\epsilon_c = \frac{d\epsilon_{x,\text{rms}}(f)}{df} \Big|_{f=0} \quad (2.2)$$

Thus, the core emittance can also be thought of as the emittance of the entire beam ($f = 1$) if the beam had a uniform phase space density equal to the density of the center of the actual distribution. The core emittance of each solution is shown in figure 2.10. Note that for all charges the 30 mm core emittance is smaller than the 50 mm core emittance. This is easy to understand if one considers that the larger photocathode field, E_{cath} , in the 30 mm gap case allows a larger charge density, σ , to be supported, $\sigma_{\max} = \epsilon_0 E_{\text{cath}}$, where a factor of two has been included for the image charge. This can also be seen in the rms laser spot size, plotted in figure 2.11, in that a smaller spot size for a given charge is used for 30 mm as compared to 50 mm.

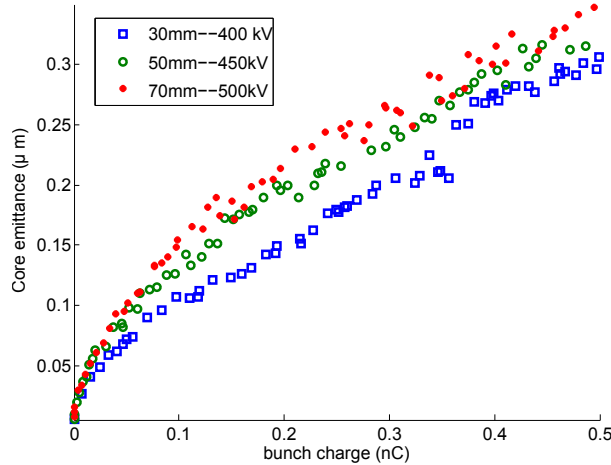


Figure 2.10: The core emittance of each solution shown in figure 2.9, computed in the manner described in the text.

Analytically explaining the trend of the 100% emittance in figure 2.9 is less simple than explaining the trend of core emittance, as each solution relies on both projected emittance cancellation as well as aberration minimization from all active beam optics and the space charge force. This complexity is illustrated by the nonintuitive fact that in the search for the lowest 100% emittance, the optimizer chose to produce higher on-axis brightness, and correspondingly *worse* 100% emittance compensation for increasing photocathode field.

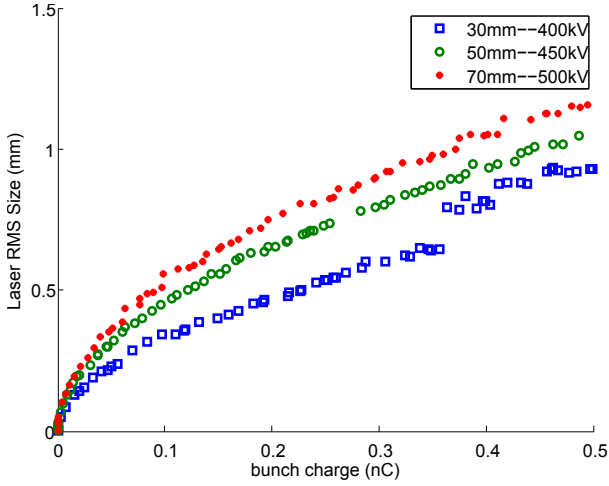


Figure 2.11: Laser rms spot size used in the solution of 2.9 for both gaps.

However, we can conclude that for charges up to 100 pC that the emittance compensation is not constrained by the gun voltage. In this charge range, a 30 mm gap with higher photocathode field outperforms a 50 mm gap or larger, as the 100% emittances are nearly equal, and the smaller gap core emittance is smaller. Above 100 pC, which gun gap to choose will depend on the application as to whether the 100% emittance or the peak (central-axis) brightness is the best performance metric.

2.7 FUTURE OUTLOOK AND CONCLUSIONS

HV conditioning will continue indefinitely as long as progress is seen. Beam with a temporary low power laser and multialkali photocathode has been demonstrated up to 400 kV at a 50 mm gap for emittance measurement commissioning. A subset of these measurements are described in Chapter 4. A mechanical problem with the loading and unloading of a photocathodes due to unwanted flexibility of the stalk support plate was repaired as of January 2014. This repair required venting the gun to replace this plate, and

thus required reconditioning back to 400 kV operation at 50 mm. Beam operation at this voltage both without measurable dark current and without measurable stalk vibration has been demonstrated. A subset of the beam measurements post-repair is given in Chapter 5; their success indicates that this stalk flexibility initial design issue was not fundamental to the overall gun design.

In summary, this chapter has described the implementation of both a segmented insulator and movable anode as additions to the traditional dc gun design. The high voltage performance presented further verifies that a segmented insulator is a robust solution to the problem of punch-through in dc guns. Furthermore, we have demonstrated the difference in utility of a gun with small gap and high photocathode field versus a larger gap and higher voltage gun. The small gap is seen to outperform the large gap for charges up to 100 pC as the source for the Cornell ERL injector, but for charges above 100 pC, the choice of gap will depend whether peak brightness (brighter with higher photocathode field) or full rms brightness (brighter with higher voltage) is more pertinent for the beam application. Finally, the inclusion of a movable anode on this gun will allow the direct exploration of these trade-offs using only one gun assembly. These results will have direct consequence for electron sources for applications ranging from mid-energy photoinjectors to electron diffraction beamlines.

CHAPTER 3

EFFICIENT AND ACCURATE LASER SHAPING WITH LIQUID CRYSTAL SPATIAL LIGHT MODULATORS

This chapter, except for the following Preface, was originally published as reference [69].

3.1 PREFACE: LASER SHAPING FOR PHOTONINJECTORS

In the previous sections, the emittance performance of the gun using various gaps has been determined. Each of the simulations relied on an ideal laser distribution, both temporally and spatially. The next two chapters will describe efforts to generate a high accuracy transverse laser shape.

The effect of 3D laser shaping on photoinjectors has been well studied. Prior to this work, much of the theoretical and experimental work has focused on the temporal dimension [30; 70]. The specific effect of the shape of the longitudinal laser pulse distribution is different in dc [55] versus GHz normal conducting rf (NC-rf) guns [70; 71], likely owing to the factor of ~ 10 difference in the photocathode field and correspondingly different early beam dynamics. Several schemes allow for the accurate shaping of the longitudinal distribution, such as applying a phase modulation in the spectral Fourier plane of a laser (i.e. the midpoint between two diffraction gratings) [70; 72], or by pulse stacking with

birefringent crystals [30; 73]. Each have been used in photoinjector experiments with success.

In the transverse plane, typically photoinjectors simply image a pinhole aperature on to the photocathode plane, yielding a sharp edged truncated semi-Gaussian (usually a truncated and transport-distorted TEM₀₀ mode) distribution on the cathode. For NC-rf injector, this has been the standard practice, and in the particular case of a very short temporal duration (~ 100 fs) in a NC-rf gun (sometimes called the “blowout” regime), the emittance is not very sensitive to the transverse distribution, but simply the rms size [71]. This is argued to be due to the extreme rearrangement of the electron beam distribution at the cathode owing to both the high accelerating fields in a NC-rf gun as well as the extreme self forces caused by the short pulse. However, for the case of a dc gun using longer pulse lengths (~ 10 s of ps FWHM), precise transverse shaping has recently been shown to have a significant effect on the photoinjector emittance for bunch charges > 100 pC [73].

A device called a liquid crystal spatial light modulator (SLM) is a promising tool used in other branches of physics (listed below) to create arbitrary transverse laser distributions. The device and its use will be described in detail below. At the time of this work, little was known about the practical efficiency and accuracy of the SLM for many of its possible modes of operation. In general, laser shaping for photoinjectors benefits from both high power efficiency and high accuracy (to eliminate nonlinear effects of space charge). Thus, to determine the applicability of SLMs to photoinjector research, we characterized a modern SLM’s performance in efficiency and accuracy for its various modes of operation in as general terms as possible, so as to be useful for the larger scientific community. The implementation of the SLM with an actual photogun will be described in Chapter 4.

3.2 ABSTRACT

Liquid crystal spatial light modulators (SLMs) have proven to be an invaluable optical tool for laser shaping, polarization control, and wavefront detection and correction. One particular method of SLM-based laser shaping, computer generated holograms (CGHs), has been shown to yield extended laser shapes with $< 10\%$ rms error, but conversely little is known about the experimental efficiency of the method in general. In this work we compare the maximum experimental efficiency and accuracy of three SLM laser shaping methods for input Gaussian beams and circular flat-top output beams: 1) the best currently known algorithm for generating CGHs, 2) polarization rotation-based intensity masking, and 3) a new adaptive algorithm for the computation of refractive phases for nearly radially symmetric shapes. We find that the polarization method performs comparably with CGHs, both having rms error $< 10\%$ with efficiency $> 15\%$. The refractive method is shown to have near maximal efficiency (92%), but with higher error ($\sim 16\%$). Generalizations to other shapes are made, and best practices for highest efficiency are described.

3.3 INTRODUCTION

The need for precisely shaped laser intensity distributions spans many disciplines in physics, including optical tweezers [74], cold atom traps [75–79], two photon microscopy [80], photoelectron sources and accelerators such as photoinjectors [36; 72; 81; 82], or electron photoguns for ultrafast electron diffraction [83; 84]. Whereas refractive beam shaping has been studied for many years [85], the most accurate laser shapes have been made by using other more recent methods [76; 77; 86; 87]. The most accurate transverse shapes that we are aware of have been made by a binary digital micromirror device producing a

dithered image, which is then low-pass filtered via a pinhole, producing less than 0.3% root-mean-squared (rms) error [86].

Liquid crystal spatial light modulators (SLMs) consist of an array of pixels with electrically addressable index of refraction along one axis. The pixel array imprints a spatially varying phase to incident light polarized along that axis. This imprinted phase can serve to form a diffractive far field image (by using a phase grating) or a refractive far field image (by using a smoothly varying phase). With the SLM as a pure phase modulator, the best shaping accuracy ($< 10\%$ rms error) for complex, sharp-edged shapes has been demonstrated using computer generated hologram (CGH) techniques in ref. [75], in which a lossy variant of the Gerchberg–Saxton (GS) method [77; 88] called the Offset Mix-Region Amplitude Freedom (OMRAF) algorithm is used. The method will be described in more detail below. The authors of ref. [75] cite a 24% efficiency for a given shape, but no other efficiency data is given. This parameter is of critical importance particularly for photoelectron sources, where the required shaped laser powers may be near the SLM damage thresholds.

In this work, we provide the first systematic experimental study of efficiency and accuracy from two of the most accurate liquid crystal SLM shaping methods: OMRAF holography, and SLM polarization rotation-based intensity masking (described below). Finally, we introduce a new adaptive algorithm for computing near maximally efficient refractive phases for nearly radially symmetric shapes.

The use of an SLM as a polarization rotator was first realized in ref. [89]. This method, modified for a reflecting SLM, is shown in figure 3.1B. Laser light polarized in the plane of the page is transmitted through a polarizing beam splitter (PBS) and is incident upon a quarter wave plate (QWP) with extraordinary axis at 45° with respect to the polarization.

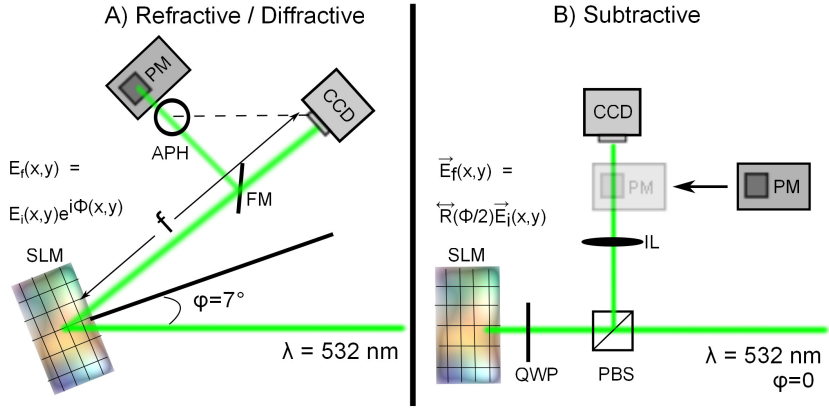


Figure 3.1: Layouts for the A) diffractive/refractive and B) subtractive methods. For both, 532 nm light polarized in the plane of the page enters from the right, with a Gaussian spatial distribution. In A, after the SLM the beam is transported to either the camera (CCD), or the adjustable pinhole (APH) and power meter (PM) via a flip mirror (FM). See text for a description of B.

A uniform phase offset $\Phi = \pi$ along the SLM axis (parallel to incident polarization), with a second pass through the QWP causes a polarization rotation of $\theta = \Phi/2$, and will thus cause the PBS to reflect all SLM-modulated light[90]. An imaging lens (IL) images the surface of the SLM onto a camera (CCD). For shaping, one can then reduce the phase Φ_{ij} of particular pixels, which will reflect less light to the CCD from those pixels, until the desired intensity distribution is obtained. We will refer to this method as “subtractive”, as the beam is shaped by the removal of intensity from the initial beam.

Both the subtractive method and OMRAF are fundamentally lossy algorithms, and both are capable of producing accurate, complex extended shapes with multiple feature size scales and hard edges [69]. However, in this work we restrict our focus to a hard-edged circular flat top, for two reasons. First, the circular flat top shape has applicability across all disciplines mentioned above. Second, the flat top shape allows easy generalization of results to other less trivial shapes, such as ring structures or extended semi-flat patterns of a characteristic size. However, the output diameter of the flat top D , as well as

input rms beam size σ , are both parameters to be optimized. Accuracy is measured by root-mean-squared error, explicitly defined as

$$\text{RMS Error} = \left(\frac{1}{N} \sum_{ij} \left(\frac{A'_{ij} - T'_{ij}}{T'_{ij}} \right)^2 \right)^{1/2} \quad (3.1)$$

where T is the target intensity distribution, A is the actual intensity distribution, and i and j are pixel indices. Here, priming corresponds to evaluating the distribution only where the *target* is nonzero (or not equal to the minimum offset in OMRAF), and N is the number of pixels in the non-zero (or non-minimal) target region. In realistic application, any intensity outside of the target region could be clipped using an aperture, and the target can be imaged to any size at the desired target plane. We define the efficiency of the algorithm as P'_A/P_0 , where P'_A is the actual output power in the non zero target region, and P_0 is the input power on the SLM, typically around 40 μW of 532 nm light in our case.

3.4 HOLOGRAPHIC SHAPING

The GS algorithm is an iterative Fourier transform method [91; 92] for CGH calculation which outputs the SLM phase required to transport a known initial beam to a target distribution, given an initial guess phase. It has been well documented elsewhere [75; 77; 91; 93; 94]. This algorithm has been improved significantly for use with current SLMs in two ways. The first principle improvement was the mixed-region amplitude freedom (MRAF) method of ref. [77] in which the target plane is split into two regions, the “signal” region (SR) and the “noise” region (NR). The solution is forced to converge to the target only in the SR, whereas the intensity may vary arbitrarily in the NR. A single dimensionless parameter, $m \in (0, 1]$ nonlinearly controls the amount of light in the SR vs.

the NR. As $m \rightarrow 1$, MRAF becomes GS, nearly 100% efficient in simulations with good convergence. The second improvement, ref. [75], was to offset the target by a small amount such that the target intensity is never zero. This method, called offset-MRAF (or OMRAF), was shown to both reduce simulation convergence issues [94] as well as to improve experimental shaping accuracy.

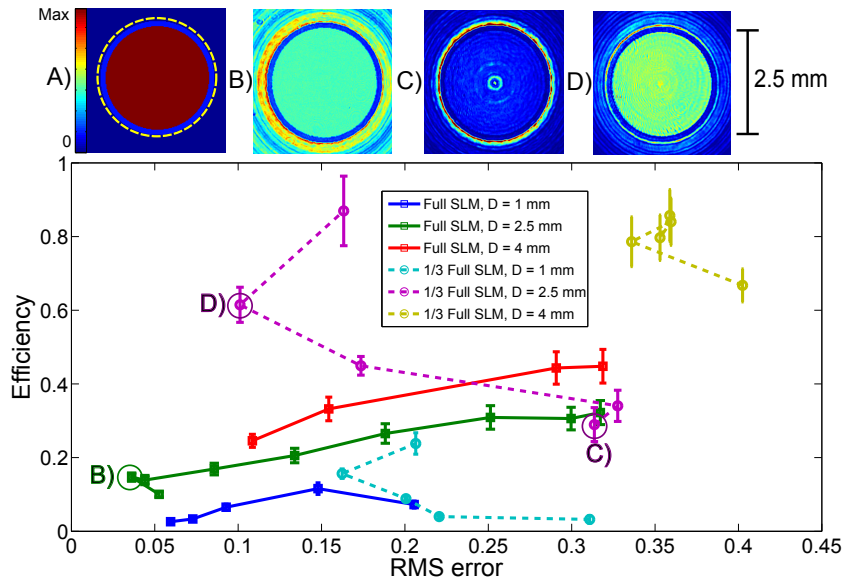


Figure 3.2: OMRAF efficiency vs. rms error for input beam sizes of $\sigma = 0.24$ mm (full SLM) and 0.8 mm ($1/3$ full SLM), for various target sizes. A) 2.5 mm target showing the SR/NR boundary (dotted line) and the offset from zero inside the SR. B-D) Example median-filtered CCD images, scaled to their respective global maxima.

Our setup for OMRAF implementation is shown in figure 3.1A. The SLM we used was a Hamamatsu LCOS-SLM X10468-04, a 600×792 pixel array with $20 \mu\text{m}$ pixel pitch. The near-Gaussian output of single mode fiber collimator was 4-f imaged into the SLM such that the SLM was approximately full, with a beam rms width of $\sigma = 2.4$ mm. We chose an offset value of $\Delta = 0.15 \max(T_{ij})$, and circular SR/NR boundary with radius 1.1 times larger than the target flat-top (see figure 3.2A). The mixing parameter m was varied between 0.4 (near optimal for accuracy) and 0.8. Contrary to most other laser GS layouts,

we do not use an imaging lens between the SLM and the target plane. We found that the exclusion of this lens did not affect simulated efficiencies or accuracies, but that it did make the OMRAF convergence more stable to the choice of initial guess phase. We uniformly use a zero guess phase throughout. Furthermore, with no lens, we also find that oversampling the SLM plane to increase the Nyquist resolution in the trapping plane [92] did not improve efficiency or error. Thus, each simulation point corresponds to an SLM pixel, which reduces computation time. For reasons described below, we do not offset the target in the trapping plane; the center of the SLM corresponds to the center of the flat top.

After 100 iterations of OMRAF, we display the calculated phase on the SLM, capture a median-filtered CCD image, and scale it such that the rms error with the target is minimal. We then perform the standard active feedback, where the OMRAF target is changed successively based on the error of the CCD image, until the error is minimized. Then, efficiency is measured by sending the beam through the adjustable pinhole, which allows us to clip all intensity in the NR. Error and efficiency results with OMRAF for an input beam of $\sigma = 2.4$ mm and various output sizes are shown in figure 3.2 (solid lines). We are able to produce a 3.6 % rms error flattop (figure 3.2B), which is on par with the best accuracy ever obtained using OMRAF [75; 76]. We find that efficiency generally increases with increasing target size, but that there is an optimal target size above and below which the error increases. Instead of efficiency increasing to near unity with $m \rightarrow 0.8$, as predicted by simulation, we find that efficiencies did not rise above 50%.

It is well known that liquid crystal SLMs have an imperfect diffraction efficiency that is a function of spatial frequency of the applied phase [95–97]. In this work, no complex correction scheme is applied [95]; we seek to increase the above overall efficiencies by reducing the spatial frequency of the applied phase. For a simple phase grating with a far field target, the diffraction angle is directly proportional to the spatial frequency. Thus,

spatial frequency is reduced by our choice of on-axis shapes, and can be reduced further with a larger distance to the CCD, f , or by making the ratio of input and output beam size closer to unity.

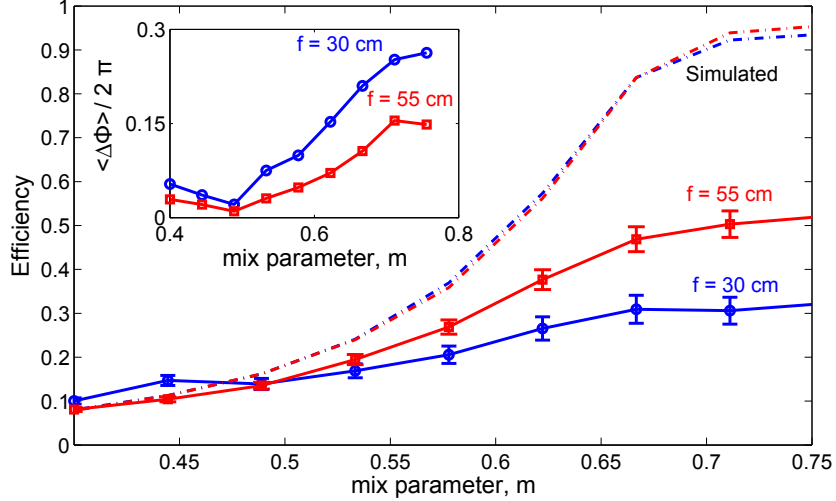


Figure 3.3: OMRAF Efficiency vs. mix parameter for a $\sigma = 2.4$ mm input, and 2.5 mm output for $f = 30\text{ cm}$ and $f = 55\text{ cm}$. Inset: the average phase difference between adjacent pixels, $\langle \Delta\Phi \rangle$, versus m .

Figure 3.2 also shows results for a beam of $\sigma = 0.8$ mm, or 1/3 of the full SLM size. We find a marked increase in efficiency for larger m , but at small m , a small beam size has larger error, due to far fewer active SLM pixels and a significant amount of zero-order light [92]. Only when the amount of light in the SR increases such that the zero-order can be masked does the error decrease to a minimum, in one case, obtaining 16% error with 87% efficiency.

The effect of increasing f has a similar effect on efficiency, as shown in figure 3.3, for two cases with $\sigma = 2.4$ mm, $D = 2.5$ mm, and $f = 30$ or 55 cm. Though the actual spatial Fourier transform of the applied phases is broad and difficult to interpret, we use the average phase difference between adjacent pixels as a measure of spatial frequency. We see in figure 3.3 that indeed the larger CCD distance does indeed correspond to a

smaller spatial frequency, and the increasing difference in efficiency between the two cases corresponds well with the increasing difference in spatial frequency. However, the larger f case was less accurate, having 1.7 times larger error, averaged over all data points. Thus, it is clear that the various tradeoffs between efficiency and error must inform all experimental parameters for OMRAF implementation.

3.5 POLARIZATION SUBTRACTIVE SHAPING

Conversely, the subtractive method has only two system parameters that control both the efficiency and error: the ratio of the input and output beam sizes (σ/D) and the intensity scale of the target image. For theoretically zero error with maximum efficiency, a target image with arbitrary scale should be rescaled by an amount α given by:

$$\alpha = \max \left\{ \frac{T'_{ij}}{I'_{0ij}} \right\} \quad (3.2)$$

where I_0 is the initial laser intensity distribution, and the maximum is taken over all the pixels on the nonzero (non-minimal) target region. Then, the desired initial guess phase function is given by $\Phi_{ij} = 2 \sin^{-1} \left[(\alpha T_{ij}/I_{0ij})^{1/2} \right]$. Increasing α beyond eq. 4.3 will increase the transmission, but also the error. This is particularly useful if the model of I_0 does not capture small features (ripples or fringes) present in the actual distribution. We find that the initial guess phase is not sufficient to immediately yield small error. A simple feedback algorithm is again applied, and runs until the error is minimized.

Using an input rms size of $\sigma = 0.8$ mm, we measured the efficiency versus ouput beam size to find its maximum. For a perfect Gaussian input beam, this value occurs at $D/\sigma = 2\sqrt{2} \approx 2.83$, whereas we measured an efficiency maximum at a ratio of 2.69, owing

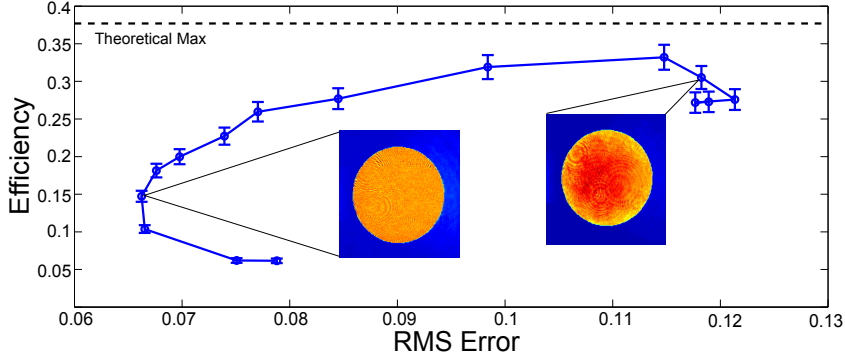


Figure 3.4: The subtractive method efficiency as a function of error using input rms size of $\sigma = 0.8$ mm and a $D = 2.17$ mm output flattop, with example CCD images. The intensity colormap is the same as in figure 3.2A.

to small non-idealities in our input beam. This corresponds to a flattop of $D = 2.17$ mm. With this diameter, α was scanned to map the efficiency as a function of the error, shown in figure 3.4. In each case, in the first iteration α is always computed by eq. 4.3, and it is only via feedback that alpha is increased or decreased to provide more or less intensity. Approximately 3% of the input intensity was unmodulated by the SLM, owing to imperfect polarization control or residual diffractive effects, and explains why the minimum efficiency does not have the best error. The theoretical maximum efficiency for Gaussian input shape and flat top output shape is 37%, and we are able to achieve 33 % with 11% error, and many patterns above 20% efficiency with less than 10% error.

The resolution of this method is set by only the SLM pixel size. The theoretical efficiency, which matches well to experimental values, is simple to calculate. For instance, the atomtronic OR-gate used in ref. [75] has a theoretical efficiency of $\sim 10\%$, which is nearly an order of magnitude larger than a simple binary intensity mask [75; 98]. Thus, the subtractive method may be a viable alternative to OMRAF for various detailed shapes.

3.6 A NEW METHOD FOR REFRACTIVE SHAPING

In principle, a refractive method of beam shaping, based solely on geometric optics, should be maximally efficient. It should also be more erroneous, owing to the lack of diffraction effects in the model. Analytic phase solutions exist for cylindrically symmetric refractive shaping, and a nonlinear partial differential equation exists for solving general 2D problems [85]. However, this equation is challenging to solve, and real initial laser distributions may not be sufficiently radially symmetric. We present a simple algorithm for refractive shaping with *nearly* radially symmetric distributions, where small asymmetries may be present.

The crux of the method is mapping the continuous beam shaping problem to a discrete particle tracing problem. The algorithm regards the input and target intensity distribution as probability distributions for the pseudo-random placement of N_p particles [99]. Both input and target distributions are populated, and then the particles in both are placed each N_b bins with respect to azimuthal angle, with the same number of particles in each bin, see figure 3.5A. Then, the input and target particles inside a given azimuthal bin are linked based on their radii; the maximum radius target particle in a bin is linked with the maximum radius input particle in the same bin. From this linking, one can calculate the angles $\theta_{x,i}$ and $\theta_{y,i}$ required to displace the input particle i to the position of the final linked particle i over a distance f . We then fit a continuous surface to these discrete angles, giving $\Theta_x(x, y)$ and $\Theta_y(x, y)$. In the geometric optics picture with small angle approximation, the correct phase must obey: $\nabla\phi = k_0(\Theta_x\hat{x} + \Theta_y\hat{y})$, where \hat{x} is a unit vector along x , and k_0 is the wavenumber of the light. To compute ϕ we instead solve Poisson's equation $\nabla^2\phi = k_0\nabla \cdot (\Theta_x\hat{x} + \Theta_y\hat{y})$, which removes any erroneous curl of the angle vector. This problem is analogous to the well-known “shape from shading” problem in optics. For more information on this solution method, consult ref. [100].

The method, which we refer to as the “particle to phase” (PTP) method, reliably reproduces the analytic solutions for cylindrically symmetric cases. However, implementation with a real beam and SLM often yields an asymmetric output before feedback, shown in figure 3.5, using a $\sigma = 0.8$ mm input beam and a 2.5 mm target diameter. Thus, PTP is used for feedback, with $N_p = 5 \times 10^4$ and $N_b = 400$. PTP was shown to reduce the RMS error from 27 % to 16%, shown in figure 3.5. The measured efficiency for this beam size was 92%. It is clear that PTP may be useful for shaping applications where efficiency is paramount. The method may be able to be extended to non-radially symmetric cases with a more sophisticated linking procedure. As above, the efficiency still depends on the spatial frequency, and so input and output beam sizes must be chosen to be comparable in scale.

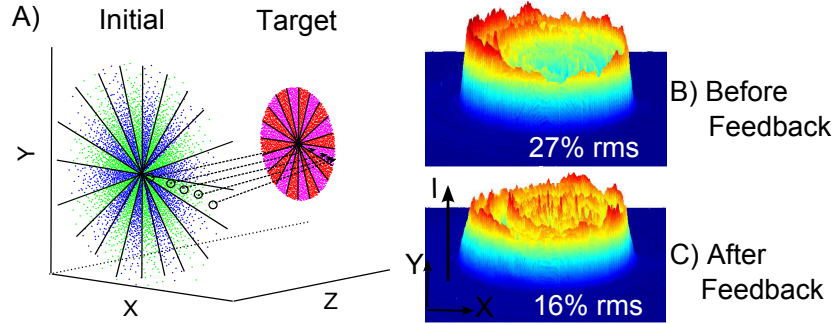


Figure 3.5: A) The method of azimuthal particle binning and radial linking of particles within a bin in PTP. B) $D = 2.5$ mm intensity obtained with PTP prior to feedback. C) Intensity after PTP feedback.

In summary, using a liquid crystal SLM, we have implemented both the best holographic method, OMRAF, as well as polarization subtractive beam shaping to compare how each trades efficiency for accuracy in making a circular flat top beam. We provide a simplified setup for OMRAF, and are able to obtain rms errors comparable with the best ever achieved with such SLMs. We explain the disagreement of simulation and actual efficiencies on the basis of a spatial frequency dependent diffraction efficiency, and show how it may be partially mitigated. Furthermore, we demonstrate the relative simplicity of the polarization

subtractive method, and show it to perform nearly as well as the holographic method for both error and efficiency. Finally, for applications where efficiency is the most important parameter, we have presented a new, simple algorithm for the calculation of refractive shaping phases for nearly cylindrically symmetric cases. This method provided near maximal efficiency (92%), with an error of 16%. We believe this work may serve as a guide for SLM practitioners across many disciplines in choosing experimental parameters for given constraints on either error or shaped laser power.

ADAPTIVE ELECTRON BEAM SHAPING USING A PHOTOEMISSION GUN AND SPATIAL LIGHT MODULATOR

This chapter was originally published as reference [101].

4.1 ABSTRACT

The need for precisely defined beam shapes in photoelectron sources has been well established. In this work, we use a spatial light modulator and simple shaping algorithm to create arbitrary, detailed transverse laser shapes with high fidelity. We transmit this shaped laser to the photocathode of a high voltage dc gun. Using beam currents where space charge is negligible, and using an imaging solenoid and fluorescent viewscreen, we show that the resultant beam shape preserves these detailed features with similar fidelity. Next, instead of transmitting a shaped laser profile, we use an active feedback on the unshaped electron beam image to create equally accurate and detailed shapes. We demonstrate that this electron beam feedback has the added advantage of correcting for electron optical aberrations, yielding shapes without skew. The method may serve to provide precisely defined electron beams for low current target experiments, space-charge dominated beam commissioning, as well as for online adaptive correction of photocathode quantum efficiency degradation.

4.2 INTRODUCTION

For any photoemitted electron beam, the three dimensional intensity distribution of the laser determines the initial density distribution of the electrons. The three dimensional distribution has been shown to have a significant impact on the emittance evolution of a space charge dominated beam [36; 71; 72; 82; 102], and is significant for various other applications such as conventional or cold atom electron sources for electron diffraction [83; 84], or next generation acceleration techniques [103; 104]. Furthermore, during high current photoinjector beam operation, the uniformity of the photocathode can be damaged by various phenomena including ion back-bombardment, high voltage discharge, or increased vacuum pressure, and may therefore change the electron density from a given laser shape as a function of time. Ion back-bombardment in particular will cause a spatially dependent decrease in photocathode quantum efficiency (QE), or the electron yield per incident photon [32]. Thus, precise shaping of the transverse dimensions for beam dynamics purposes should ideally also be adaptive to account for changes in QE.

With a few notable exceptions ([105], [83], and [106]), the transverse Gaussian output of drive lasers are most often shaped to a semi-flat-top shape via truncation with pinhole, and subsequent imaging of this pinhole onto the cathode. The notable exceptions include [105], which used a deformable mirror as an adaptive transverse shaper. With the use of a genetic algorithm to search for the mirror shape, a much improved semi-flat beam output was achieved. In [83] and [106], a spatial light modulator (SLM) was used with a modified Gerchberg-Saxton (GS) iterative Fourier transform method , e.g. [77; 88; 107] to make arbitrary beam shapes from a cold atom gas. However, in these cases, the beam profile is modulated by the density of the gas cloud, which alters the beam shape. Here again, an adaptive method which accounts for the spatially varying yield of electrons could be of use.

In this paper we demonstrate that using a commercially available liquid crystal spatial light modulator (Hamamatsu LCOS-SLM X10468-04) in the transverse plane to shape a drive laser, a low current beam from high voltage dc gun imaged onto a target plane can be shaped with high accuracy. Instead of computationally intensive iterative Fourier transform methods, we use a much simpler method of SLM-based polarization masking [89; 90], described in detail below. This method has been shown in [69] to have nearly equivalent performance in terms of accuracy and efficiency to the best Fourier space method. We demonstrate that this method has both the ability to offer a precise transverse shape for beam dynamics purposes, but also the adaptive capability to correct for imperfections in the quantum efficiency of a photocathode. Furthermore, we show that using a calibration to match the coordinates of the SLM with the coordinates of the target plane, the low-current target image can be shaped to undo any effects of electron optical aberrations.

Prior to using a SLM, we tested a variety of methods to shape our laser beam, but eventually found each to be unsatisfactory. We will describe each briefly here, so as to guide practitioners in the field. We tested a refractive beam shaper (Newport GBS-AR14), which takes in a Gaussian beam and produces a flat-top profile. This shaper worked very well when supplied with a good quality Gaussian beam with a precise initial size and divergence, but it was not realistic to use this in practice with our non-ideal input beam, and more importantly it does not allow for a tunable shape. See also [73]. Similarly, we also tested an engineered diffuser (Thorlabs ED1-C20) which produces a uniform flat-top speckle pattern for an arbitrary input beam. Because it produces the same output for almost any input, this is practically very attractive, but it suffers from too large of a beam divergence after the optic. Thorlabs was able to custom order smaller divergences, at the loss of some output beam quality, but not sufficiently small for our in-vacuum beam transport to the cathode. Furthermore, clearly this would not provide any adaptive capability. But, for

applications with a fixed desired shape with a smaller beam transport a custom ordered diffuser would be a very attractive option. Also, others have demonstrated light shaping using digital micromirror devices for beam instrumentation [108; 109]. Apart from SLMs, micromirror devices may offer another option for high accuracy [86] drive laser shaping.

The SLM method requires a single linear polarization of all input light. However, in the case of birefringent crystal temporal shaping there are multiple polarizations in the input pulse train [30]. However, we found producing one linear polarization after this temporal shaping to not be a problem in practice when only moderate overlap of the differently polarized pulses is employed. An example of such an overlap is shown in [110]. A linear polarizer rotated at 45 degrees to the optic axis of the birefringent crystals will produce linearly polarized light at the expense of 50% intensity reduction.

Liquid crystal SLMs have a damage threshold given by the onset of thermal effects. For pulsed lasers, the damage threshold of such SLMs is a function of both peak and average power, and is general not yet well studied. The vendor of our SLM has shown this model to withstand at least 2.6 W/cm^2 average power (with 101 MW/cm^2 peak power) without damage when illuminated with a 515 nm pulsed laser for 8 hours¹. While not exhaustive, these data suggest that current SLMs may be applicable to a wide array of photoinjectors.

In principle, a shaping method such as demonstrated in [105] using a deformable mirror, would not be sensitive to the polarization and may have a higher damage threshold. We attempted to use a deformable mirror (Okotech, 37 Channel, 15mm) to achieve a tunable beam profile. Contrary to [105], we found that the limited number of actuators in the mirror prevented us from having the necessary flexibility to go from an arbitrary and

¹LCOS-SLM X10468 series Technical Information 1, Hamamatsu Photonics.

non-ideal initial distribution to a desired output. More details about the deformable mirror are given in [101].

The organization of the paper is as follows. We will first give an overview of the SLM based high accuracy polarization-mask shaping method which was introduced in [90], first implemented in [89], and characterized in terms of efficiency in [69]. In this work we describe its implementation with an actual photogun [57]. We will then show that the transmission of the shaped drive laser to the cathode results in an electron beam shape of similar fidelity. Finally, we will show that using an active feedback with an unshaped beam, we can achieve similarly high fidelity beam shapes free from electron optical aberrations and QE non-uniformities present in our system.

4.3 POLARIZATION-SUBTRACTIVE SLM TRANSVERSE LASER SHAPING

A diagram of the setup is shown in figure 4.1. The liquid crystal orientation rotates in the $x - z$ plane as a function of the SLM setpoint, where z is the direction of propagation of the incident light. The orientation of the liquid crystal can vary from pixel to pixel. Thus, the SLM can apply a spatially varying phase to light polarized in the x direction. Each pixel is capable of applying a phase $\Phi_{ij} \in [0, 2\pi]$ to the incident light, where i and j are pixel indices. One can then compute phase profiles that shape the light in a refractive [85] or diffractive manner [92]. The best diffractive methods, variants of the GS holographic method, are lossy [75; 77]. For simple shapes, these losses are comparable to the method described below [69], which is computationally simpler.

With two passes through a quarter-wave plate aligned at 45 degrees to the initial

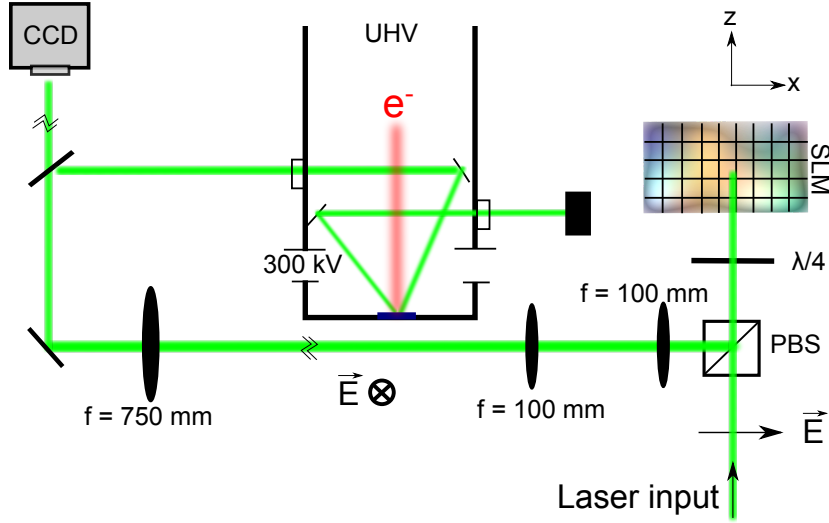


Figure 4.1: 532 nm diode laser light enters from the bottom along z and is polarized along x . A quarter wave plate and SLM act as a polarization rotator with spatial dependence, which shapes the light when used with a polarizing beam splitter (PBS). The surface of the SLM is then 4-f imaged onto an intermediate plane to preserve the beam divergence, and then this intermediate plane is imaged with a single long focal length lens onto either the photocathode or a CCD. An ultra high vacuum (UHV) mirror reflects light to the center of the photocathode. A dc bias of 300 kV accelerates the photoemitted electrons.

polarization, as in figure 4.1, the spatially dependent phase delay of the SLM is converted into a linear polarization rotation [89; 90]. Each pixel will rotate the phase of the incident light by $\theta_{ij} = \Phi_{ij}/2$. A polarizing beam cube is set to reflect light polarized perpendicular to the initial polarization. Thus, applying a phase of $\Phi_{ij} = \pi$ on a particular pixel will transmit all light incident on that pixel to the CCD or cathode. The intensity of the transmitted light is theoretically zero at a applied phase of zero. In real application, phase error in the SLM, imperfect polarization control of the input light, and spurious reflections from the beam cube caused by the former may contribute to a nonzero background intensity in the target plane. The smallest spatial scale that can be modulated is thus set by the size of the SLM pixel, which is 20 μm in our case. In general, we refer to this

method as the polarization subtractive method, as the laser is shaped by the spatially varying masking of the initial unshaped intensity. The efficiency of the method as compared to other SLM based laser shaping methods was studied in [69]. As such, our discussion of the efficiency in this work will be limited.

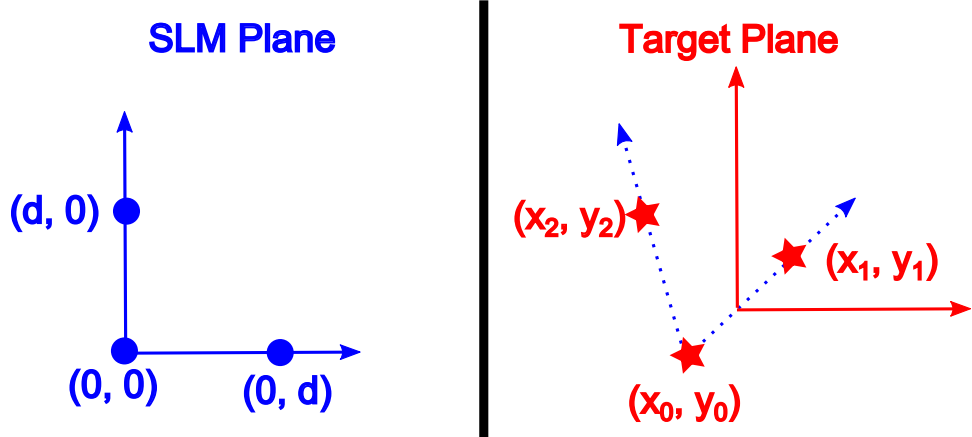


Figure 4.2: Coordinate systems of both the SLM and target planes, showing a possible skew transformation between the two.

To create an arbitrary laser shape, we must first establish the relationship between the coordinate system of the SLM and the target plane given by the properties of the optical transport from one to the other. This is done by setting the phase of individual SLM pixels to maximum transmission $\Phi = \pi$ and measuring the position of the resultant intensity maximum in the target plane, as shown in figure 4.2. In the case of pre-shaping the laser before transmission to the cathode, the target plane is the CCD. We account for a linear skew transformation between the SLM coordinates and the target plane, rather than simply rotation and magnification, anticipating that this method might accommodate various other linear optical aberrations between the SLM and target planes. We transmit light from only three pixels on the SLM, forming a right triangle: $(0, 0)$, at the geometric center of the SLM, and two points a distance d from the center. The position of the three points in the target plane we denote by (x_0, y_0) , (x_1, y_1) and (x_2, y_2) . From these points

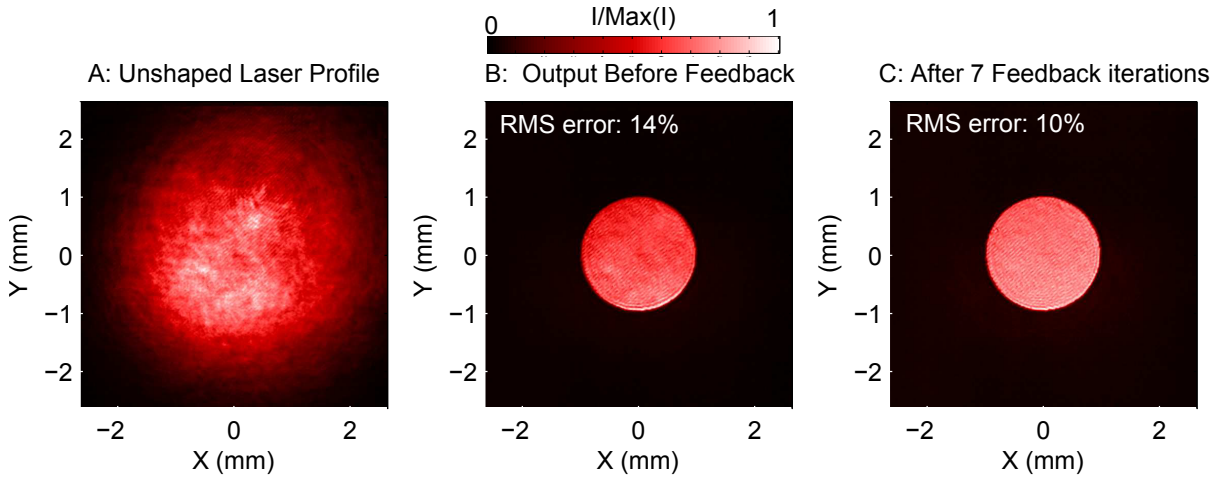


Figure 4.3: A: The initial near-Gaussian unshaped laser profile, U . B: Shaped profile, a 2mm diameter flat-top, prior to feedback , I^0 . C: After 7 feedback iterations, the rms error is reduced to 10%. Each image is scaled to its respective maximum.

we can determine the general linear transformation that takes any point on the SLM (x_{SLM}, y_{SLM}) to the corresponding point in the target plane (x_T, y_T) , assuming only that the transformation is linear:

$$\begin{pmatrix} x_T \\ y_T \end{pmatrix} = \begin{pmatrix} x_1 & x_2 \\ y_1 & y_2 \end{pmatrix} \begin{pmatrix} x_{SLM} \\ y_{SLM} \end{pmatrix} \frac{1}{d} + \begin{pmatrix} x_0 \\ y_0 \end{pmatrix} \quad (4.1)$$

Once this transformation is established, we generate an arbitrary target laser intensity distribution, defined in the the target plane coordinates. Then we apply the inverse of the transformation in eq. 4.1 to generate the required target in the SLM plane. This ensures that the target plane output will be upright and skew-free.

We then apply a uniform phase of π to the SLM, transmitting all light to the CCD, which measures the initial intensity distribution denoted by U , from which we will subtract. This image is transformed to SLM coordinates via the above scheme, and the phase applied to the SLM is given by:

$$\Phi_{ij} = 2 \sin^{-1} \left(\sqrt{\frac{\alpha T_{ij}}{U_{ij}}} \right) \quad (4.2)$$

where T is the target, and α is a numerical scaling factor for the target. For maximum theoretical accuracy and efficiency, alpha should be set to:

$$\alpha = \max \left(\frac{T'_{ij}}{U'_{ij}} \right) \quad (4.3)$$

where the prime denotes that the distribution should only be evaluated where the *target* is non-zero. This value is such that the theoretical efficiency is maximum while keeping the target intensity αT less than the initial intensity U at all points.

A practical limitation of the method is the presence of multiple reflections from the PBS and nearby mirrors which can overlap the intensity distribution, causing a small quantity of unmodulated light to leak through to the target plane, even with a setting of zero transmission. We found this leakage light to be present even with precise polarization alignment, and clipping of all visible spurious reflections. This leakage light was measured to be 2% of the total intensity when the phase was set uniformly to zero transmission. This leakage distribution does not change significantly with phase modulation, and thus its inclusion in U is erroneous, and makes the output in the target plane given by eqs. 4.2 and 4.3 to be slightly incorrect.

To correct for this, we apply an active feedback to reduce the error of the output distribution. The first guess output, which we now denote with an extra iteration superscript, I_{ij}^0 is used to change the first guess phase Φ_{ij}^0 . First, α^0 is recomputed:

$$\alpha^\gamma = \max \left(\frac{\tilde{T}_{ij}}{\tilde{I}_{ij}^{\gamma-1}} \right) \quad (4.4)$$

where here γ is the feedback iteration index, and the tilde means evaluating the distributions at only those pixels where $\Phi_{ij} = \pi$, or where the transmission is maximum. Thus, the maximum in eq. 4.4 finds the worst case pixel for which the transmission is maximum but the output is maximally far from the target. All images below, unless stated otherwise, are median filtered, so as to reduce any influence of dead pixels on this definition of α .

The phase during feedback is then adjusted according to:

$$\Phi_{ij}^\gamma = \Phi_{ij}^{\gamma-1} + \epsilon (\alpha^\gamma T_{ij} - I_{ij}^{\gamma-1}) \quad (4.5)$$

here ϵ is a constant that both converts intensity units to phase, as well as ensures that the relative adjustment between iterations is small. Note that we do not again employ eq. 4.2, which would depend on the initial image. Here, we simply exploit the fact that output is very near the target, and that a pixel's transmission is monotonic function phase, when the bounds are enforced to be $[0, \pi]$. With an intensity scale normalized to unity, we found sufficient convergence with $\epsilon = 0.05$ radians.

Beam output in the target plane is quantitatively compared to the target in terms of the root-mean-squared (RMS) error, which is defined as:

$$\text{RMS Error} = \left(\frac{1}{N} \sum_{ij} \left(\frac{\beta I'_{ij} - T'_{ij}}{T'_{ij}} \right)^2 \right)^{1/2} \quad (4.6)$$

where N is the number of pixels inside the nonzero target region, and β scales the actual intensity I such that the RMS error is minimal. Note that any intensity of I outside of the target region is not included in the calculation of the error. We will discuss background minimization outside of the context of RMS error.

Our first target of choice was a hard edged flat-top circle of diameter $D = 2$ mm as measured in the target plane. The initial laser beam before shaping, the first feedback

guess, and shape after 7 iterations of feedback is shown in figure 4.3. If α is defined as above, feedback proceeds by removing additional light from the distribution. In the case of figure 4.3, feedback was stopped when the rms error of the flat-top reached 10%, so as to maintain good efficiency. The efficiency as estimated by both CCD images was 16%. Unmodulated leakage light is visible in figure 3C, in which the shaped power is the smallest. Flat-tops with even higher degrees of flatness using this method can be seen in [69].

4.4 TRANSMISSION OF SHAPED LASER LIGHT TO THE PHOTOCATHODE

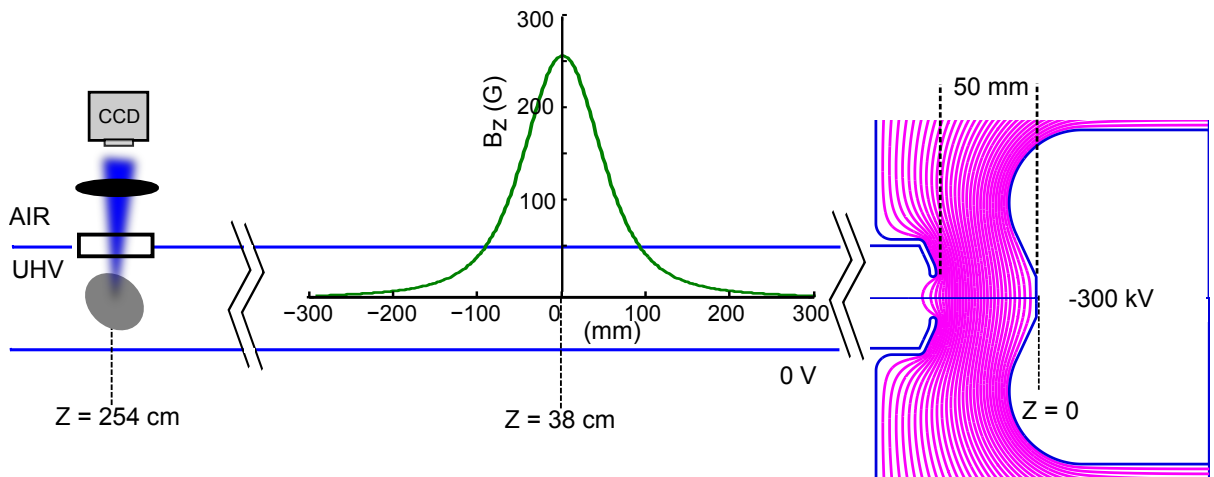


Figure 4.4: Layout of the electron beamlne, including the photogun (purple equipotential lines), imaging solenoid, and BeO fluorescent viewscreen and fluorescence profiling camera.

The method by which laser light is introduced to the gun vacuum chamber, and the electron imaging beamline is shown in figure 4.4. Light is transported to the gun via a vacuum window and an in-vacuum mirror in a dedicated laser entrance chamber (not shown). The in-vacuum mirror directs the laser toward the center of the photocathode, and

a second in-vacuum mirror directs beam reflected off the photocathode out of the vacuum chamber to a beam block. The photogun used has been described in detail elsewhere [57]. A Cs₃Sb cathode with average QE of 6% was used.

The electron beam was emitted with average (across all shapes produced) current density of approximately 30 nA/cm² at the photocathode, and thus the space charge force is negligible here. The beam is accelerated to 300 kV using a cathode-anode gap of 50 mm. A solenoid magnet 38 cm downstream of the photocathode is used as an imaging lens to image the cathode surface on to the 1.5" diameter BeO fluorescent viewscreen, angled at 45 degrees to the beam direction. The solenoid field profile is shown in figure 4.4. The fluorescence from the BeO prompted by the electron beam was imaged by a lens and CCD. We assume this fluorescence distribution to be directly proportional to the beam transverse distribution. We will slightly modify this assumption later. The size of the image taken with the CCD was calibrated via landmarks on the in-vacuum BeO holder, a method which is accurate to 5%, when compared to beam deflections from corrector magnets with known magnetic fields. The imaging solenoid field setting was found to correspond to particle tracking simulations to $\pm 2\%$. At these settings, the photocathode plane is magnified by a factor of 3.8 on the viewscreen, and the photocathode image is rotated by a Larmor angle of 46°.

The laser profile shown in figure 4.3C was transported to the cathode according to the above scheme, and the resultant beam profile measured on the viewscreen is shown in figure 4.5A. There are several features to note. The first is that the flatness of the laser shape is preserved in the electron beam, further indicated by the line cuts in figure 4.5C, from which we calculate a variation of only 4% rms. The second feature is a ring of decreased intensity around the shape. This fluorescence is not directly modulatable with laser power; changing the SLM transmission at the flat-top edge changes only the fluorescence on the edge of the

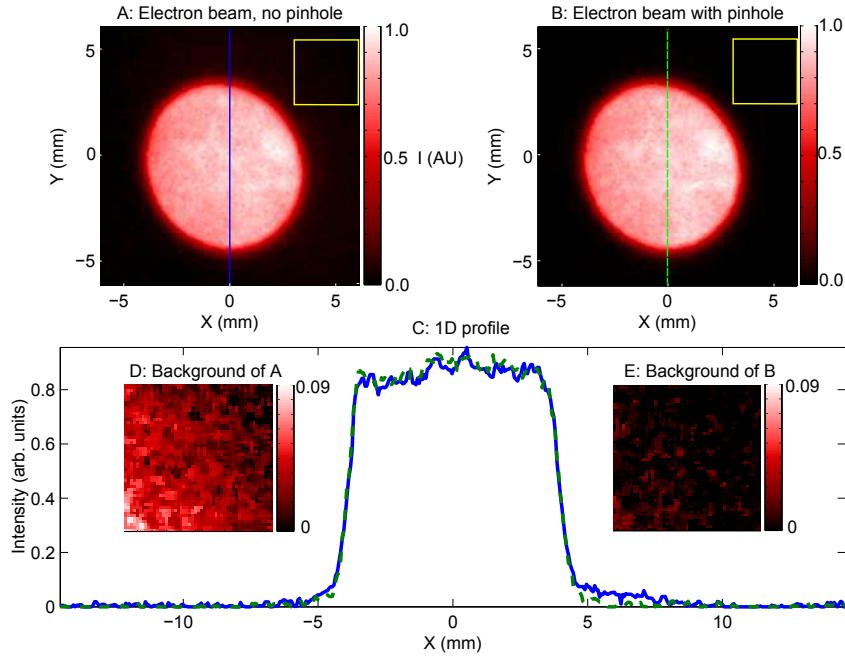


Figure 4.5: A: Resultant beam profile when the flat-top shown in figure 4.3C is transported to the cathode and the beam imaged on the viewscreen. B: Beam result when a pinhole is placed in the image plane of the second lens downstream of the SLM. C: 1D profiles along the lines shown in A and B. D: Background of A, taken from yellow boxed region. E: Background of B, taken from yellow boxed region.

bright interior. We believe this edge effect to be due to diffuse scattered beam fluorescence from the BeO, and does not correspond to a spatial “tail” in the electron distribution. This was further verified by clipping the electron beam with an aperture upstream of the screen, in which this tail effect was also seen.

Next, it is clear that the beam is no longer round. As the beam is round on an upstream viewscreen (not shown, $Z=130$ cm), this is not due to poor laser transport. We believe this is due to both imperfect alignment in the solenoid and a stray quadrupole magnetic field in the beamline. Though this can obviously be remedied with more perfect alignment and reduction of unwanted fields, we will correct for this electron optical aberration in the next section by using the SLM.

Finally, we note that the leakage light described above is also visible in the electron beam profile in figure 4.5 A and D. However, placing an appropriately sized pinhole in the imaging plane of the second lens downstream of the SLM can clip this leakage light without altering the central shape, as demonstrated in figure 4.6B, C, and E.

To illustrate the shaping capability of the SLM, we chose a much more elaborate laser target with various intensities and feature sizes. The Cornell University bear logo was used, converted to grayscale, as shown in figure 4.6A. The laser profile output of the laser shaping as described above is shown in figure 4.6B, which illustrates that polarization subtractive shaping is capable of resolving fine detail in both shape and intensity. To get an estimate of the error of the of this output image, the target was thresholded at 15% of its maximum value to remove small intensity points from inclusion in eq. 4.6, which yields an rms error of 20%. The efficiency was estimated from the CCD images of the initial beam and the final output to be 8%.

This shaped light was then transmitted to the cathode and the resultant beam was imaged onto the viewscreen, giving the distribution shown in figure 4.6C. The image is not median filtered, but is rotated to remove the Larmor angle. While the image still suffers the same aberrations in figure 4.5 and the smallest details are lost, most fine features are preserved.

4.5 ACTIVE ELECTRON BEAM FEEDBACK

Instead of transmitting a shaped beam profile to the cathode, we can instead transmit the unshaped laser beam and perform shaping on the electron beam image formed on the viewscreen. This method has two clear advantages. First, the laser profile is never directly

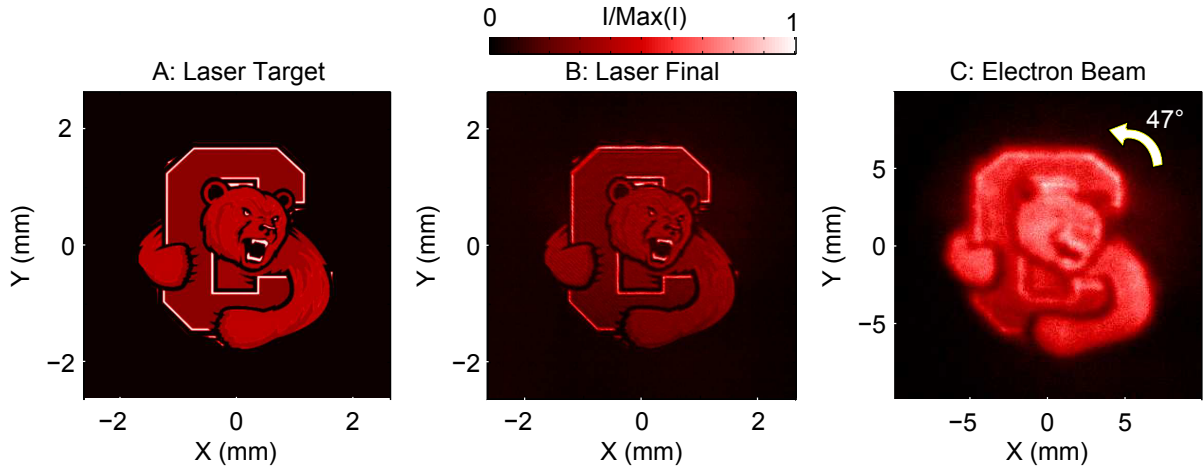


Figure 4.6: A: Laser target (see text for details) B: Final measured laser distribution C: Resultant beam distribution, rotated by 47 degrees in after acquisition, with no median filter.

imaged; only the product of the laser distribution and the QE distribution is known. Thus, this method will automatically correct for any QE non-uniformities. Secondly, with the electron viewscreen as the target plane, the above calibration with full skew transformation will also correct for any electron optical aberrations.

The coordinate transformation scheme described above in figure 4.2 is used with only slight modification. The target coordinates are those of the CCD which images the beam induced fluorescence. Instead of illuminating 1 pixel per triangle side, we illuminate three 3x3 square groups of pixels on the SLM, with each square centered on the points of the right triangle in figure 4.2. The resultant electron beam intensity maximum is then chosen as the corresponding point in the target plane.

This calibration scheme was found to systematically overestimate the size of the target area by a small amount. When lined up with the output on the viewscreen, the target shape only just encloses the non-modulatable tail presumed to be from diffuse scatter described above. This leads to the generation of artifacts in the beam shape. To improve the

coordinate system agreement, the target coordinates were reduced by 5% when compared to the output image, which is the minimum adjustment that keeps the non-modulated tail outside of the shaping region. This coordinate matching was aided by a 10x10 pixel average filter applied to the image for use in feedback (though not for error computation).

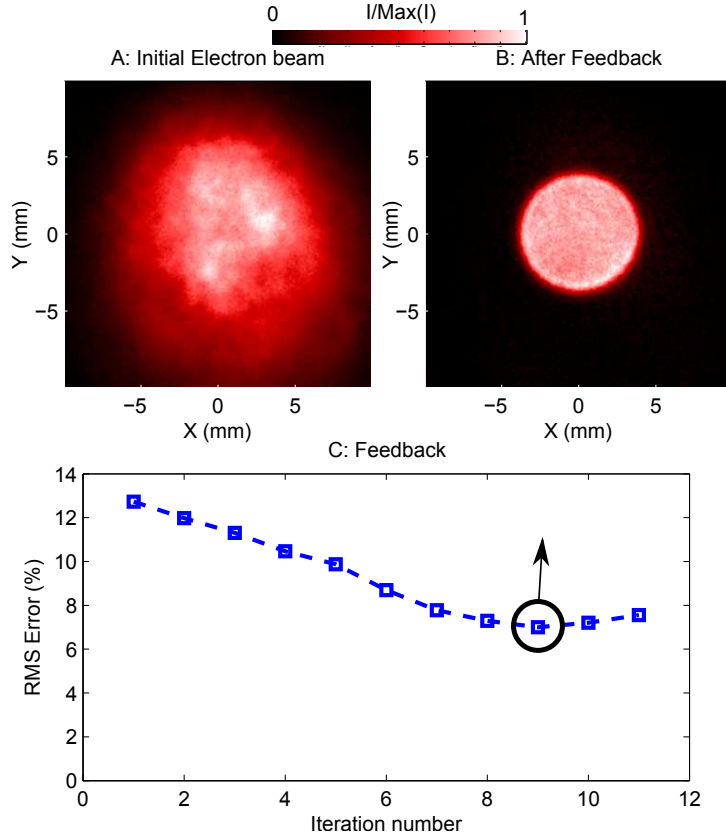


Figure 4.7: A: Initial unshaped electron beam imaged on the fluorescent screen B: Final output of electron beam-based feedback, with no profiling of the drive laser. C: Progress of feedback vs. iteration. The distribution shown in B is circled.

With these changes to the beam shaping feedback, we first chose to make a flat-top of comparable size to that of figure 4.5. The initial unshaped beam, the final feedback output, and the error as a function of feedback iteration are shown in figure 4.7. At the feedback error minimum, the beam distribution has flatness nearly equal (4-5%, depending on the position) to that shown of figure 4.3. The rms error of the whole shape, which

includes any mismatch between the target and output, is smaller than the error in the laser shape of figure 4.5, and is thus also very round. This indicates that the calibration scheme can successfully remove effects of electron optical aberrations. After reaching an minimum of error, further iterations usually increase the error, as seen in 4.7. This is due to small misalignment between the target and SLM plane coordinates. This mismatch causes an erroneous over-correction in subsequent iterations. In practical application, this over-correction can be detected and suppressed. After feedback, with a constant SLM setpoint, we did not observe any time dependent image quality degradation.

Though this method automatically corrects for any spatial QE dependence, as only the product of the laser intensity distribution and the QE distribution is ever measured, our results with the transmission of shaped laser to the photocathode indicate that there was no significant QE slope in the illuminated photocathode area. We emphasize the QE corrective capability of the method by creating a flat-top shape via beam feedback with an additional small bump, which simulates an area of low QE for which more laser power would be desired. This electron beam feedback shape is shown in figure 4.8. Furthermore, the truncated Gaussian, another electron profile of interest for beam applications [2], is also shown figure 4.8. Both shapes have an rms error <10%.

To test the ability of the electron beam feedback method to resolve small features, we chose to create the target of figure 4.6. In this example, we omit the 10x10 pixel average filter, to maximize resolution. With the inclusion of the skew transformation, the electron shape should be upright in the target plane coordinates. The results of beam feedback are shown in figure 4.9. The target is indeed upright, and the rotation and skew are now placed in the SLM plane shape, also shown in figure 4.9. We find comparable fidelity to the shape shown in figure 4.6C. This suggests that traditional laser shaping prior to transmission to

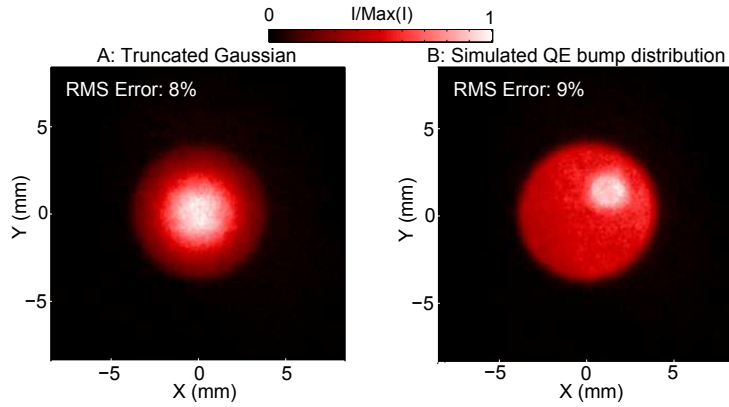


Figure 4.8: A: Electron beam distribution created with beam feedback: A truncated Gaussian. B: A beam shape for a hypothetical photocathode with a local QE dip, thus requiring a local maximum on the laser power (electron beam shown).

the gun could instead be performed by beam feedback at low current without loss of electron beam quality.

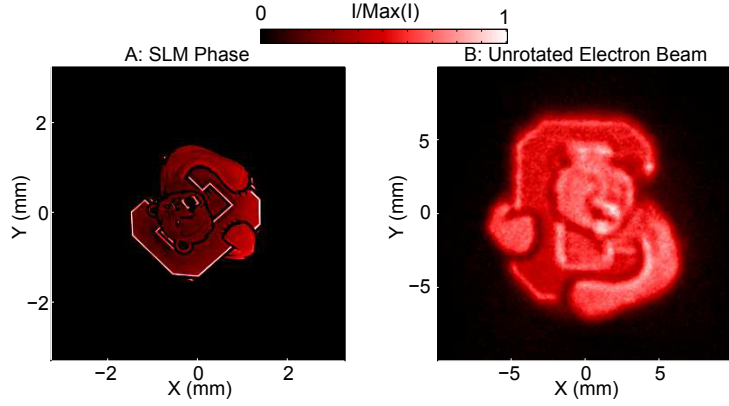


Figure 4.9: A: Phase applied to the SLM to create the shape in B. The phase ranges from $[0, \pi]$. B: Electron beam distribution created with electron beam feedback, which does not directly profile the laser. The target distribution is that of figure 4.6A, scaled by the electron magnification.

4.6 CONCLUSIONS AND OUTLOOK

In this work, we show that a simple method of SLM-based laser shaping, the polarization subtractive method, enables the ability to generate arbitrary low-current electron beam shapes of high accuracy from photoelectron sources. We demonstrate that the most direct beam shaping method of transporting a pre-shaped laser distribution to the cathode can preserve many of the features of the electron beam distribution, but will also naturally suffer from the electron optical aberrations. We demonstrate that these electron aberrations can be corrected using a feedback method at a target plane, using a simple calibration scheme. This method has the added benefit of never directly imaging the laser profile, and thus the feedback will correct both laser distribution irregularities along with any unwanted spatial QE dependence.

The potential applications of both beam shaping methods presented in this work are numerous, spanning the many applications of photoelectron sources. For high brightness beam applications, for instance, the transmission of a precise, arbitrary transverse beam shape to the cathode will allow more accurate characterization of the transverse optics during commissioning. While for some applications the laser power required for high current operation may exceed the SLM damage threshold, beam commissioning with high charge and lower duty factor [27] can allow SLM use for injector optimization. Furthermore, the electron feedback method can directly correct for any quantum efficiency irregularities that arise from photocathode growth or beam operation.

CHAPTER 5

MEASUREMENT OF THE TRADEOFF BETWEEN THERMAL EMITTANCE AND QUANTUM EFFICIENCY FROM A NAKSB PHOTOCATHODE NEAR THRESHOLD

This chapter has been submitted for publication in *Applied Physics Letters*.

5.1 ABSTRACT

We measure the tradeoff between the quantum efficiency and thermal emittance from a NaK_{Sb} photocathode at three increasing wavelengths (635, 650 and 690 nm) at or below the energy of the bandgap plus the electron affinity, $h\nu \leq E_g + E_a$. These measurements were performed using a high brightness, high voltage dc gun up to 400 kV, with surface fields varied between 1.4 – 4.4 MV/m. Measurements of thermal emittance are performed using two methods: a solenoid scan and a two-slit based measurement. The two methods are found to agree, and the momentum spread is measured to be \sim 35 meV at the longest wavelength available, 690 nm, for which the quantum efficiency is $\sim 10^{-4}$. This momentum spread corresponds to a thermal emittance of 0.26 $\mu\text{m}/\text{mm-rms}$. The applicability of NaK_{Sb} emitting at threshold to low emittance, small bunch charge applications, as well as to high brightness photoinjectors is discussed.

5.2 INTRODUCTION

Next generation continuous duty and pulsed photoinjectors for high brightness light sources such as energy recovery linacs [11; 111] and free electron lasers [10; 112] have demonstrated beam brightnesses directly limited by the brightness of the source [55; 113]. Aside from increasing the gradient of the electron source to increase the extractable charge density [36; 37], the only other route to higher source transverse brightness is the reduction of the photoemitted electron transverse energy spread. This energy spread is commonly characterized by one of two quantities, the mean transverse energy (MTE), or the thermal emittance, $\epsilon_{th,x}$. The two are related via

$$\epsilon_{th,x} = \sigma_x \sqrt{\frac{\text{MTE}}{mc^2}} \quad (5.1)$$

where σ_x is the initial rms size of the beam along a transverse Cartesian coordinate x , and mc^2 is the electron rest energy. MTE here is analogous to the temperature of the photoemitted electrons.

The MTE and quantum efficiency (QE) of multialkali and bialkali cathodes have been shown to have comparable emittance performance to that of negative electron affinity (NEA) semiconductor photocathodes such as GaAs when driven with green light [30; 31; 114; 115]. Furthermore, for the production of unpolarized electrons in high current photoinjectors, they routinely have significantly longer lifetimes than that of NEA photocathodes [116; 117]. For photon energies much larger than the work function, $h\nu \gg \phi$, which for NaKSb is approximately $\phi = 2$ eV [115; 118], the MTE is well approximated by a simple model assuming a constant density of states in the portion of the conduction band accessible by a photon of a given energy: $\text{MTE} = (h\nu - \phi)/3$ [30; 115] However, for photon energies near the work function, it was known as early as 1958 [118] that nonzero

photoemission can be obtained from impurity states within the band gap. The yield from these states was shown to be strongly suppressed with decreasing photon energy, and was further suppressed by reducing the cathode temperature to 77 K. Recent work [119] has shown that for CsKSb not only the QE but also the MTE from photoemission from these states is similar to what one would expect from photoemission at the tail of the Fermi-Dirac distribution in a metal. For a free-electron gas (e.g. a metal), it can be shown that the MTE of photoemission near threshold is given by [120]:

$$\text{MTE} = kT \frac{\text{Li}_3\left(-\exp\left[\frac{h\nu-\phi}{kT}\right]\right)}{\text{Li}_2\left(-\exp\left[\frac{h\nu-\phi}{kT}\right]\right)} \quad (5.2)$$

where here Li_n is the polylogarithm function of order n , $h\nu$ is the photon energy, ϕ is the work function, and T is the temperature of the material. As $h\nu \rightarrow \phi$, this expression approaches kT . For CsKSb, a semiconductor, it was shown that the MTE also approaches kT . Furthermore, reduction of the CsKSb temperature was shown to reduce the MTE. This work was performed at a single wavelength, $h\nu = 1.8$ eV, and so the behavior of the MTE at intermediate wavelengths was not determined.

5.3 MEASUREMENT METHODS

In the present work, we characterize the MTE and QE of a NaKSb photocathode, for 3 wavelengths near threshold, with photon energies from 1.8 eV to 1.9 eV, as well as in the green (532 nm) in order to map the tradeoff between MTE and QE with decreasing photon energy. NaKSb is chosen here as it has been shown previously to display lower MTE at 520 nm than other alkali-based photocathodes [31; 115], and thus we wish to determine whether this low emittance performance might extend into the near threshold regime. These

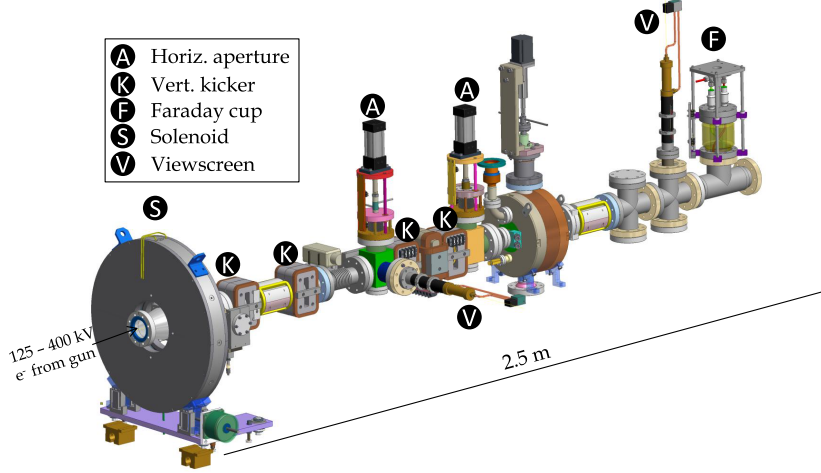


Figure 5.1: Beamline used for the measurement. The high voltage dc gun, not shown, is directly upstream of the solenoid.

measurements are performed on a high voltage dc gun, described elsewhere [57], as a function of the applied field, from 1.4 to 4.4 MV/m, which corresponds to 125 to 400 kV of beam energy, using a 50 mm cathode-anode gap. The use of a high voltage dc gun allows for *in-situ* characterization of the cathode performance using inexpensive dc diode lasers.

Beams with room-temperature transverse momentum spread ($MTE=25$ meV) and sub-millimeter rms sizes have normalized emittances in the tens of nm. To verify the measurement of such small emittances, we use two different emittance measurement methods. The first method is a solenoid scan, in which a solenoid magnet (shown in figure A.1) just downstream of the gun is varied and the resulting rms beam sizes are measured with a fluorescent viewscreen (BeO) and a CCD camera. If one calculates the linear transfer matrix which propagates the beam transverse phase space coordinates (x, p_x) from the cathode to the measurement screen, one can fit the resultant beam sizes as a function of solenoid current for the beam emittance and the initial spot size on the cathode. This method has been well documented and successfully employed to measure down to 20 meV in GaAs near threshold [30].

The second measurement uses what is called the emittance measurement system (EMS), also shown in figure A.1. The system is composed of two retractable horizontal slits, and two sets of fast vertical kicker magnets. The first slit and magnet system selects a small vertical slice of the beam's density distribution, and the second slit and magnet select a small slice in the vertical momentum of the beam's phase space distribution. Measuring the transmitted current through the slits with a downstream Faraday cup as a function of the kicker magnet setpoints, one can map the full 2-D vertical phase space density of the beam. The EMS has been described in detail elsewhere [121]. The quantum efficiency is measured by retracting the slits and measuring the full beam current on the Faraday cup, as well as measuring the laser power upstream of the laser's entrance into the vacuum chamber.

To determine the MTE from these measurements of emittance, one must also know the laser spot size on the photocathode. In general, for both methods and for all applied fields, we use 3 laser apertures (0.7, 1, and 1.75 mm diameter) to determine the linear relationship between emittance and spot size, the slope of which determines the MTE. In the case of the solenoid scan, the spot size on the cathode is fit alongside the emittance. Thus, the only significant uncertainties associated with the measurement of emittance are the error in the solenoid scan fit, as well as the error in the determination of the spot size on the screen. In general, for an accurate model of the fields, the error in the fitting can be negligible, as it is in all cases in this work. However, the error in the calibration of the image size of the fluorescent viewscreen on the CCD camera is more significant. We estimate it to correspond to a 5% relative error in all spot size measurements. This error is propagated through to the calculation of the MTE, yielding on average an error of ± 3 meV for the MTEs measured here.

The systematic uncertainty in the EMS measurement is larger in general. The field integral of each kicker magnet is calibrated by measuring its deflection of a beam on a

viewscreen, and thus each of the calibrations of the magnets depends on the viewscreen uncertainty. Furthermore, this measurement relies on the profiling of the laser distribution at a “virtual cathode” plane the same distance away from the shaping aperture as the actual photocathode. Our estimates of error in the MTE determined by the EMS system include both the uncertainty in the imaging of the laser profile as well as the uncertainty in the magnet calibrations. Given the larger total uncertainty (roughly ± 10 meV near threshold) in the EMS measurements, they are considered as secondary check for the primary measurements performed with the solenoid scan.

5.4 QE AND MTE OF NaKSB NEAR THRESHOLD

The NaKSB cathode was grown via sequential deposition from pure metal alkali sources onto a polished stainless steel substrate. The photocathode was then first moved into the chamber of another dc gun [55], where the QE at 532 nm was measured to be 5.5%, with an absolute QE uniformity of 0.5% over the central 100 mm^2 area. This photocathode was used for a series of low average current (μA), high bunch charge measurements in the full Cornell photoinjector [55], and was then moved to the gun testing lab for these measurements. Due to multiple cathode transfers, as well as its use for beam measurements, the QE at 532 nm at the start of these measurements had decreased to 3.1%. To check the agreement between the two emittance methods, the MTE at 532 nm and 4.4 MV/m (400 kV beam energy) was measured with the solenoid scan and the EMS. The measured values were 134 meV and 129 meV, indicating good agreement, as the uncertainty in the solenoid scan method here was approximately ± 10 meV.

The measurement of MTE of NaKSB at 635 nm, 650 nm, and 690 nm is shown in figure 5.2. There are several features of note. First, there is good quantitative agreement

between the measured values from both the solenoid scan and the EMS method within the experimental uncertainty. Secondly, the value of the MTE is near the room-temperature limit for the longest wavelength used.

Next, we note that there is only a very small slope in the MTE as a function of the applied field. This behavior is also seen in Eq. 5.2 near threshold. The change in the MTE from Eq. 5.2 due to the change in applied fields used here (via the Schottky effect, see figure 5.4 below) results in a MTE change of < 10 meV at 635 nm. The longer wavelengths are expected to have even smaller MTE changes at these fields. The difference in the slopes in MTE from solenoid and EMS measurements may be due to the fact that the ultimate resolution of the EMS also depends slightly on the orientation of the phase space at the slit, which is a function of both solenoid current and the gun voltage. Coupling this with the larger uncertainty, it is difficult to draw conclusions from the slope of the EMS data,

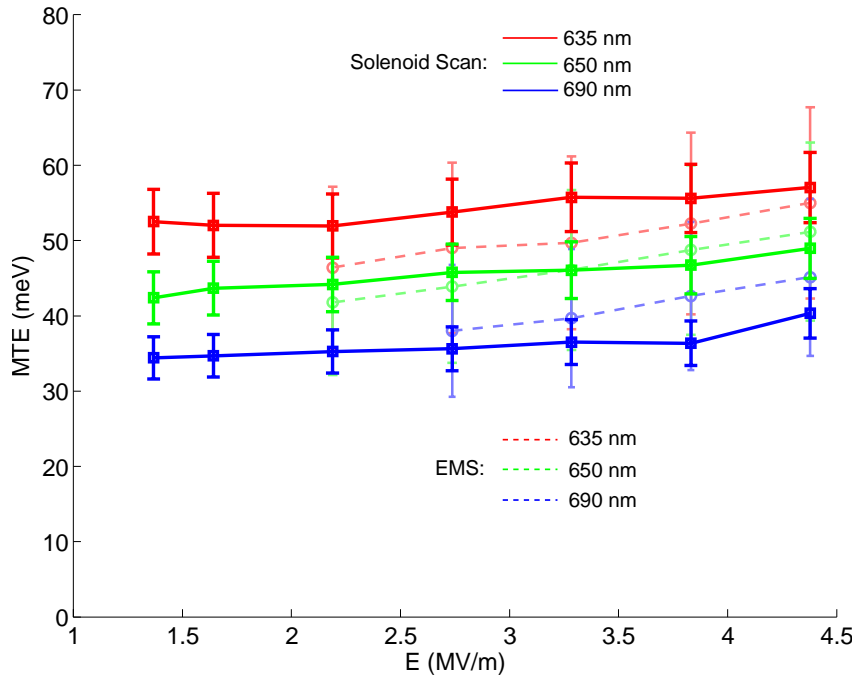


Figure 5.2: The measured MTE at various wavelengths as a function of field at the cathode surface. Both solenoid scan (solid) and EMS (dotted) are shown.

however the overall quantitative agreement with the solenoid scan measurement in this field range lends confidence to the small measured values of MTE.

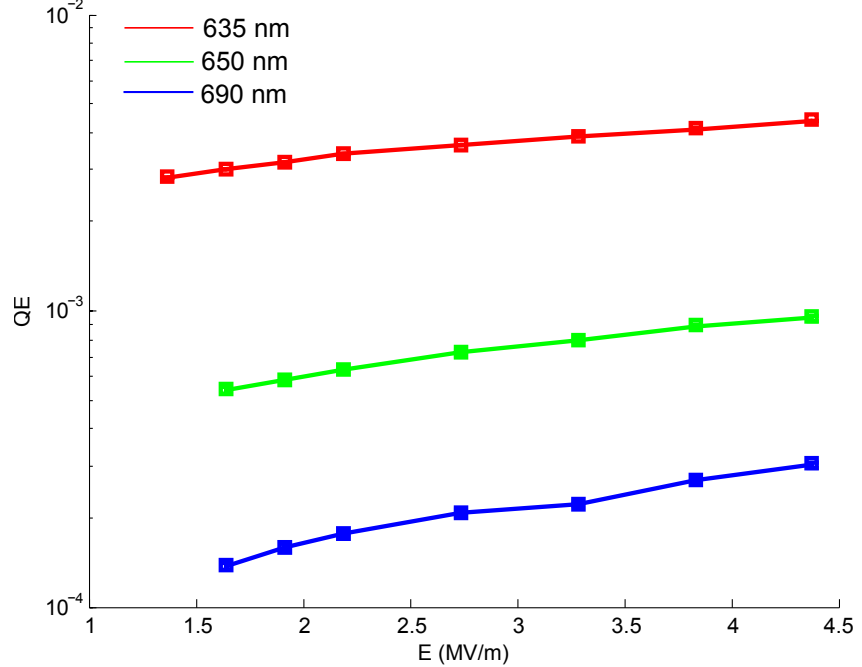


Figure 5.3: Quantum efficiency at various wavelengths as a function of the field at the cathode surface.

The quantum efficiency at these wavelengths are shown in figure 5.3. We note that the quantum efficiency near threshold is a stronger function of the applied field than the MTE, with the QE for each wavelength increasing by at least a factor of 1.5 when the field is increased from 1.6 MV/m to 4.5 MV/m. Again, this is similar behavior to a metal emitting near threshold, in that for a metal, a small change in energy in the tail of the Fermi-Dirac distribution can have a large impact on the number of electrons at that energy. We note that while the QE has decreased sharply with decreasing photon energy, the lowest QE measured is larger than the QE of typical metal photocathodes (10^{-5}) [29].

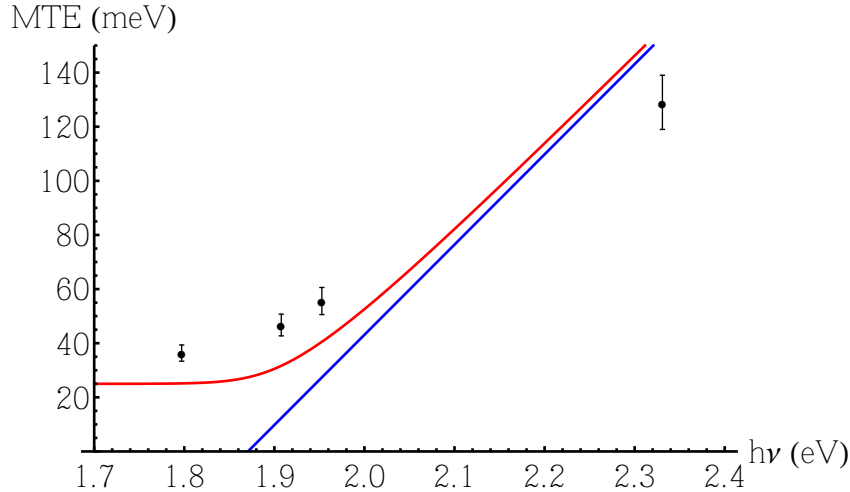


Figure 5.4: MTE at 4.4 MV/m, inferred from the straight line trend of solenoid scan data in figure 5.2, included with the solenoid scan measurement result at 2.3 eV. The red curve is Eqn. 5.2, assuming a Schottky reduction of the nominal work function of $\phi_{\text{eff}} = (1.95 - 0.08)$ eV. The blue curve is the simple model for large photon energy, $MTE = (h\nu - \phi_{\text{eff}})/3$.

5.5 DISCUSSION AND CONCLUSIONS

To compare the behavior of the MTE of NaKSB to the metallic case given in Eq. 5.2, we use a straight line fit of the solenoid scan data in figure 5.2, to smooth any effects of measurement noise. We then evaluate this smoothed behavior at $E = 4.4$ MV/m. The workfunction in Eq. 5.2 is then reduced by the Schottky value for that field $\phi_{\text{eff}} = \phi - e\sqrt{eE/4\pi\epsilon_0}$, where ϕ is taken to be 1.95 eV [115]. The resulting curve, along with the simple, linearized model $MTE = (h\nu - \phi_{\text{eff}})/3$ is plotted alongside the data in Fig. 5.4. The model of the metallic emission applied to NaKSB neglects a host of differentiating effects (varying density of states, electron-electron scattering rates, among many others [29]) and so does not capture the specific MTE values, but it does capture the qualitative nature of the photoemission as a function of photon energy and applied field.

Reducing the thermal emittance of photocathodes is the most direct route to increasing

the brightness of emittance-compensated beams. Emission at 690 nm from NaKSb yields near room temperature electrons (35 meV) for a room temperature cathode, giving a thermal emittance approximately a factor of two less than at 532 nm. The lowest temperature electron beam sources to date, cold atom electron sources for ultrafast electron diffraction (UED), have demonstrated MTEs between ~ 1 and ~ 20 meV [84; 122], with the smallest MTE limited directly by disorder induced heating [123]. However, the electron beam density is limited by the density of the atom cloud, and the smallest emittance performance of cold atom electron sources has only been demonstrated fC-scale bunch charges [124–126]. Alkali-antimonide photocathodes operating at threshold are shown here to be a low-emittance alternative to cold atom sources for UED or ultrafast electron microscopy [127] having much more relaxed limits on the beam density and bunch charge extractable. Furthermore, the QE at 690 nm is comparable to that of a metal, and so such photocathodes could be driven near threshold for next-generation high brightness photoinjectors. For instance, a 1 MHz high brightness photoinjector, delivering 100 pC bunch charges from NaKSb using 690 nm light would require $\leq 1 \mu\text{J}$ per pulse, or only 1 W of average power at the photocathode.

In this letter, we have characterized the long wavelength photoemission behavior of a NaKSb photocathode installed in a high voltage dc gun. We found that increasing the wavelength from 532 nm to 690 nm decreases the MTE from ~ 134 meV to ~ 35 meV, with a corresponding QE drop from $\sim 3 \times 10^{-2}$ to $\sim 2 \times 10^{-4}$ for various applied fields of several MV/m. We also use the comparison to metallic emission near threshold to explain the qualitative behavior of the photoemission properties as a function of wavelength and applied field. These results show that using such multialkali photocathodes near threshold allows for a simple, instantaneous increase in beam brightness.

CHAPTER 6

FUNDAMENTAL PHOTOEMISSION BRIGHTNESS LIMIT FROM DISORDER INDUCED HEATING

This chapter, with the exception of the following preface, was originally published as reference [123].

6.1 PREFACE

In the previous chapters, all discussions of the beam dynamics of photoemitted electron beams have considered the accelerating electron bunch as a continuous charge distribution. This assumption is referred to as the space charge approximation, and relies on adequate Debye screening of individual interactions. As photoemission temperatures are now reaching the scale 10's of meV or less, the space charge approximation may begin to fail at the electron densities being used in modern high brightness linacs. The following paper describes in detail the conditions under which the space charge assumption fails, and the new effects of individual electron interaction on the temperature evolution of a photoemitted bunch. This induced temperature rise can be viewed as a fundamental limit to the initial brightness of the beam.

6.2 ABSTRACT

We determine the limit of the lowest achievable photoemitted electron temperature, and therefore the maximum achievable electron brightness, due to heating just after emission into vacuum, applicable to dense relativistic or nonrelativistic photoelectron beams. This heating is due to poorly screened Coulomb interactions equivalent to disorder induced heating seen in ultracold neutral plasmas. We first show that traditional analytic methods of Coulomb collisions fail for the calculation of this strongly coupled heating. Instead, we employ an N-body tree algorithm to compute the universal scaling of the disorder induced heating in fully contained bunches, and show it to agree well with a simple model utilizing the tabulated correlated energy of one component plasmas. We also present simulations for beams undergoing Coulomb explosion at the photocathode, and demonstrate that both the temperature growth and subsequent cooling must be characterized by correlated effects, as well as correlation-frozen dynamics. In either case, the induced temperature is found to be of several meV for typical photoinjector beam densities, a significant fraction of the intrinsic beam temperature of the coldest semiconductor photocathodes. Thus, we expect disorder induced heating to become a major limiting factor in the next generation of photoemission sources delivering dense bunches and employing ultra-cold photoemitters.

6.3 INTRODUCTION

Beam brightness is a principle figure of merit for relativistic photoelectron sources for use in high brilliance linear accelerators or for ultrafast electron diffraction (UED) experiments. It is qualitatively defined as the average particle flux per phase space volume. For high brilliance linear accelerators used for x-ray production, the brightness of the x-ray beam is

directly determined by that of the electron beam. For UED setups, the brightness of the electron beam is main beam parameter that determines the visibility of diffraction pattern per electron pulse.

Such electron sources are comprised of a photoemitting material placed in an accelerating gradient, where both direct current (DC) and radio frequency (RF) accelerating fields are used for various applications. For either x-ray or electron diffraction experiments, it is often the 4 dimensional transverse normalized brightness that is most pertinent. For a given beam current I , we can define the “micro-brightness” as the phase space density itself, $\rho = \frac{dI}{dV_4}$, where $dV_4 = dx dy dp_x dp_y$ is the phase space volume element. The normalized total beam brightness can then be defined as a statistical average of the micro-brightness:

$$\mathcal{B}_{n,4D} = \frac{I^{-1}}{(mc)^2} \int \rho(x, y, p_x, p_y)^2 dV_4 \quad (6.1)$$

For a bunched beam with some bunch repetition rate f , the average current can be written as $I_{av} = qf$, where q is the charge of the bunch. In a previous work [36], it was shown that the maximum achievable beam brightness (either microbrightness or total) can be written:

$$\mathcal{B}_{n,4D} \Big|_{\max} = \frac{mc^2 f \epsilon_0 E_{acc}}{2\pi kT} \quad (6.2)$$

where E_{acc} is the accelerating electric field directly at the photocathode, which sets the maximum supportable charge density at the photocathode. The minimum divergence is set by kT , the temperature of photoemitted electrons, an intrinsic property of the choice of photocathode and laser wavelength. A nonzero temperature arises fundamentally from the electron momentum spread inside the photoemitting material, and can then be significantly increased due to excess laser energy above the photoemission threshold, as well as electron scattering off of imperfections in the emitter.

As it is one of the two independent parameters of the maximum achievable beam brightness per bunch, the photoemission temperature has been the focus of much work in

photoelectron sources. Great progress has been made by those working with negative electron affinity semiconductor photocathodes and those pursuing electron emission from laser cooled atoms. Several semiconductor photocathode groups have measured photoemission of equivalent temperatures well below $kT = 25$ meV, or the thermal energy at room temperature, either via the cryogenic cooling of the photocathode [128], or via the maintenance of a pristine photoemissive conditions in ultra high vacuum, allowing the low effective mass of conduction electrons to produce an effect equivalent to Snell's law in which the velocity spread of electrons is drastically reduced at the vacuum interface [129]. Furthermore, using laser cooled atoms which are photoionized, there has been production of electrons at temperatures equivalent to ~ 1 meV [130].

The number of electrons per bunch varies widely across various applications, with a range approximately between $10^6 \rightarrow 10^9$ electrons, which for moderate to high flux applications often corresponds to densities in the range of $n_0 = 10^{17} \rightarrow 10^{20}$ m⁻³. For a near-zero temperature bunch with such high density, we expect some contribution of individual stochastic Coulomb interactions from close encounters just after emission into vacuum to add to the total effective photoemission temperature. In this work, we determine this amount of stochastic heating as a function of beam density and initial temperature, as well as the nature of its evolution in time.

We expect this effect to be most prevalent when the electrostatic potential energy of neighboring particles is comparable to their thermal energy, that is $kT \sim e^2/4\pi\epsilon_0 a$, where a is the Wigner-Seitz radius, $a = (3/4\pi n_0)^{1/3}$. Thus for a given density, we expect the heating to be of the order $e^2/4\pi\epsilon_0 a$, and should thus scale with the cubic root of the density, and should be independent of the number of particles in the bunch. For a rough estimate of the importance of the effect, the plasma coupling parameter Γ can be used, defined as the ratio of kT to the average pair interaction potential. It ranges from $\Gamma = e^2/4\pi\epsilon_0 a kT = 0.2 \rightarrow 2$

given an electron temperature of 5 meV. Thus, for applications requiring a large charge density, we expect this stochastic heating to serve as a hard limit to the lowest attainable electron temperature, and limiting the maximum attainable beam brightness.

6.4 FAILURE OF ANALYTIC MODELS FOR COULOMB COLLISIONS

We will now describe how traditional collisional methods in beam physics, familiar to many accelerator practitioners, fail for the case of a cold dense beam. Readers familiar with the inability of such methods to accurately describe our strongly correlated case can bypass this section. A simple model for a bunch that has just been photoemitted into vacuum is a static, uniform, randomly distributed electron sphere with very small initial temperature $kT \sim 0$, in a constant accelerating field. We first draw a sharp distinction between the stochastic heating in question and the effects of space charge, which is the collective, mean field effect of Coulomb repulsion. The space charge approximation, applied in most beam physics calculations, self-consistently calculates the interparticle interaction based on the local single particle beam density, $\nabla^2\Phi(\mathbf{r}) = en(r)/\epsilon_0$, where Φ is the total electrostatic potential of a particle at \mathbf{r} . This approximation requires that the individual electron interaction is heavily screened, meaning that the Debye screening length $\lambda = \sqrt{\epsilon_0 kT/n_0 e^2}$ is much larger than the interparticle separation. However, for the lowest temperatures attained in semiconductor photoemission $kT \sim 5$ meV [129], and the lowest of the above densities $n_0 = 10^{17} \text{ m}^{-3}$, the Debye length is already on the order of the interparticle separation. In this case, the collective field will describe the overall density evolution, but cannot capture the growth of the stochastic component of the velocity.

The effect of Coulomb interactions in particle beams has been treated analytically in various schemes. Perhaps the most famous is the diffusive Fokker-Planck method. The Fokker-Planck method assumes that the effects of Coulomb collisions can be treated via the calculation of effective velocity diffusion and dynamical friction terms. This approach requires that the shifts in velocity due to Coulomb collisions are small compared to the overall velocity spread of the beam. This assumption is maximally violated for the case of a cold dense beam as described above, in which transverse velocities begin near zero.

Non diffusive, two-particle methods have also been developed that do not require the assumption of Debye screening. A clear presentation of these is given in [131]. The method applicable over the largest parameter space is the Extended Two-Particle Approximation (ETPA), developed by Jansen. This method relies on the calculation of the displacement (either velocity displacement, or position displacement) of a test particle in the presence of a single field particle over some collision time δt_c . If we calculate the velocity displacement Δv of a particle pair initially at rest, the ETPA allows the formation of the probability distribution $\rho(\Delta v)$, by averaging Δv over all possible separations and initial velocities in the beam. Each of these encounters is assumed to be statistically and dynamically independent. The second moment of the velocity distribution $\langle \Delta v^2 \rangle$ is then a measure of the temperature. We will proceed with a sketch of this calculation to highlight the failure of some of its assumptions in the cold dense beam case.

For two particles initially at rest (i.e. $kT \sim 0$) with initial separation r_i , using the dimensionless variables $\tilde{r} = r/r_i$ and $\tilde{t} = t \left(e r_i^{-3/2} / \sqrt{2\pi\epsilon_0 m} \right)$ the equation of motion for their separation is given by:

$$1 = \left(\frac{d\tilde{r}}{d\tilde{t}} \right)^2 + \frac{1}{\tilde{r}} \quad (6.3)$$

This equation is integrable for the function $\tilde{t}(\tilde{r})$, which is not analytically invertible, but is trivial to invert numerically to obtain $\tilde{r}(\tilde{t})$. With a global choice of δt_c , and with a test

particle chosen at the origin, we can obtain Δv as a function of r_i by replacing the scaling factors. Then, we average over the entire distribution of r_i :

$$\langle \Delta v^2 \rangle = \int n(\mathbf{r}) \Delta v(r, \delta t_c)^2 d^3 \mathbf{r} = \frac{2e^2 n_0}{\epsilon_0 m} \int r^2 dr \left(\frac{d\tilde{r}(\tilde{t})}{d\tilde{t}} \frac{1}{\sqrt{r}} \right)^2 \quad (6.4)$$

where \tilde{t} is also evaluated at δt_c and r_i . The velocity kick Δv falls off sufficiently fast with large separation, and the integral measure $r^2 dr$ ensures that the averaging does not diverge at small r , and thus we can integrate over all space. The equation 6.4 is the statistical average of all two particle interactions in a beam for during some time δt_c .

6.4.1 UNBOUND TRAJECTORIES

The expression given in 6.4 and similar uncorrelated two-particle collision methods fail in the cold dense beam case for two reasons. First, it assumes that each pair-wise interaction is statistically independent from each other. There can be no dynamic correlation between separate pair interactions. However in the cold dense beam case a large contribution to the final temperature can be given by simultaneous 3-body (or higher) interactions. The assumption of statistical and dynamical independence allows for the unbound expansion particles with very small initial separation, which are the most pertinent interactions in the cold dense beam case.

Even from the definition of the scaled coordinates, it is clear that any choice of δt_c corresponds to a some electron separation r_c below which all collisions taking place in that time will be sufficiently complete collisions, in which all potential energy is converted to kinetic energy. Alternatively put, given δt_c there will always be some electron separation small enough to make τ arbitrarily large. If we assume the initial distribution of electron separations to be uniform over all length scales, there is no unambiguous choice of cutoff in for r_c to avoid such unphysical free expansion, and thus no inherent timescale for two

particle collisions across the entire bunch. For perspective, in other Coulomb collision calculations, this ambiguity is seen the calculation of the so-called “Coulomb Logarithm”, defined as $\ln(b_{max}/b_{min})$, or the logarithm of the ratio of the maximum to minimum impact parameters over the whole bunch. However, as it appears under the logarithm in such problems, the minimum distance is often not considered to be a sensitive parameter [13].

In a similar method to the ETPA, in [132] Massey et al. calculate the uncorrelated root mean square fluctuation in the interaction force, and from it they obtain a stochastic energy spread. The authors directly impose a minimum interaction distance which corresponds to those collisions for which half of the potential energy is converted to kinetic energy over a certain time. Collisions with more of a fraction of potential energy release (i.e. smaller separation) are ignored. They readily acknowledge the ambiguity of this choice, and argue that the effect is small for the beams in their study. However, for a cold beam just after photoemission, it is this fast-timescale release of potential energy as close neighbors rearrange that we are interested in calculating. Thus, an average over independent two particle interactions is not sufficient here.

6.4.2 SCALING WITH DENSITY

Furthermore, even if one does make a choice of δt_c based on some other reasoning, the fact that this scheme involves taking a moment of the single particle distribution means one will always find $\langle v^2 \rangle \sim n_0$, whereas the effect we desire to calculate should have $\langle v^2 \rangle \sim n_0^{1/3}$, argued above. This scaling of the velocity spread with density occurs in the Fokker-Planck method (as shown in [13] in Eq. 5.243), in the ETPA (as shown in [131] in Eq. 5.5.11), and in the work by Massey (reference [132] in Eq. 19).

A method that produces the correct scaling with density, but is also flawed, is again

given by Jansen in [131]. In what he calls the “thermodynamic limit”, Jansen takes the difference of the total electrostatic potential energy of an initially uniform distribution of charge with no screening, and a final state of a Debye screened distribution with some kT , and sets this difference equal to the the total thermal energy, $\frac{3}{2}NkT$. However, instead of using a single particle density, Jansen implicitly uses the two-particle correlated density for a Debye screening:

$$\frac{3}{2}nVkT = U_i - U_f = \frac{1}{2}n^2V \int_0^\infty d^3r \frac{e^2}{4\pi\epsilon_0 r} (1 - \exp[-\phi(r)/kT]) \quad (6.5)$$

Here U_i and U_f stand for the initial and final potential energy in the system, respectively given by the first and second terms of the integral. $\phi(r)$ is the interaction potential of two electrons separated by r , and is assumed to have the form: $\phi(r) = e^2 \exp(-r/\lambda)/4\pi\epsilon_0 r$. The factor $n \exp(-\phi(r)/kT)$ is the final two particle correlated density. This equation has a solution of the form:

$$kT = \frac{e^2}{4\pi\epsilon_0} (4\pi\alpha^2)^{1/3} n^{1/3} \quad (6.6)$$

Where α is a dimensionless number determined by numerical solution of the above, $\alpha = 0.08702$ ¹ This number corresponds to an coupling factor at thermodynamic equilibrium of $\Gamma_{eq} = 3.53$. However, if one evaluates the number of particles in the Debye sphere, one finds $N_D = \frac{4}{3}\pi\lambda^3 n_0 \approx 0.03$, whereas the Debye approximation requires that the number of particles in the Debye sphere must be large. Thus, we may not apply the Debye/Yukawa form for $\phi(r)$ nor for the two particle density function used in 6.5. It is the use of a two particle correlated density function that provides the correct scaling with density, however, it is difficult to analytically compute the correlation in general. It must be found by some other numerical means [133].

¹An incorrect value of alpha is quoted for α in [131], which explains the use of the Debye relations, though the final value of λ shows that they are not applicable.

6.5 DISORDER INDUCED HEATING

The heating associated with the relaxation of a random, near-zero temperature distribution of charges is well known to the ultracold neutral plasma (UNP) community. In such systems, a cold gas is laser ionized, and after a time on the order of the $\tau = 2\pi\omega_p^{-1} = 2\pi (n_0 e^2 / m_e \epsilon_0)^{-1/2}$. In the traditional plasma physics terminology, this effect is referred to as disorder induced heating (DIH), and the effect is seen for Γ of order unity or larger [134], and we will argue that an exact analog of this effect is present in practical photoemission.

Disorder induced heating has been experimentally observed for the ions in a neutral plasma [135]. In cold neutral plasmas, the electrons equilibrate much faster than the ionic ω_p^{-1} , and then serve to screen ion-ion interaction. An expression for the amount of DIH in ions was first given for Yukawa systems (for which electron screening, but not electron-ion recombination, is considered) in [136]. The initial ionic distribution is uncorrelated, and can be defined as the zero energy state. As the ions relax, the ion distribution begins to develop order, and the resulting correlations have an associated binding energy. This correlation binding energy can be calculated from the two particle density function $g(r)$, and is only a function of Γ and the electron screening parameter $\kappa = \lambda/a$:

$$\frac{U_c}{NkT} \equiv \bar{U} = \frac{1}{2} \frac{e^2 n_0}{4\pi\epsilon_0} \int \frac{g(r, \Gamma, \kappa) d^3 r}{r} \quad (6.7)$$

This binding energy is balanced by an increasing ion temperature. Calculating the increase in temperature thus only requires knowledge of \bar{U} for a given electron screening. Analytic calculation of $g(r)$ for strongly coupled systems is difficult, and alternatively, \bar{U} has been tabulated via molecular dynamics (MD) simulations [136].

It has been demonstrated that a trapped, charged plasma, such as an electron bunch, is equivalent to the one-component plasma (OCP) model, in which the charges exist in a uniform neutralizing background [137]. The external containing potential allows the initial

uncorrelated state to be viewed as zero total energy. As electrons relax, correlations develop, and the presence of a “Coulomb hole” in $g(r)$ for $r < a$ creates an effective correlation binding energy equal to that of a one component plasma. In the case of an OCP, there is no second species to provide additional screening, and thus \bar{U} is only a function of Γ . Owing to this simplification, MD data has been fit to a power series relation for $\bar{U} = a\Gamma + b\Gamma^{1/3} + c$, where the coefficients are given in [137], $a = -0.90$, $b = 0.590673$, $c = -0.26569$. We may now write down the expression for the final coupling Γ_f , and thus the final equilibrium temperature, for a fully confined, initially uncorrelated ($\bar{U}_i = 0$), uniform distribution of charges with initial coupling Γ_i , analogous to that presented in [136]:

$$\bar{U}_f = \frac{3}{2} \left(\frac{\Gamma_f}{\Gamma_i} - 1 \right) = a\Gamma_f + b\Gamma_f^{1/3} + c \quad (6.8)$$

It is important to note the power series relation is quoted only for $\Gamma > 1$, however we find that for $\Gamma < 1$, the above expression is well approximated by $\Gamma_i = \Gamma_f$, or the limit of no DIH, as we expect. The final coupling given in 6.8 is plotted in figure 6.1. For an ideal bunch with zero initial temperature, $\Gamma_i \rightarrow \infty$, 6.8 can be solved to give $\Gamma_f \approx 2.23$.

Practical relativistic photoelectron sources contain a number of complicating factors. Inside the emitting material (either a cold gas or crystal), the electron coupling, and thus DIH, will be dramatically reduced by the presence of the ionic/nuclear potential, and thus here we only need to consider DIH developing in vacuum. The beam density during emission will vary in time and with position across the bunch. The temperature associated with DIH should be reached on the order of ω_p^{-1} after electron emission into vacuum, which for typical beam densities is on the picosecond scale. On this scale, we can neglect relativistic effects, such as the $1/\gamma^2$ damping of the interaction force [13]. The coupling given by $\Gamma_f = 2.23 \equiv \Gamma_{eq}$, for a given local beam density, can then be viewed as the

fundamental photoemission temperature limit. We consider the effects of a changing local beam density, as well as the nonrelativistic effects of acceleration during the evolution of DIH below, and we find it to correspond well with the prediction of 6.8. Rewriting it in terms of practical units, the heating induced in a zero temperature bunch is given by $kT[\text{eV}] = 1.04 \times 10^{-9}(n_0[\text{m}^{-3}])^{1/3}$. Along with 6.2, this forms the fundamental photoemission brightness limit.

To test the prediction of 6.8, we have chosen to use a tree-algorithm electrostatic simulation package, with nonrelativistic, spherical, uniform particle bunches. Traditional particle-in-cell integrators have an intrinsic length scale—the spatial grid on which local fields are calculated. However, tree algorithms lack a spatial grid, and thus are better suited to our initial conditions, where both close interactions and long range correlations are significant. Several plasma treecodes have been developed, see for instance [138], and one has been included in a relativistic particle accelerator code [139]. However, considering the simplicity of the problem, we elected to directly modify a code originally written for gravitational interaction [140].

We consider a randomly distributed spherical bunch of 10^5 particles with uniform density, and vary only the density ($10^{17} \rightarrow 10^{20} \text{ m}^{-3}$) and initial Gaussian velocity distribution ($kT \in \{0.25, 20\} \text{ meV}$ or $kT = 0$), where we use the definition $kT = m_e(\langle v_i^2 \rangle - \langle x_i v_i \rangle^2 / \langle x_i^2 \rangle)$, where m_e is the electron mass, and i is a Cartesian coordinate. There is no breaking of spherical symmetry in our simulations, thus equipartition will always hold. For a fully contained uniform bunch, $\langle x_i v_i \rangle \approx 0$, and the temperature is just a measure of average electron kinetic energy, with no spatial dependence. Containment is done in simulation via the application of a radial external force equal and opposite to the SC field. The parameters of the interparticle force calculation are the Barnes-Hut opening angle θ , and the leap frog integrator time step dt . The opening angle is the force

calculation accuracy parameter that determines whether an electron is treated individually or lumped together with other similarly distant particles [141]. No effect was seen from a force-softening distance p , such that the force between two particles is $f_{12} \propto (r_{12} + p)^{-2}$, from $p = p = a/10^6$ up to $p = a/100$. For all simulations presented, we have demonstrated convergence using $dt = \tau/120$, $\theta = 23^\circ$, $N = 10^5$.

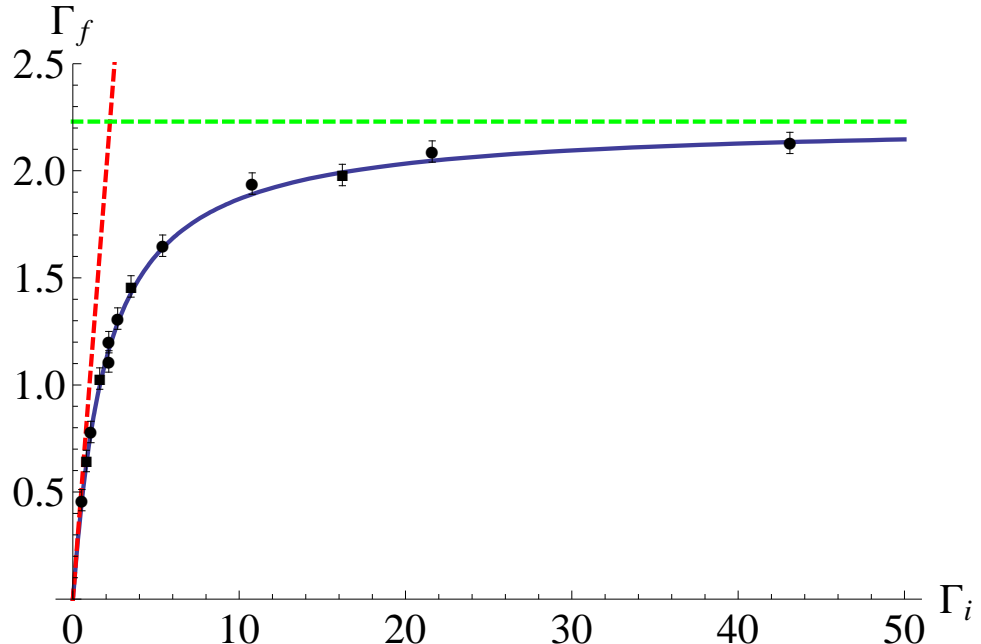


Figure 6.1: Final coupling Γ_f , vs initial coupling Γ_i , given by 6.8 (blue line), with $\Gamma_f = \Gamma_i$ for $\Gamma_i \rightarrow 0$ (red, dotted), and $\Gamma_f = 2.23$ for $\Gamma_i \rightarrow \infty$. Dots are simulation results of a fully contained, equipartitioned electron sphere, density $n_0 = 10^{20} \text{ m}^{-3}$, and initial temperatures between $kT=0.25 \text{ meV}$ and 20meV . Squares are simulation results for multiple densities, where $kT_z = 0$, and $kT_x = kT_y$, and where Γ is calculated from the average of the three directions. Error bars are an estimate of the uncertainty in final temperature determination due to the residual oscillations, as in figure 6.2.

For an initial distribution with zero temperature, the final temperature for several applicable beam densities is plotted in figure 6.2. We note that for extremely dense beams, $n_0 > 10^{19} \text{ m}^{-3}$, the DIH is comparable to the temperature of photoemission from the coldest semiconductor cathodes $kT \sim 5 \text{ meV}$. Furthermore, we note the oscillation of the

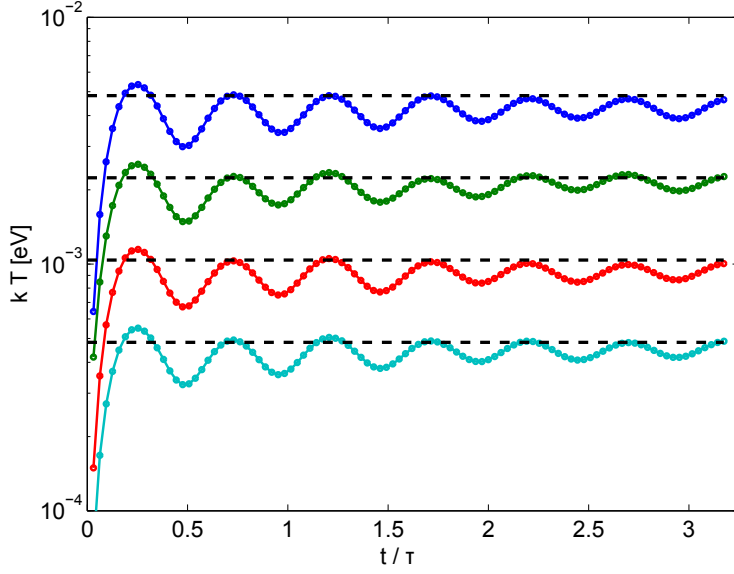


Figure 6.2: Temperature vs. number of plasma periods from treecode simulation using 10^5 contained electrons, and $n_0 = 10^{20}$ (top curve), 10^{19} , 10^{18} , 10^{17} m^{-3} (bottom curve), with zero initial temperature, $\Gamma_i \rightarrow \infty$. The equilibrium value predicted by 6.8, $\Gamma_f \approx 2.23$ is shown (dotted lines).

electron temperature at $2\omega_p$, which has been measured experimentally in UNP systems [135].

These oscillations last far longer than those seen in UNPs, as the bunch remains uniform in simulation (rather than Gaussian), and there is thus no spatial temperature smearing.

For bunches with nonzero initial temperature, the amount of additional heating can be calculated in the final coupling, plotted along with the prediction of 6.8 in figure 6.1. All simulations here had a constant density $n_0 = 10^{20} \text{ m}^{-3}$, with varied initial Maxwellian velocity distribution. The duration of the temperature oscillations visible in figure 6.2 is reduced with increasing initial temperature, though the exact dependence was not extracted in this study. In practical systems, initial acceleration in a voltage gap V will have cooled any photocathode emission temperature along the acceleration direction by a factor kT_i/eV , making $kT_{||} \sim 0$ almost instantaneously in high gradient electron sources, whereas the transverse velocity spread will remain unaffected [13]. Simulations were performed for

contained bunches of multiple densities with $kT_x = kT_y \neq 0$ and $kT_z = 0$. Equivalent dynamics to figure 6.2, as well as agreement with 6.8 were found if the average of the temperatures in all three directions is used to calculate Γ_i and Γ_f , as shown in Fig 6.1. The timescale of equipartition here also depends on kT_i and n_0 , but for the densities considered above and initial temperatures comparable to DIH heating, it was seen that equipartition occurs between τ and 3τ . A bunch instantaneously emitted into a uniform accelerating field will not have the DIH evolution altered, a fact that was also verified in simulation.

Real electron bunches just after emission are very infrequently fully transversely contained in the sense described above, and are not emitted instantaneously. The overall space charge force can double the beam radius on the timescale of ω_p^{-1} , and acceleration can significantly lengthen the pulse afterwards. Thus, we must consider the process of DIH in bunches with time dependent density reduction. A system of fully coupled charges will have an equilibrium temperature that decreases as $kT \propto 1/\Gamma_{eq}a$, as given by above. However, it is well known that system of noninteracting charges expanding under linear forces will have an equilibrium temperature that decreases as $kT \propto 1/a^2$ [13], as a consequence of RMS emittance conservation, which therefore leaves the phase space density or brightness unchanged. During the explosion, the beam is in a highly nonequilibrium state, but our definition of temperature above still applies, where here $\langle rv_r \rangle \neq 0$.

Simulations were performed to determine the temperature as a function of time for a bunch undergoing full Coulomb explosion. Multiple densities were considered, however the previous scaling with $n_0^{1/3}$ was seen. Thus, we present only results for $n_0 = 10^{20} \text{ m}^{-3}$ in figure 6.3. The total overall expansion and velocity growth is plotted in the inset, with the analytic prediction, showing excellent agreement. The temperature shows an initial increase due to DIH at a time of $t_{\max} \approx \omega_p^{-1}$, to a value of $kT(t = t_{\max}) = e^2/4\pi\epsilon_0 a(t_{\max})$, or a value $a(t_{\max})/a_0 \approx 1.6$ times smaller than for a fully contained beam. The bunch continues to

expand, attempting to equilibrate to $\Gamma_{eq} = 2.23$, and the temperature continues to decrease. However, at longer times, the temperature falls as a^{-2} , as in an uncoupled system. Thus, there must be a time at which correlation ceases to grow with decreasing temperature. Such behavior has been noted in the adiabatic expansion of UNPs due to kinetic pressure [142].

Thus, to model the temperature as a function of time, we can write the temperature as a product of the correlated growth, and the decoupled expansion after correlation ceases. Since the growth of the radius is small during the time of DIH, we may presume $T = T_c(t) \frac{a_0^2}{a(t)^2}$, where T_c is the correlated temperature dependence, and the term $\frac{a_0^2}{a(t)^2}$ describes the expansion of independent particles. The rate of DIH should be proportional to the how far the system is from the equilibrium temperature at the current density, and so:

$$\frac{dT_c}{dt} = \frac{T_{c,eq} - T_c(t)}{\tau_0} = \frac{1}{\tau_0} \left(\frac{e^2}{4\pi\epsilon_0 a(t)\Gamma_{eq}} - T_c(t) \right) \quad (6.9)$$

The only free parameter of this model is decoupling time τ_0 , or the time when the correlation ceases to increase. Integrating this numerically, and fitting to the temperature data, we find $\tau_0 = 0.325\tau$, which is also plotted in figure 6.3. This time is non-negligibly greater than t_{max} , and suggests that the bunch is cooled not only via decoupled expansion, but coupled expansion as well just after t_{max} . We can verify this prediction by looking at the pair correlation as a function of time. This is computed in figure 6.4, via averaging over 5×10^3 particles randomly selected from the distribution. The development of the “Coulomb hole” and an accompanying shock profile due to violent repulsion is clearly visible, as has also been seen in UNP simulations [143]. Indeed the correlation ceases to change after a time of approximately $\tau_0 = 0.3\tau$. Partial confinement effected by linear focusing in the source would yield an altered $a(t)$, and thus a longer τ_0 , whereas acceleration that lengthens the bunch significantly near the DIH heating timescale would yield a shorter τ_0 , but in either case the DIH heating timescale should remain unchanged.

The exploding beam case justifies *post-factum* the validity of the temperature limit of 6.8 for practical photoemission, though beams in many applications do not have constant volume. In the exploding case, near τ_0 the temperature scaling shifts from $a(t)^{-1}$ as given in Eq. 2, to the familiar scaling of $\sigma_v^2 \propto a(t)^{-2}$, as given by emittance/brightness conservation. A more detailed calculation of DIH for practical cases in which the bunch shape is both time and space dependent should involve averaging over a temperature distribution given by 6.8 and 6.9 using the local density as determined by space charge tracking.

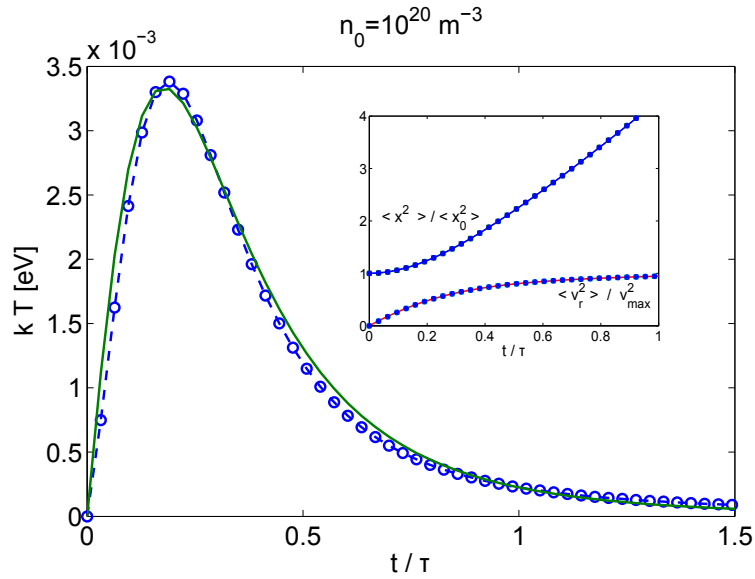


Figure 6.3: RMS velocity spread of a spherical bunch undergoing coulomb expansion, treecode data (circles), and prediction of 6.9. The inset shows the overall expansion of the bunch in normalized units, both analytic prediction (solid line), given by Gauss's Law, and treecode data (dots). Uniform bunches remain uniform, and the normalized bunch size $R(\tau)/R_0$ is independent of density.

6.6 CONCLUSION

In summary, we have characterized the fundamental temperature limit of photoemission from the disorder induced heating of electrons due to poorly screened Coulomb interactions

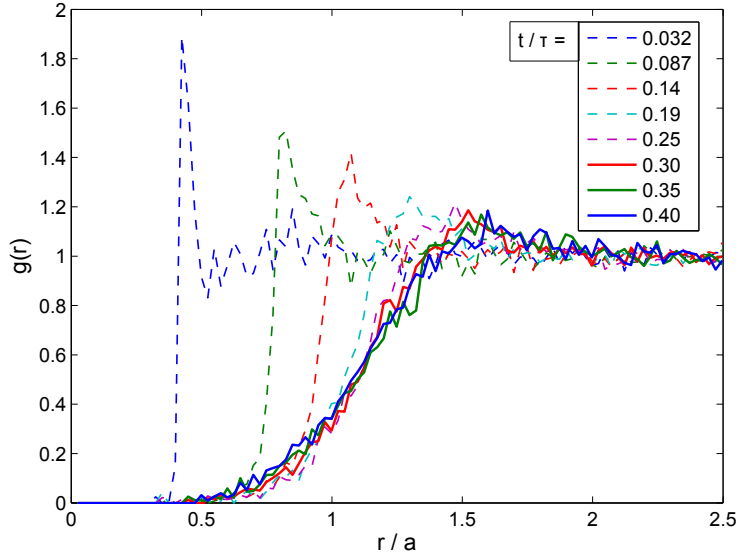
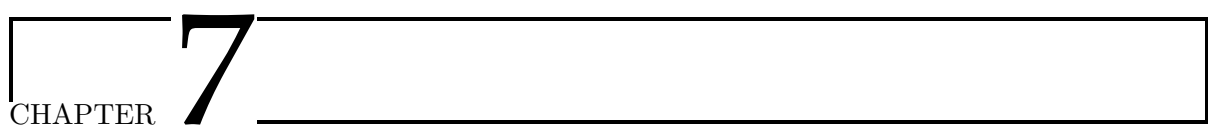


Figure 6.4: Pair correlation function $g(r)$, computed at multiple simulation times for a bunch undergoing coulomb explosion. Both the initial “shock” profile and the freezing out of correlations despite increasing Γ is visible.

at all length scales, where the analytic two particle models fail. We have shown that the tabulated thermodynamic quantities of one component plasmas are sufficient to explain both fully contained and Coulomb exploding instances of DIH, and have verified two simple relations that describe the temperature evolution. Furthermore, many interesting effects of DIH in UNP, such as temperature oscillation and correlation decoupling, should also be present in such cold beams, yielding the possibility of rich interdisciplinary study.

Practically, for next-generation ultracold dense electron sources we have shown that the temperature of photoemission, and thus the maximum beam brightness, cannot be arbitrarily improved. Furthermore, given the rapid progress of photocathode temperature reduction, we anticipate such a limit to be approached in the next generation of high brightness electron sources producing intense beams.

CHAPTER **7**

CONCLUSION: THE FUTURE OF DC GUNS

The current design and implementation of dc guns is reaching its full maturity. This work has touched upon a number of items that illustrate this fact. First, this work has shown that both the photocathode field and voltage of current dc guns is now approaching the maximum breakdown limits suggested by comparing the obtained dc gun voltage with an exhaustively studied, commercially available high voltage vacuum diode. It is seen here and ubiquitously elsewhere in other high voltage systems that a reciprocal relationship exists between the two. We have shown that for sufficiently high bunch charge in the example system of the Cornell photoinjector ($> 100 \text{ pC}$), this field and voltage tradeoff corresponds to a tradeoff between the full and the peak transverse brightness.

For sufficiently low bunch charge ($< 100 \text{ pC}$) in the Cornell photoinjector, we have shown in simulation the space charge induced emittance growth can be well compensated, such that the final emittance is dominated by the emittance at the photocathode. This photocathode emittance is given by the size of the laser spot and the intrinsic momentum spread of the photoemitted electrons. For the commonly used, durable multialkali semiconductor photocathode material NaKSb, it was shown that this momentum spread approaches values near kT , the limit in the free-electron gas model , as the wavelength of the light approaches the emission threshold. Though the quantum efficiency is reduced by several order of magnitude, as compared to emission with green light, this reduced quantum efficiency at threshold is comparable with those achieved with bare metal photocathodes,

which are the source of many high brightness electron accelerators. These measurements suggest that using NaKSB photocathodes near threshold can provide a factor of two increase in beam brightness as compared to typical operation with green light.

Recent work [55] has shown that for high enough charge in the Cornell ERL injector, imperfections in the initial transverse distribution of electrons can have a significant ($\sim 25\%$) effect on the transverse emittance in simulation and experiment. Longitudinal shaping has been studied extensively and successfully employed using various schemes. This work is the first to define a high accuracy, adaptive transverse shaping method, illustrating the flexibility by creating low current electron beams of arbitrary transverse shape.

The prescription to produce maximally bright beams from current-generation dc photoguns is clear. First, one must determine an electrode gap that emphasizes either the core or full brightness of the beam, depending on the particular application, and the charge per bunch. Next, the gun should be high voltage conditioned to the fullest extent possible to obtain excellent voltage stability and vacuum, allowing the use of low emittance semiconductor photocathodes. Next, illuminate the cathode with a high accuracy shaped laser pulse near threshold. Given the reduced QE at threshold (between 600 - 700 nm) as compared to in the green, providing enough light to produce the 100s of pC may be the most pressing challenge in this prescription; however, much progress continues to be made in the development active media for pulsed lasers in this wavelength regime[144].

Significantly brighter beams from dc, in-vacuum accelerating gaps will come from guns that differ significantly from those illustrated in Chapter 1. While the laser distribution is now fully adaptable, significant improvements to the MTE of photocathodes are still possible, and a different configuration of electrodes might yield the possibility of both

larger voltage and higher extraction field. These two “next-generation” improvements are mentioned below.

7.1 HIGHER VOLTAGE *and* FIELD

Two different configurations of electrodes have the promise to offer both higher field and higher voltage. The first configuration, called the dual gap gun, is the most natural conceptual extension of the single gap design. Since higher electric fields can be generated with smaller gaps, the photocathode can be seated in a low voltage, high field accelerating gap. Once the electrons traverse the low voltage gap, they immediately enter a higher voltage, larger gap accelerating column. This design is by no means new; the thermionic triode vacuum tube, the precursor to modern transistors, was essentially a dual gap thermionic gun. For the case of a high voltage photoelectron source, using two voltage dividing resistors $R_1 < R_2$ as shown in figure 7.1 allows a small voltage gap to be inserted into a segmented insulator. This eliminates the need to float a second power supply at the high voltage to obtain two different voltages.

Figure 7.1 suggests that an on-axis insulator is more desirable for the multiple gap case than the off-axis insulator. The use of two voltages has a significant impact on the gun beam dynamics. First, there is clearly a sharp decrease in the accelerating field as the beam travels from the first gap to the second, and a second decrease in field when the beam exits the gun into vacuum. The requirement of the potential to obey $\nabla^2V = 0$ can be shown to imply that $E_r = -\frac{r}{2} \frac{dE_z}{dz} + \mathcal{O}(r^3)$, and therefore a decrease in longitudinal field requires corresponds to a defocusing lens. Hence, the dual gap gun contains two defocusing lenses.

The defocusing effects of the two gaps, coupled with space charge driven beam expansion,

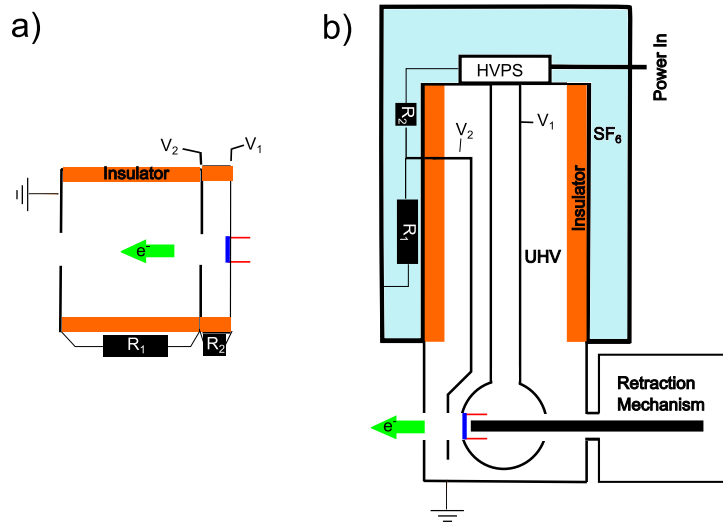


Figure 7.1: a) Example of the dual gap geometry, using two voltage dividing resistors, $R_1 < R_2$. b) The dual gap geometry does not easily lend itself to the off-axis insulator, as it requires another large electrode.

may require additional focusing near the source. In the analogous case of a long rf cavity with many cells used as a photogun, it is typical to encase the cavity in a solenoid to provide this focusing. To reduce the effects of initial angular momentum on the beam, a second coil cancels the magnetic field at the emission point, see for instance [13; 26]. This is the most sensible way to provide focusing in the second dc gap. However, the specifics of placing and powering two solenoid within the SF₆ environment are difficult engineering questions. As such, no dual gap high voltage photoemission gun of this sort has been created to date, though it is indeed possible, and may offer lower emittance. To determine this, a modular geometry field map should be generated and optimized in the manner of the study in Chapter 2, and compared with the results of this work.

A second, less practically challenging method to generate higher extraction field and higher voltage is the use of field enhanced emitter tips, similar to those used for field emission electron sources in electron microscopes. The idea here is that the gap can be

made large to support a high voltage, and a sharp feature on the photocathode can enhance the small nominal photocathode field by an order of magnitude or more [145]. The factor β by which the sharp tip feature enhances the nominal field is usually well approximated by the ratio of the height of tip to its radius, $\beta \sim h/r$. This design does not require altering the general form of the dc gun described here; it only requires a modified photocathode. An example of such a field enhancement feature is shown in figure 7.2.

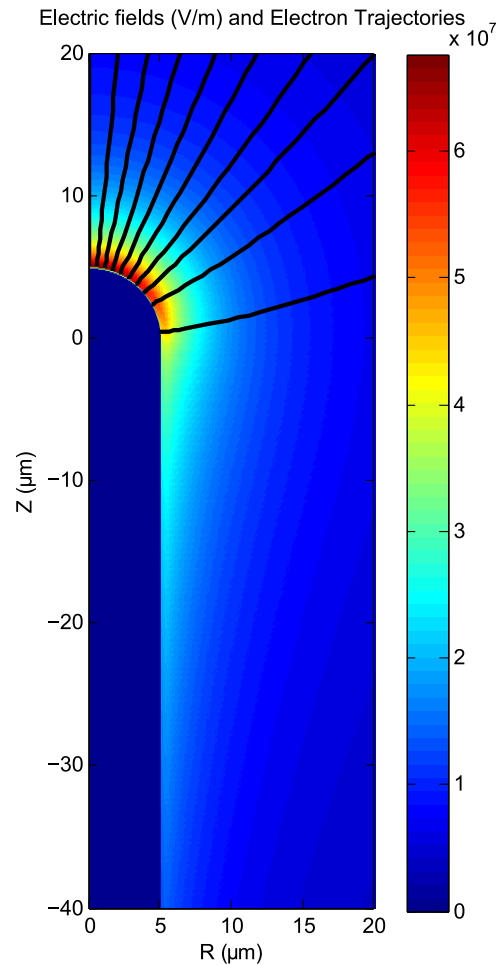


Figure 7.2: Example of a field enhancement feature, here shown for $\beta \sim 20$, and a nominal field of $E_0 = 3$ MV/m. The base of the tip is not shown. Magnitude of the electric field and electron trajectories from various positions on the tip are shown.

In some cases, an intermediate electrode, called a gate electrode, is placed directly in

front of the field enhancement tip. Thus this case is also a dual gap configuration. If the tip and the gate electrode are grown using semiconductor nanofabrication techniques, the electrode distance can be on the scale of 100s of nm, requiring only 10's of volts to reach fields approaching GV/m [146]. Using a gated structure with a nanoscale gap would require only that a battery, or other small voltage source for the gate electrode be floated at high voltage, which is also very feasible.

There are two main issues with field enhancement tips sources. The first is they are clearly very likely to field emit to some degree, particularly if they are coated with low work function semiconductor cathodes (2 eV, as compared to 4-5 eV for bare metal tips). The field emission is of course tunable with the field enhancement factor and material work function, and so the final extraction field achievable will be a strong function of the experiment's ability to tolerate a dc field emitted current as the background to the pulsed photoemitted current.

The second difficulty is the large nonlinear fields in the region of emission. These fields, and some example electron trajectories for a $\beta \sim 20$, nominal field $E_0 = 3$ MV/m are shown in figure 7.2. Note that the field decays strongly on the scale of the diameter of the tip, and thus this again corresponds to a large defocusing force by the same argument as above. The curvature of the geometry results in a strong nonlinearity of the fields in the region of the tip, making the preservation of the traditionally-defined cathode emittance difficult. However, it may be possible to shape the tip such that the nonlinearity is removed. This idea is discussed in the Appendix.

If this geometric emittance can be dealt with, needle-like features for photoemission offer multiple benefits. The first is clearly a larger extractable charge density due to the large field. Furthermore, if a semiconductor photocathode like NaKSb could be grown on

the needle structure (and surrounding area), the large difference in field on the tip and the base could yield a large quantum efficiency difference between the two, if driven near threshold. Thus, most of the electrons would be emitted from the tip, regardless of the input laser size. This may enable initial beam sizes smaller than those achievable with diffraction limited visible light. High density and small transverse size are of particular interest to the growing field of ultrafast electron microscopy and diffraction.

7.2 LOWER MTE

The path to lower MTE is clear. If both metal and semiconductor photocathodes have a MTE that tends toward kT as the photon energy decreases toward the emission threshold, then one must simply reduce the photocathode temperature. This is not an insurmountable technical challenge. In fact, the first dc photoemission gun cathodes were operated at liquid nitrogen temperature to provide a higher degree of electron polarization [28]. A recent work has demonstrated that indeed for semiconductor photocathodes that the MTE at threshold decreases with temperature [119], though this was done with a low voltage (< 50 kV) photogun. Using a cooled photocathode in a high voltage gun presents significant high voltage design challenges, particularly if a SF₆ enclosure is to be used. In that case, the refrigeration system must extend along the length of the stalk, must be floated at the high voltage, and must have an interface to draw power from high voltage power supply.

An alternate design for lower voltage guns, with or without an SF₆ tank would be to use a second electrical insulator with high thermal conductivity in contact with the cathode electrode. The cold head of a refrigeration system, attached to the ground end of this second insulator, could then cool the cathode electrode while remaining electrically isolated from it. The design has the benefit of both not needing to float the cryogenic apparatus, and with

an appropriate cryogenic system, it would not require frequent refilling of cryogen. At the time of this writing, tests are currently underway at Cornell on a low voltage gun (< 200 kV) cooled via a sapphire rod (high thermal conductivity, low electrical conductivity at low temperature) in contact with the cathode and the cold head of a liquid helium cryopump.

7.3 CONCLUSION

Now is an exciting time for the development of dc guns as the sources for high average brightness accelerators for synchrotron light sources and high energy colliders. Though the parameter space of dc gun photoinjectors is necessarily large, a robust optimization scheme such as the one used in this work can reproducibly determine brightness maxima. The optimized solutions correspond to a high degree of emittance compensation with high bunch charge ($\sim nC$). Perhaps most excitingly, the simulated high bunch charge, well-compensated emittances have been demonstrated experimentally in the Cornell photoinjector [55; 147], which is a level of performance once thought reserved for rf sources. These results already show the dc gun to be a mature technology for large scale high average brightness electron linacs. With this as a starting point, this work outlines the specific means by which the brightness of current high voltage dc guns may be further increased towards its ultimate limits. Aside from large scale accelerators, dc guns serve many smaller, university-scale electron beam experiments needing bright electrons such as ultrafast electron diffraction and microscopy. It is in these smaller scale applications where the such “next-generation” design modifications described in this chapter may be most easily implemented and tested.

Beyond its practical success as a source technology, the maximum simplicity of the accelerating fields of the dc gun makes it the ideal testing environment for a wide array of new accelerator concepts, such as new photoemissive materials and new beam generation

concepts. This work has illustrated just a few, ranging from the emission of low temperature electrons, to generating beams of arbitrary shape. The number of avenues of study with dc guns is far larger than this subset, and is perhaps only limited by the creativity of the practitioner.

THE GEOMETRIC EMITTANCE OF NEEDLE PHOTOCATHODES

The emittance of emission from a needle-like field enhanced photocathode can be large due to the strongly nonlinear field distribution at the source. The goal of this appendix is to explore the dependence of this nonlinearity on the shape of the tip. For simplicity, we do not include any effects of space charge, nor do we consider the feasibility of manufacturing a given needle feature with the required accuracy to experimentally obtain the emittances calculated here.

The calculation of the field distribution from a needle tip can be challenging, given that the needle aspect ratio can be large, in the range of 10-100 or even higher for field emitter tips. Furthermore, one of the benefits of using needle photocathodes is their small physical size (μm scale radii, for example). However, if using an ungated needle photocathode, the anode may be several millimeters away. Thus, for finite volume element mesh Poisson solvers, both the large aspect ratio and the scale discrepancy often yield taxing (though not prohibitive) constraints on the mesh resolution. This issue has been dealt with by using analytically tractable approximations to the emitter shape [148], as well as using a boundary element method Poisson solver instead of a volume element one. We chose to implement the latter. It is described in detail below.

A.1 A BOUNDARY ELEMENT POISSON SOLVER

The methods used here follow those described in [149] closely. The boundary element method involves discretizing only the boundary of the volume (rather than the volume itself), and by choosing the appropriate strength (the charge density) of each discrete boundary segment such that the boundary conditions are satisfied everywhere. In the case of the a dc gun, the electrodes are the boundary, and the boundary conditions are that the electrodes are held at the specified potential. An illustration of the method, as well as the superposition simplification described below is shown in A.1.

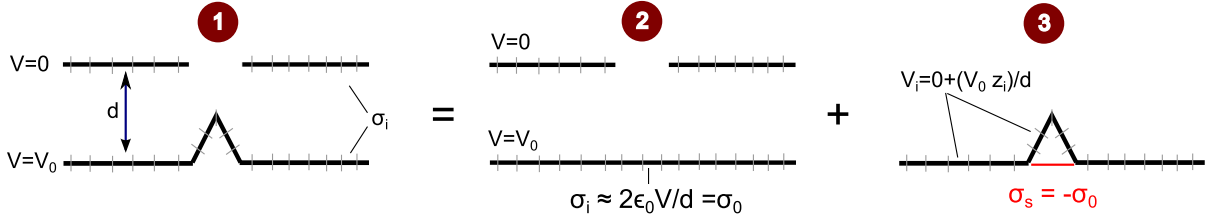


Figure A.1: The setup of the boundary element method. The method solves for unknown σ_i that generate required potential on the other segments. The needle geometry can be simplified into two simpler problems, wherein the middle diagram has an approximate analytic solution.

The boundary (electrodes) are thus modeled as the sum of linear surface charge elements. Cylindrical symmetry is assumed, and so each line segment in the R-Z plane is actually a circular strip in real space. Each boundary element i is assigned a charge density σ_i . The potential at a site j due to element i is thus:

$$V_j = \int_{S_i} \frac{\sigma_i}{4\pi\epsilon_0} \frac{dS}{|\mathbf{R}_j - \mathbf{R}_i(\mathbf{S})|} \equiv P_{ji}\sigma_i \quad (\text{A.1})$$

where \mathbf{R}_j is the mean position of the j th element, and where S_i is the annular surface of the i th boundary element. Note here that $\mathbf{R}_i(\mathbf{S})$ is not constant in the integration.

Note that we need only sum over the elements $i \neq j$ to obtain the total boundary contribution to the voltage at j , $V_j = \sum_{i \neq j} \sigma_i P_{ij}$. If we specify the potential on each segment, we can then calculate the charge densities that satisfy this requirement via $\mathbf{P}^{-1}\mathbf{V} = \boldsymbol{\sigma}$, where bold signifies matrix notation.

The needle geometry shown in figure A.1, diagram 1 can be decomposed into two superimposed simpler geometries, diagrams 2 and 3. Diagram 2 is simply the gun geometry without the needle feature. In this configuration, the charge density on the cathode the charge density is relatively constant, $\sigma_0 = 2\epsilon_0 V/d$. Diagram 3 is only the needle feature, where the potential has a height dependent form $V_3 = V_0 z/d$, where z is the longitudinal coordinate. The region below the needle feature in diagram 3 includes a fixed charge density of $-\sigma_0$. With these specifications, $V_1 = V_2 + V_3$, and so $\mathbf{E}_1 = \mathbf{E}_2 + \mathbf{E}_3$ by superposition. The fields \mathbf{E}_2 can be obtained via volume mesh Poisson solvers or by analytic approximation.

In this form, the solution produces a set of charge densities that are not necessarily continuous along the electrodes. A continuous charge density can be created with a slight modification of the above procedure. Instead of the index i labeling the segment centers, it will now label the vertices of the segments. This increases the size of the matrix \mathbf{P} by 1 along each dimension. We can associate with a particular vertex a charge density *distribution* of $\sigma'_i = \sigma_i h_i(S)$, where $h_i(S)$ is a function that is unity at the vertex i , and linearly decreases to zero at the adjacent vertices $i + 1$ and $i - 1$. The function $h_i(S)$ is only a function of the geometry, and so we may write the contribution from the vertex i to the potential at the site j as:

$$V_j = \sigma_i \int_{S_i} \frac{h_i(S)}{4\pi\epsilon_0} \frac{dS}{|\mathbf{R}_j - \mathbf{R}_i(\mathbf{S})|} \equiv P'_{ji} \sigma_i \quad (\text{A.2})$$

Thus, when adding up the contributions from all vertices, the inclusion of the function h produces a charge distribution which changes from a vertex value to its adjacent vertex values linearly. Note that the charge density is now continuous everywhere, but its derivative is still discontinuous at the vertices.

Once the charge densities at each vertex are determined by the above method, it is straightforward to calculate the fields. For each field evaluation point, one must sum the contributions from each segment. This process can be very time consuming if the number of field evaluation points is large. In general, the field from a single segment can be written in terms of elliptic integrals of both the first and second kind [149], and so the method benefits from an efficient, vectorizable computation of those functions. However, even with this, pre-evaluating an entire grid for particle tracking purposes can then be just as lengthy as computation with a volume mesh solver. Instead, we chose to evaluate the fields at run-time as requested by a symplectic integrator, which drastically reduces evaluation time, when the number of particles is small. Furthermore, when the particles are sufficiently far away from the needle tip, we may neglect the contribution of \mathbf{E}_3 , which allows for nearly instantaneous tracking thereafter.

A small number of particles is sufficient to describe the geometric aberrations induced by the needle tip without space charge, and without the effects of finite thermal emittance. One must simply find the map of the emission site (r_i, z_i) to its final position and momentum $(r_f, \beta_r \gamma)$ at a given evaluation plane z_f . As will be demonstrated below, sometimes the relationship β_r vs. r_f is not a pure function, meaning that the electron flow (without space charge) is non-laminar. In this case, it is impossible to interpolate the discrete data to find the continuous relationship between the final momentum and final position. To get around this, each quantity is treated as a function of r_i , from which one can interpolate the smooth

functions of $r_f(r_i)$, and $\beta_r(r_i)$. Thus, averages over the final position and momenta have the form:

$$\langle \chi \rangle = \iint \rho(r_i) \chi(r_i, \theta) r_i dr_i d\theta \quad (\text{A.3})$$

where χ is the quantity to be averaged. This is permitted as here the dynamics are Hamiltonian, and thus Liouville's theorem applies, $\rho(r_i)r_i dr_i = \rho(r_f)r_f dr_f$. This method allows the use of any initial distribution of particles in the averaging, and is not constrained to be equal distribution of the actual particles launched in the particle tracker. For all that follows, we assume $\rho(r_i) = 1/\pi R^2$, where R^2 is the radius of the needle. Now we can calculate the the trajectories of a small number of electrons (20, in this case) from emission sites that span the tip, and obtain the geometric emittance induced by the tip.

A.2 EMITTANCE AS A FUNCTION OF TIP SHAPE

If a needle cathode is to be cyro-cooled and driven with a near-threshold light, the intrinsic momentum spread and initial spot size will yield a thermal emittance that potentially very small. For 25 meV and a uniformly illuminated tip of radius or $5 \mu\text{m}$, the thermal emittance is 0.5 nm. We wish to determine whether there is a needle shape that is capable of preserving such a small emittance. We begin by choosing feasible parameters for the needle radius $R = 5 \mu\text{m}$, field enhancement $\beta \approx 10$, and nominal photocathode field (without needle) $E_0 = 3 \text{ MV/m}$. We start by evaluating a set of simple shapes. We begin with a needle with a semicircular end-cap, and deform it intermediate steps to produce a square cap. The specific shapes evaluated by the field solver are shown in figure A.2.

For consistency, the fields for the fully round case were also evaluated with a (much

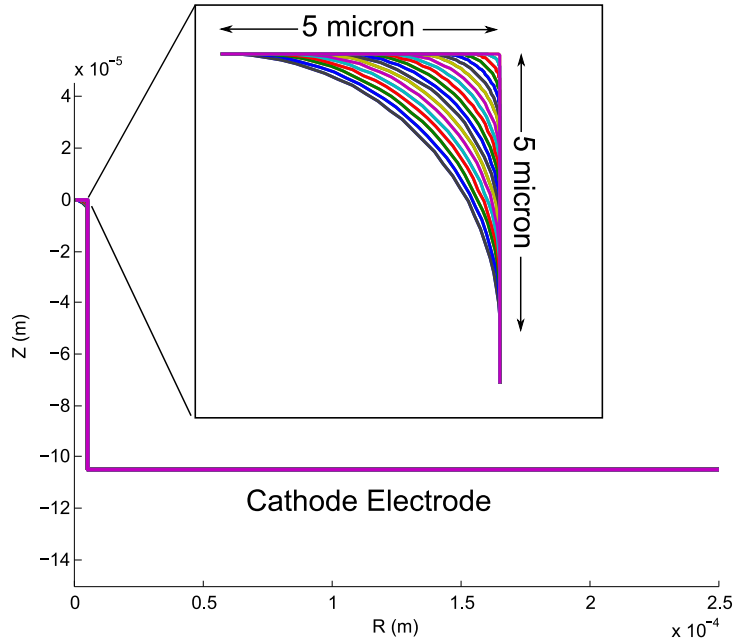


Figure A.2: The geometries evaluated by the solver. Inset: closeup on the endcap, where a semicircular cap is deformed in several intermediate geometries to produce a square cap.

slower) volume mesh solver, and 20 particles emitted were tracked with the General Particle Tracer [139] to a plane $z=10 \mu\text{m}$ away, where the particle trajectories have already been significantly deformed by the needle shape (see figure 7.2). The emittances here were found to agree with the boundary element solver and symplectic integrator to within 5%. This accuracy is more than adequate for the trends described below.

The emittances of each of the shapes drawn in figure A.2 are shown at various distances away from the needle tip in figure A.3. The geometries of the figure A.2 are parameterized by the length f of the flat segment and the tip apex divided by the tip radius. If $f/R = 0$ the tip is round, and if $f/R = 1$ the tip is fully square. Note that the emittances from round geometries are nearly two orders of magnitude larger than the intrinsic emittance. Furthermore, the emittances here are not yet converged, as seen by their dependence on the

evaluation plane distance. Emittance convergence in the nearly constant field of \mathbf{E}_2 generally occurs on the scale of millimeters.

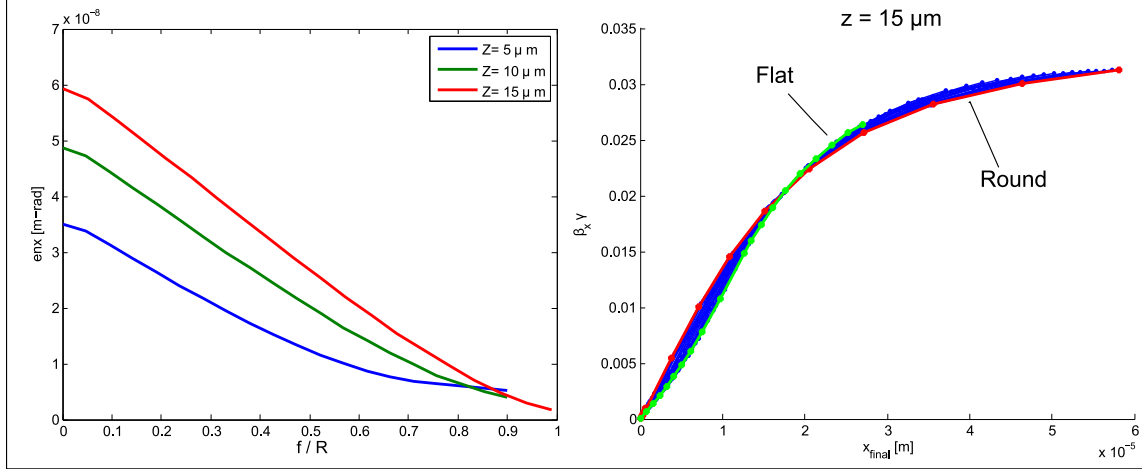


Figure A.3: Left: Emittance versus flatness of the tip. $f/R = 0$ is round, $f/R = 1$ is flat. Right: Phase spaces at $z = 15 \mu\text{m}$ used to calculate emittances, with fully flat and fully round cases highlighted.

The nonlinear curvature of the phase spaces indicate that the emittances may be improved by introducing “Pierce style” focusing at near the outer radial edge of the needle. A set of geometries with this feature are shown in figure A.4, where a flat portion of length $r = \sim 0.75R$ is terminated with an upward curve, reaching a sharp point at $r = R$. The height of the point at $r = R$ above $r = 0$ is labeled p , and these curves are parameterized below by the ratio p/R .

The emittances and phase spaces from these needles are shown in figure A.5. Each of the emittances in this case are two orders of magnitude smaller than the round case, approaching the nominal photocathode value estimated above, and there is a clear minimum of emittance for a certain p/R .

This focusing is not a perfect solution to the problem of emittance induced by the

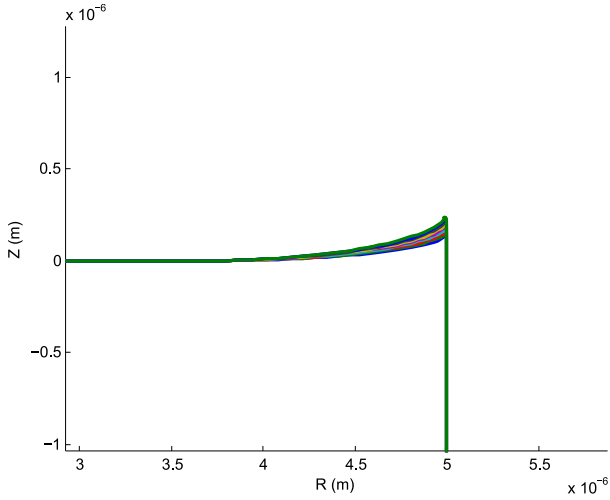


Figure A.4: A set of focusing needle geometries used to mitigate the phase space curvature of figure A.3.

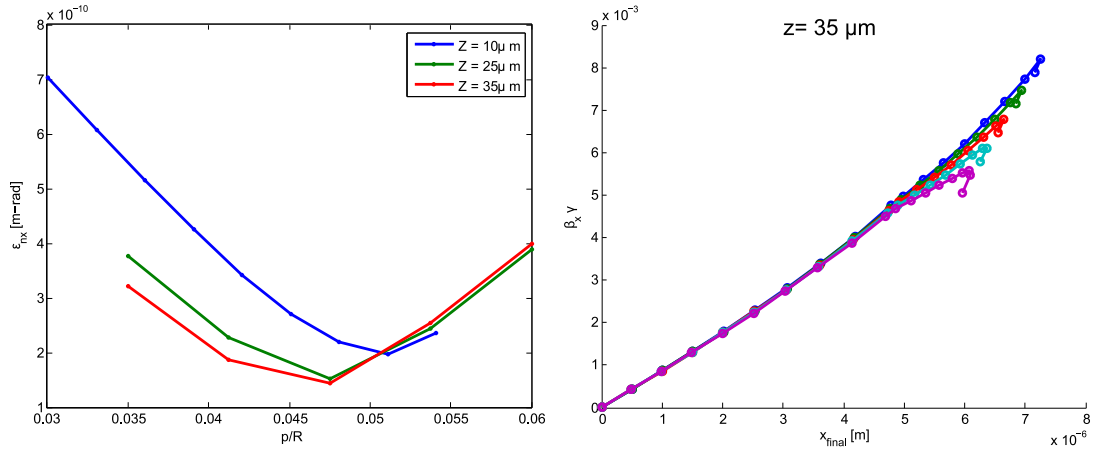


Figure A.5: Left: Emittance at different evaluation planes for focusing geometries.

needle shape. It introduces a very large field enhancement at the apex of the tip. This field enhancement as a function of r is shown in figure A.6.

It is clear that this geometry may have significant field emission. However, the field emission will be spatially separated from the central photoemitted beam. It is possible that a downstream aperture could truncate the field emission. Furthermore, it may be advantageous for emittance purposes to also truncate the outermost radial portion of the

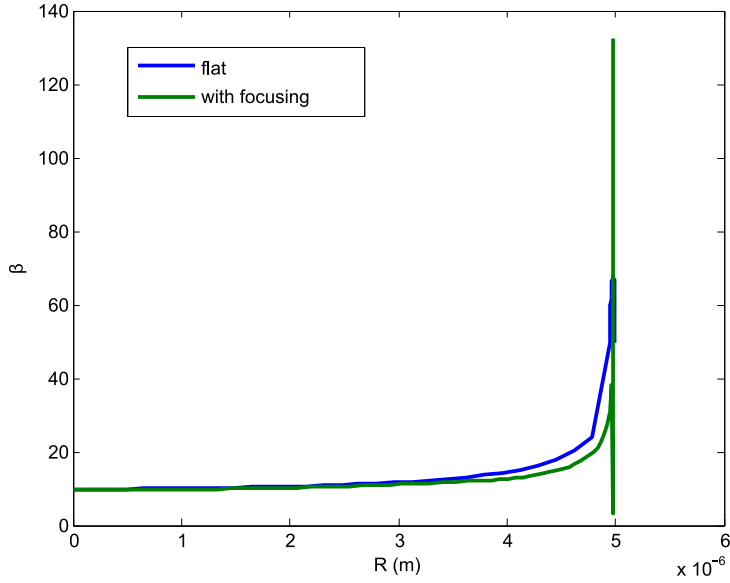


Figure A.6: Field enhancement parameter β along the surface of flat and focusing tip.

photoemitted beam, as the phase space is distorted there for all needle shapes (to varying degrees).

To get a sense of the final emittances after propagation through the gun, as well as the effect of truncation near the anode, both a flat geometry and the focusing case that minimizes the emittance in figure A.5 were tracked out to $z = 2$ cm. The beam here has an energy of roughly 60 kV, and the emittances are well converged. The outermost radial particles were then successively removed from the distribution, and the emittances were recalculated for these truncated cases. The results for varied truncation fractions are shown in figure A.7.

It is clear that if beam clipping is to be used to eliminate both field emission and photoemitted particles originating from the outer edge of the tip, than there may be no significant gain in using the focusing tip geometry, and that a flat emitter may be adequate.

This work does not capture a host of effects that will be present when photoemitting a

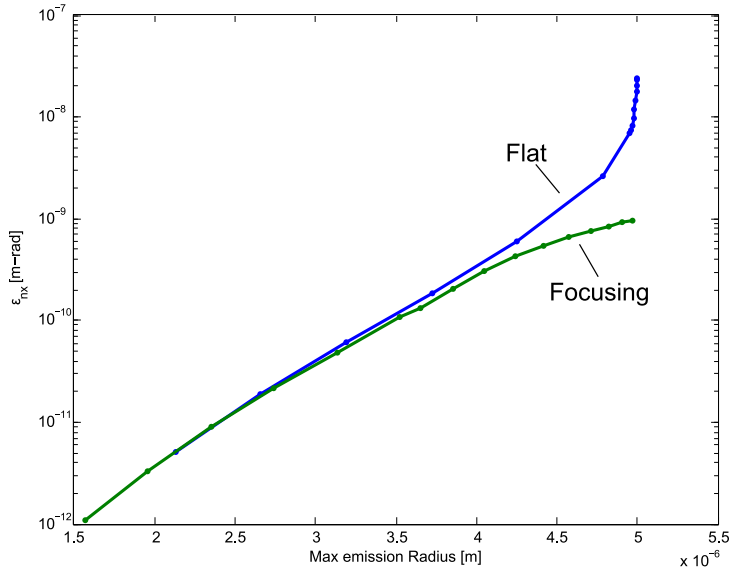


Figure A.7: Emittance at $z = 2$ cm for both flat and focusing cases, versus the maximum emission radius. The maximum emission radius is the radial position at the tip source above which particles are removed from the emittance calculation.

space charge dominated bunch from a needle photocathode. The effects of space charge, thermal emittance, and the heating of the tip due to the laser and emission process will further complicate the process of preserving the initial emittance. However, it is clear that even the shape of the tip itself can have a significant impact on the emittance from needle structures. However, with adequate needle shaping and beam clipping, it is possible to obtain sub-nm scale geometric emittances, which is the scale of the initial cathode emittance using cryo-cooled, μm -scale needle sizes and near threshold emission.

REFERENCES

- [1] P. Slade, *The Vacuum Interrupter: Theory, Design, and Application*. The Vacuum Interrupter: Theory, Design, and Application. Taylor & Francis, 2007.
<http://books.google.com/books?id=uJT4mENgMbQC>. ix, 12, 14, 15, 16, 30
- [2] I. V. Bazarov, A. Kim, M. N. Lakshmanan, and J. M. Maxson, “Comparison of dc and superconducting rf photoemission guns for high brightness high average current beam production,” *Phys. Rev. ST Accel. Beams* **14** no. 7, (Jul, 2011) .
<http://dx.doi.org/10.1103/PhysRevSTAB.14.072001>. ix, 16, 18, 24, 25, 37, 39, 40, 74
- [3] C. Prescott, W. Atwood, R. Cottrell, H. DeStaebler, E. L. Garwin, A. Gonidec, R. Miller, L. Rochester, T. Sato, D. Sherden, C. Sinclair, S. Stein, R. Taylor, J. Clendenin, V. Hughes, N. Sasao, K. Schler, M. Borghini, K. Lbelsmeyer, and W. Jentschke, “Parity non-conservation in inelastic electron scattering,” *Physics Letters B* **77** no. 3, (1978) 347 – 352.
<http://www.sciencedirect.com/science/article/pii/0370269378907220>. 1, 22
- [4] D. Pierce and F. Meier, “Photoemission of spin-polarized electrons from GaAs,” *Phys. Rev. B* **13** no. 12, (Jun, 1976) 54845500.
<http://dx.doi.org/10.1103/PhysRevB.13.5484>. 1
- [5] C. K. Sinclair, “High intensity polarized electron sources,” tech. rep., Stanford Linear Accelerator Center, CA (USA), 1980. 1
- [6] J. Clendenin, “Polarized electron sources,” in *Particle Accelerator Conference, 1995., Proceedings of the 1995*, vol. 2, pp. 877–881, IEEE. 1995. 1
- [7] M. Poelker and J. Grames, “Operation of cebaf photoguns at average beam current $> 1 \text{ mA}$,” *Polarized Sources and Targets - Proceedings of the 11th International Workshop* (2007) . http://dx.doi.org/10.1142/9789812770653_0024. 1
- [8] I. V. Bazarov, S. A. Belomestnykh, D. H. Bilderback, M. G. Billing, J. D. Brock, B. W. Buckley, S. S. Chapman, E. P. Chojnacki, Z. A. Conway, J. A. Crittenden, D. Dale, J. A. Dobbins, B. M. Dunham, R. D. Ehrlich, M. P. Ehrlichman, K. D. Finkelstein, E. Fontes, M. J. Forster, S. W. Gray, S. Greenwald, S. M. Gruner, C. Gulliford, D. L. Hartill, R. G. Helmke, G. H. Hoffstaetter, A. Kazimirov, R. P. Kaplan, S. S. Karkare, V. O. Kostroun, F. A. Laham, Y. H. Lau, Y. Li, X. Liu, M. U. Liepe, F. Loehl, L. Cultrera, T. Miyajima, C. E. Mayes, J. M. Maxson, A. Meseck, A. A. Mikhailichenko, D. Ouzounov, H. S. Padamsee, S. B. Peck, M. A. Pfeifer, S. E. Posen, P. G. Quigley, P. Revesz, D. H. Rice, U. Sae-Ueng, D. C. Sagan, J. O. Sears, V. D. Shemelin, C. K. Sinclair, D. M. Smilgies, E. N. Smith, K. W. Smolenski, C. Spethmann, C. Song, T. Tanabe, A. B. Temnykh, M. Tigner, N. R. A. Valles, V. G. Veshcherevich, Z. Wang, A. R. Woll, Y. Xie, and Z. Zhao, “Cornell energy recovery linac project definition design report,” tech. rep., Cornell University,

September, 2012. 1

- [9] S. Benson, J. Boyce, D. Douglas, P. Evtushenko, F. Hannon, C. Hernandez-Garcia, J. Klopf, G. Neil, M. D. Shinn, C. Tennant, *et al.*, “The vuv/ir/thz free electron laser program at jefferson lab,” *Nuclear Instruments and Methods in Physics Research Section A: Accelerators, Spectrometers, Detectors and Associated Equipment* **649** no. 1, (2011) 9–11. 1
- [10] P. Emma, R. Akre, J. Arthur, R. Bionta, C. Bostedt, J. Bozek, A. Brachmann, P. Bucksbaum, R. Coffee, F.-J. Decker, and et al., “First lasing and operation of an ngstrom-wavelength free-electron laser,” *Nature Photon* **4** no. 9, (Aug, 2010) 641647. <http://dx.doi.org/10.1038/nphoton.2010.176>. 1, 78
- [11] G. Neil, C. Bohn, S. Benson, G. Biallas, D. Douglas, H. Dylla, R. Evans, J. Fugitt, A. Grippo, J. Gubeli, and et al., “Sustained kilowatt lasing in a free-electron laser with same-cell energy recovery,” *Physical Review Letters* **84** no. 4, (Jan, 2000) 662665. <http://dx.doi.org/10.1103/PhysRevLett.84.662>. 78
- [12] M. Altarelli, R. Brinkmann, M. Chergui, W. Decking, B. Dobson, *et al.*, “Xfel: The european x-ray free-electron laser. technical design report,”. 1
- [13] M. Reiser, *Theory and Design of Charged Particle Beams*. Wiley Series in Beam Physics and Accelerator Technology. John Wiley & Sons, 2008.
<http://books.google.com/books?id=eegK9Mqgpi4C>. 2, 4, 5, 24, 94, 97, 100, 101, 108
- [14] K. Kubo and K. Oide, “Intrabeam scattering in electron storage rings,” *Phys. Rev. ST Accel. Beams* **4** no. 12, (Dec, 2001) .
<http://dx.doi.org/10.1103/PhysRevSTAB.4.124401>. 2
- [15] J. Fraser, R. Sheffield, and E. Gray, “A new high-brightness electron injector for free electron lasers driven by {RF} linacs,” *Nuclear Instruments and Methods in Physics Research Section A: Accelerators, Spectrometers, Detectors and Associated Equipment* **250** no. 12, (1986) 71 – 76.
<http://www.sciencedirect.com/science/article/pii/0168900286908624>. 2
- [16] D. H. Dowell, J. W. Lewellen, D. Nguyen, and R. Rimmer, “The status of normal conducting RF (ncrf) guns, a summary of the erl2005 workshop,” *Nuclear Instruments and Methods in Physics Research Section A: Accelerators, Spectrometers, Detectors and Associated Equipment* **557** no. 1, (Feb, 2006) 6168.
<http://dx.doi.org/10.1016/j.nima.2005.10.052>. 2
- [17] F. Sannibale, D. Filippetto, C. F. Papadopoulos, J. Staples, R. Wells, B. Bailey, K. Baptiste, J. Corlett, C. Cork, S. De Santis, S. Dimaggio, L. Doolittle, J. Doyle, J. Feng, D. Garcia Quintas, G. Huang, H. Huang, T. Kramasz, S. Kwiatkowski, R. Lellinger, V. Moroz, W. E. Norum, H. Padmore, C. Pappas, G. Portmann, T. Vecchione, M. Vinco, M. Zolotorev, and F. Zucca, “Advanced photoinjector experiment photogun commissioning results,” *Phys. Rev. ST Accel. Beams* **15** (Oct, 2012) 103501. <http://link.aps.org/doi/10.1103/PhysRevSTAB.15.103501>. 2

- [18] R. Rimmer, “A High-Gradient CW R Photo-Cathode Electron Gun for High Current Injectors,” in *21st Particle Accelerator Conference (PAC 05)*, p. 3049. 2005. 2
- [19] D. Janssen, H. Bttig, P. Evtushenko, M. Freitag, F. Gabriel, B. Hartmann, U. Lehnert, P. Michel, K. Mller, T. Quast, B. Reppe, A. Schamlott, C. Schneider, R. Schurig, J. Teichert, S. Konstantinov, S. Kruchkov, A. Kudryavtsev, O. Myskin, V. Petrov, A. Tribendis, V. Volkov, W. Sandner, I. Will, A. Matheisen, W. Moeller, M. Pekeler, P. Stein, and C. Haberstroh, “First operation of a superconducting rf-gun,” *Nuclear Instruments and Methods in Physics Research Section A: Accelerators, Spectrometers, Detectors and Associated Equipment* **507** no. 12, (2003) 314 – 317. <http://www.sciencedirect.com/science/article/pii/S0168900203009367>. Proceedings of the 24th International Free Electron Laser Conference and the 9th Users Workshop. 2
- [20] J. Kewischa, I. Ben-Zvi, T. Rao, A. Burrill, D. Pate, E. Wang, R. Todd, H. Bluem, D. Holmes, and T. Schultheiss, “The polarized srf gun experiment,” in *Workshop on Polarized Electron Sources and Polarimeters*, p. 1133, Citeseer. 2008. 2
- [21] J. Teichert, C. Schneider, P. Murcek, K. Möller, R. Hempel, P. Michel, H. Büttig, D. Janssen, A. Arnold, and U. Lehnert, “Measurement of the radio-frequency photo electron source with superconducting niobium cavity,” tech. rep., CARE, 2007. 2
- [22] J. Worster, “The brightness of electron beams,” *J. Phys. D: Appl. Phys.* **2** no. 3, (Mar, 1969) . <http://dx.doi.org/10.1088/0022-3727/2/3/321>. 3
- [23] M. J. Rhee, “Refined definition of the beam brightness,” *Phys. Fluids B* **4** no. 6, (1992) 1674. 3
- [24] Y. Batygin, “Conservation of space-charge-dominated beam emittance in a strong nonlinear focusing field,” *Phys. Rev. E* **53** no. 5, (May, 1996) 53585364. <http://dx.doi.org/10.1103/PhysRevE.53.5358>. 5
- [25] B. Carlsten, “Photoelectric injector design code,” *Proceedings of the 1989 IEEE Particle Accelerator Conference, . Accelerator Science and Technology* (1989) . <http://dx.doi.org/10.1109/PAC.1989.73157>. 5, 17
- [26] L. Serafini and J. B. Rosenzweig, “Envelope analysis of intense relativistic quasilaminar beams in rf photoinjectors:ma theory of emittance compensation,” *Phys. Rev. E* **55** no. 6, (Jun, 1997) . <http://dx.doi.org/10.1103/PhysRevE.55.7565>. 5, 17, 108
- [27] C. Gulliford, A. Bartnik, I. Bazarov, L. Cultrera, J. Dobbins, B. Dunham, F. Gonzalez, S. Karkare, H. Lee, H. Li, Y. Li, X. Liu, J. Maxson, C. Nguyen, K. Smolenski, and Z. Zhao, “Demonstration of low emittance in the cornell energy recovery linac injector prototype,” *Phys. Rev. ST Accel. Beams* **16** (Jul, 2013) 073401. <http://link.aps.org/doi/10.1103/PhysRevSTAB.16.073401>. 5, 25, 29, 40, 76
- [28] C. K. Sinclair, “DC photoemission electron guns as erl sources,” *Nuclear Instruments and Methods in Physics Research Section A: Accelerators, Spectrometers, Detectors*

and Associated Equipment **557** no. 1, (Feb, 2006) .

<http://dx.doi.org/10.1016/j.nima.2005.10.053>. 6, 111

- [29] D. H. Dowell and J. F. Schmerge, “Quantum efficiency and thermal emittance of metal photocathodes,” *Phys. Rev. ST Accel. Beams* **12** no. 7, (Jul, 2009) .
<http://dx.doi.org/10.1103/PhysRevSTAB.12.074201>. 6, 84, 85
- [30] I. Bazarov, D. Ouzounov, B. Dunham, S. Belomestnykh, Y. Li, X. Liu, R. Meller, J. Sikora, C. Sinclair, F. Wise, and et al., “Efficient temporal shaping of electron distributions for high-brightness photoemission electron guns,” *Phys. Rev. ST Accel. Beams* **11** no. 4, (Apr, 2008) .
<http://dx.doi.org/10.1103/PhysRevSTAB.11.040702>. 6, 44, 45, 61, 78, 80
- [31] I. Bazarov, L. Cultrera, A. Bartnik, B. Dunham, S. Karkare, Y. Li, X. Liu, J. Maxson, and W. Roussel, “Thermal emittance measurements of a cesium potassium antimonide photocathode,” *Appl. Phys. Lett.* **98** no. 22, (2011) 224101.
<http://dx.doi.org/10.1063/1.3596450>. 6, 78, 79
- [32] J. Grames, P. Adderley, J. Brittian, J. Clark, J. Hansknecht, D. Machie, M. Poelker, E. Pozdeyev, M. Stutzman, and K. Surles Law, “A biased anode to suppress ion back?bombardment in a dc high voltage photoelectron gun,” *AIP Conference Proceedings* **980** no. 1, (2008) 110–117. 6, 59
- [33] L. Cultrera, J. Maxson, I. Bazarov, S. Belomestnykh, J. Dobbins, B. Dunham, S. Karkare, R. Kaplan, V. Kostroun, Y. Li, X. Liu, F. Löhl, K. Smolenski, Z. Zhao, D. Rice, P. Quigley, M. Tigner, V. Veshcherevich, K. Finkelstein, D. Dale, and B. Pichler, “Photocathode behavior during high current running in the cornell energy recovery linac photoinjector,” *Phys. Rev. ST Accel. Beams* **14** (Dec, 2011) 120101.
<http://link.aps.org/doi/10.1103/PhysRevSTAB.14.120101>. 6
- [34] C. Sinclair, P. Adderley, B. Dunham, J. Hansknecht, P. Hartmann, M. Poelker, J. Price, P. Rutt, W. Schneider, and M. Steigerwald, “Development of a high average current polarized electron source with long cathode operational lifetime,” *Phys. Rev. ST Accel. Beams* **10** no. 2, (Feb, 2007) .
<http://dx.doi.org/10.1103/PhysRevSTAB.10.023501>. 6
- [35] “International Committee for Future Accelerators Beam Dynamics Newsletter, no 46,” 2008. 7
- [36] I. V. Bazarov, B. M. Dunham, and C. K. Sinclair, “Maximum achievable beam brightness from photoinjectors,” *Phys. Rev. Lett.* **102** (Mar, 2009) 104801.
<http://link.aps.org/doi/10.1103/PhysRevLett.102.104801>. 8, 24, 46, 59, 78, 89
- [37] D. Filippetto, P. Musumeci, M. Zolotorev, and G. Stupakov, “Maximum current density and beam brightness achievable by laser driven electron sources,” *Phys. Rev. ST Accel. Beams* **17** no. 2, (Feb, 2014) .
<http://dx.doi.org/10.1103/PhysRevSTAB.17.024201>. 8, 78
- [38] T. Takuma, O. Yamamoto, and S. Hamada, “Gases as a dielectric,” in *Gaseous*

Dielectrics X, pp. 195–204. Springer, 2004. 8

- [39] C. Hernandez-Garcia, T. Siggins, S. Benson, D. Bullard, H. Dylla, *et al.*, “A high average current DC GaAs photocathode gun for ERLs and FELs,” *Conf. Proc. C0505161* (2005) 3117. 8, 22, 35
- [40] M. Yamamoto, T. Nakanishi, S. Okumi, F. Furuta, M. Kuwahara, *et al.* in *Proceedings of the International Conference on Linear Colliders*. 2004. 9
- [41] P. A. Adderley, J. Clark, J. Grames, J. Hansknecht, K. Surles-Law, D. Machie, M. Poelker, M. L. Stutzman, and R. Suleiman, “Load-locked dc high voltage gaas photogun with an inverted-geometry ceramic insulator,” *Phys. Rev. ST Accel. Beams* **13** (Jan, 2010) 010101.
<http://link.aps.org/doi/10.1103/PhysRevSTAB.13.010101>. 9, 22
- [42] J. Shea, “Punchthrough of ceramic insulators,” *Annual Conference on Electrical Insulation and Dielectric Phenomena* (1990) .
<http://dx.doi.org/10.1109/CEIDP.1990.201380>. 11
- [43] R. Nagai, R. Hajima, N. Nishimori, T. Muto, M. Yamamoto, Y. Honda, T. Miyajima, H. Iijima, M. Kuriki, M. Kuwahara, S. Okumi, and T. Nakanishi, “High-voltage testing of a 500-kv dc photocathode electron gun,” *Review of Scientific Instruments* **81** no. 3, (2010) –. <http://scitation.aip.org/content/aip/journal/rsi/81/3/10.1063/1.3354980>. 11
- [44] N. Nishimori, R. Nagai, H. Iijima, Y. Honda, T. Muto, M. Kuriki, M. Yamamoto, S. Okumi, T. Nakanishi, and R. Hajima, “Development of an electron gun for an erl based light source in japan,” *AIP Conference Proceedings* **1149** no. 1, (2009) 1094–1098. 11
- [45] N. Nishimori, R. Nagai, S. Matsuba, R. Hajima, M. Yamamoto, Y. Honda, T. Miyajima, H. Iijima, M. Kuriki, and M. Kuwahara, “Experimental investigation of an optimum configuration for a high-voltage photoemission gun for operation at ≥ 500 kV,” *Phys. Rev. ST Accel. Beams* **17** (May, 2014) 053401.
<http://link.aps.org/doi/10.1103/PhysRevSTAB.17.053401>. 23, 34, 37
- [46] N. Nishimori, R. Nagai, S. Matsuba, R. Hajima, M. Yamamoto, T. Miyajima, Y. Honda, H. Iijima, M. Kuriki, and M. Kuwahara, “Generation of a 500-keV electron beam from a high voltage photoemission gun,” *Appl. Phys. Lett.* **102** no. 23, (2013) 234103. <http://dx.doi.org/10.1063/1.4811158>. 11, 37
- [47] R. Latham, *High Voltage Vacuum Insulation: Basic Concepts and Technological Practice*. Elsevier Science, 1995. 12, 14, 15, 30, 32
- [48] H. Chen, Y. Du, W. Gai, A. Grudiev, J. Hua, W. Huang, J. G. Power, E. E. Wisniewski, W. Wuensch, C. Tang, L. Yan, and Y. You, “Surface-emission studies in a high-field rf gun based on measurements of field emission and schottky-enabled photoemission,” *Phys. Rev. Lett.* **109** (Nov, 2012) 204802.
<http://link.aps.org/doi/10.1103/PhysRevLett.109.204802>.

- [49] R. Huang, D. Filippetto, F. Papadopoulos, C. H. Qian, F. Sannibale, and M. Zolotorev, “Dark current studies on a normal-conducting high-brightness very-high-frequency electron gun operating in continuous wave mode,” *Phys. Rev. ST Accel. Beams* **18** (Jan, 2015) 013401. <http://link.aps.org/doi/10.1103/PhysRevSTAB.18.013401>. 12
- [50] D. Swenson, A. Wu, E. Degenkolb, and Z. Insepov, “Gas cluster ion beam surface treatments for reducing field emission and breakdown of electrodes and srf cavities,” *Nuclear Instruments and Methods in Physics Research Section B: Beam Interactions with Materials and Atoms* **261** no. 1, (2007) 630–633. 13
- [51] I. Yamada, J. Matsuo, N. Toyoda, and A. Kirkpatrick, “Materials processing by gas cluster ion beams,” *Materials Science and Engineering: R: Reports* **34** no. 6, (2001) 231 – 295. <http://www.sciencedirect.com/science/article/pii/S0927796X01000341>. 13
- [52] H. Padamsee, *RF Superconductivity: Volume II: Science, Technology and Applications*. John Wiley & Sons, 2009. 13
- [53] V. Kukreja and K. Smolenski, “Field emission properties in the erl electron source.” Unpublished. 13
- [54] N. Nishimori, R. Nagai, S. Matsuba, R. Hajima, M. Yamamoto, Y. Honda, T. Miyajima, H. Iijima, M. Kuriki, and M. Kuwahara *Phys. Rev. ST Accel. Beams* **17** no. 5, (May, 2014) . <http://dx.doi.org/10.1103/PhysRevSTAB.17.053401>. 15
- [55] C. Gulliford, A. Bartnik, I. Bazarov, B. Dunham, and L. Cultrera, “Demonstration of cathode emittance dominated high bunch charge beams in a DC gun-based photoinjector,” *Appl. Phys. Lett.* **106** no. 9, (Mar, 2015) 094101. <http://dx.doi.org/10.1063/1.4913678>. 16, 44, 78, 82, 106, 112
- [56] I. Bazarov and C. Sinclair, “Multivariate optimization of a high brightness dc gun photoinjector,” *Phys. Rev. ST Accel. Beams* **8** no. 3, (Mar, 2005) . <http://dx.doi.org/10.1103/PhysRevSTAB.8.034202>. 18
- [57] J. Maxson, I. Bazarov, B. Dunham, J. Dobbins, X. Liu, and K. Smolenski, “Design, conditioning, and performance of a high voltage, high brightness dc photoelectron gun with variable gap,” *Review of Scientific Instruments* **85** no. 9, (Sep, 2014) 093306. <http://dx.doi.org/10.1063/1.4895641>. 21, 62, 69, 80
- [58] C. K. Sinclair, “{DC} photoemission electron guns as {ERL} sources,” *Nuclear Instruments and Methods in Physics Research Section A: Accelerators, Spectrometers, Detectors and Associated Equipment* **557** no. 1, (2006) 69 – 74. <http://www.sciencedirect.com/science/article/pii/S0168900205019753>. 22, 30
- [59] M. Merano, S. Collin, P. Renucci, M. Gatri, S. Sonderegger, A. Crottini, J. D. Ganire, and B. Deveaud, “High brightness picosecond electron gun,” *Review of Scientific Instruments* **76** no. 8, (2005) –. <http://dx.doi.org/10.1063/1.1863811>

//scitation.aip.org/content/aip/journal/rsi/76/8/10.1063/1.2008975. 22

- [60] J. A. Berger, J. T. Hogan, M. J. Greco, W. A. Schroeder, A. W. Nicholls, and N. D. Browning, “Dc photoelectron gun parameters for ultrafast electron microscopy,” *Microscopy and Microanalysis* **15** (8, 2009) 298–313.
http://journals.cambridge.org/article_S1431927609090266. 22
- [61] R. Nagai, R. Hajima, N. Nishimori, T. Muto, M. Yamamoto, Y. Honda, T. Miyajima, H. Iijima, M. Kuriki, M. Kuwahara, and et al., “High-voltage testing of a 500 kv dc photocathode electron gun,” *Review of Scientific Instruments* **81** no. 3, (2010) 033304.
<http://dx.doi.org/10.1063/1.3354980>. 23
- [62] J. Lewellen and N. Nishimori, “Report from wg1 dc guns,” *Proceedings of ERL’09, Cornell University, Ithaca NY* (2009) .
<https://accelconf.web.cern.ch/accelconf/ERL2009/papers/wg102.pdf>. 24
- [63] J. Li, Z. Yu, W. Shao, K. Zhang, Y. Gao, H. Yuan, H. Wang, K. Huang, Q. Chen, S. Yan, and S. Cai, “High current density m-type cathodes for vacuum electron devices,” *Applied Surface Science* **251** no. 14, (2005) 151 – 158. 24
- [64] M. Lakshmanan, I. Bazarov, and T. Miyajima, “Geometry optimization of dc and srf guns to maximize beam brightness,” *Proceedings of ERL’09, Cornell University, Ithaca NY* (2009) .
<https://accelconf.web.cern.ch/accelconf/ERL2009/papers/plt20.pdf>. 24
- [65] A. Valfells, D. W. Feldman, M. Virgo, P. G. OShea, and Y. Y. Lau, “Effects of pulse-length and emitter area on virtual cathode formation in electron guns,” *Physics of Plasmas (1994-present)* **9** no. 5, (2002) 2377–2382. <http://scitation.aip.org/content/aip/journal/pop/9/5/10.1063/1.1463065>. 24
- [66] K. Smolenski, I. Bazarov, B. Dunham, H. Li, Y. Li, X. Liu, D. Ouzounov, and C. Sinclair, “Design and performance of the cornell erl dc photoemission gun,” *AIP Conference Proceedings* **1149** no. 1, (2009) 1077–1083. <http://scitation.aip.org/content/aip/proceeding/aipcp/10.1063/1.3215596>. 25, 29
- [67] J. Maxson, I. Bazarov, B. Dunham, and K. Smolenski, “Optimization of DC Photogun Electrode Geometry,” *Proceedings of the 2011 Particle Accelerator Conference New York, NY, USA* (2011) 1945–1947.
<http://accelconf.web.cern.ch/AccelConf/PAC2011/papers/wep245.pdf>. 29
- [68] K. Flottman, “Astra: a space charge tracking algorithm.” DESY, 2000. 37
- [69] J. M. Maxson, A. C. Bartnik, and I. V. Bazarov, “Efficient and accurate laser shaping with liquid crystal spatial light modulators,” *Appl. Phys. Lett.* **105** no. 17, (Oct, 2014) 171109. <http://dx.doi.org/10.1063/1.4900835>. 44, 48, 60, 62, 64, 68
- [70] M. Ferrario, D. Alesini, A. Bacci, M. Bellaveglia, R. Boni, M. Boscolo, M. Castellano, L. Catani, E. Chiadroni, S. Cialdi, and et al., “Direct measurement of the double emittance minimum in the beam dynamics of the sparc high-brightness photoinjector,”

Physical Review Letters **99** no. 23, (Dec, 2007) .
<http://dx.doi.org/10.1103/PhysRevLett.99.234801>. 44

- [71] P. Musumeci, J. T. Moody, R. J. England, J. B. Rosenzweig, and T. Tran, “Experimental generation and characterization of uniformly filled ellipsoidal electron-beam distributions,” *Phys. Rev. Lett.* **100** (Jun, 2008) 244801.
<http://link.aps.org/doi/10.1103/PhysRevLett.100.244801>. 44, 45, 59
- [72] Y. Li, S. Chemerisov, and J. Lewellen, “Laser pulse shaping for generating uniform three-dimensional ellipsoidal electron beams,” *Phys. Rev. ST Accel. Beams* **12** (Feb, 2009) 020702. 44, 46, 59
- [73] A. Sharma, T. Tsang, and T. Rao, “Theoretical and experimental study of passive spatiotemporal shaping of picosecond laser pulses,” *Phys. Rev. ST Accel. Beams* **12** no. 3, (Mar, 2009) . <http://dx.doi.org/10.1103/PhysRevSTAB.12.033501>. 45, 60
- [74] E. Schonbrun, R. Piestun, P. Jordan, J. Cooper, K. Wulff, J. Courtial, and M. Padgett, “3d interferometric optical tweezers using a single spatial light modulator,” *Opt. Express* **13** no. 10, (May, 2005) 3777–3786.
<http://www.opticsexpress.org/abstract.cfm?URI=oe-13-10-3777>. 46
- [75] A. L. Gaunt and Z. Hadzibabic, “Robust digital holography for ultracold atom trapping,” *Scientific reports* **2** (2012) . 46, 47, 49, 50, 51, 54, 62
- [76] G. D. Bruce, J. Mayoh, G. Smirne, L. Torralbo-Campo, and D. Cassettari, “A smooth, holographically generated ring trap for the investigation of superfluidity in ultracold atoms,” *Physica Scripta* **2011** no. T143, (2011) 014008. 46, 51
- [77] M. Pasienski and B. DeMarco, “A high-accuracy algorithm for designing arbitrary holographic atom traps,” *Opt. Express* **16** no. 3, (Feb, 2008) 2176–2190. 46, 47, 49, 59, 62
- [78] F. Nogrette, H. Labuhn, S. Ravets, D. Barredo, L. Béguin, A. Vernier, T. Lahaye, and A. Browaeys, “Single-atom trapping in holographic 2d arrays of microtraps with arbitrary geometries,” *Phys. Rev. X* **4** (May, 2014) 021034.
- [79] L. Amico, D. Aghamalyan, F. Auksztol, H. Crepaz, R. Dumke, and L. C. Kwek, “Superfluid qubit systems with ring shaped optical lattices,” *Scientific reports* **4** (2014) . 46
- [80] V. Nikolenko, D. S. Peterka, R. Araya, A. Woodruff, and R. Yuste, “Spatial light modulator microscopy,” *Cold Spring Harbor Protocols* no. 12, (December, 2013) 1132–41. 46
- [81] G. Penco, M. Danailov, A. Demidovich, E. Allaria, G. De Ninno, S. Di Mitri, W. M. Fawley, E. Ferrari, L. Giannessi, and M. Trovó, “Experimental demonstration of electron longitudinal-phase-space linearization by shaping the photoinjector laser pulse,” *Phys. Rev. Lett.* **112** (Jan, 2014) 044801. 46
- [82] O. J. Luiten, S. B. van der Geer, M. J. de Loos, F. B. Kiewiet, and M. J. van der Wiel, “How to realize uniform three-dimensional ellipsoidal electron bunches,” *Phys.*

Rev. Lett. **93** (Aug, 2004) 094802. 46, 59

- [83] A. McCulloch, D. Sheludko, S. Saliba, S. Bell, M. Junker, K. Nugent, and R. Scholten, “Arbitrarily shaped high-coherence electron bunches from cold atoms,” *Nature Physics* **7** no. 10, (2011) 785–788. 46, 59
- [84] B. Claessens, S. van der Geer, G. Taban, E. Vredenbregt, and O. Luiten, “Ultracold electron source,” *Physical Review Letters* **95** no. 16, (Oct, 2005) . <http://dx.doi.org/10.1103/PhysRevLett.95.164801>. 46, 59, 86
- [85] F. Dickey and S. Holswade, *Laser Beam Shaping: Theory and Techniques*. Optical Science and Engineering. Taylor & Francis, 2000. 46, 55, 62
- [86] J. Liang, J. Rudolph N. Kohn, M. F. Becker, and D. J. Heinzen, “High-precision laser beam shaping using a binary-amplitude spatial light modulator,” *Appl. Opt.* **49** no. 8, (Mar, 2010) 1323–1330. <http://ao.osa.org/abstract.cfm?URI=ao-49-8-1323>. 46, 47, 61
- [87] D. Trypogeorgos, T. Harte, A. Bonnin, and C. Foot, “Precise shaping of laser light by an acousto-optic deflector,” *Opt. Express* **21** no. 21, (Oct, 2013) 24837–24846. 46
- [88] R. Gerchberg and W. Saxton, “Practical algorithm for determination of phase from image and diffraction plane pictures,” *Optik* **35** no. 2, (1972) 237. 47, 59
- [89] J. A. Davis, D. E. McNamara, D. M. Cottrell, and T. Sonehara, “Two-dimensional polarization encoding with a phase-only liquid-crystal spatial light modulator,” *Appl. Opt.* **39** no. 10, (Apr, 2000) 1549–1554. 47, 60, 62, 63
- [90] C. Ye, “Construction of an optical rotator using quarter-wave plates and an optical retarder,” *Optical Engineering* **34** no. 10, (1995) 3031–3035. 48, 60, 62, 63
- [91] V. Soifer, V. Kotlar, and L. Doskolovich, *Iterative Methods For Diffractive Optical Elements Computation*. Taylor & Francis, 1997. 49
- [92] B. Kress and P. Meyrueis, *Applied Digital Optics: From Micro-optics to Nanophotonics*. Wiley, 2009. 49, 51, 52, 62
- [93] G. Whyte and J. Courtial, “Experimental demonstration of holographic three-dimensional light shaping using a gerchbergsaxton algorithm,” *New Journal of Physics* **7** no. 1, (2005) 117. 49
- [94] P. Senthilkumaran, F. Wyrowski, and H. Schimmel, “Vortex stagnation problem in iterative fourier transform algorithms,” *Optics and Lasers in Engineering* **43** no. 1, (2005) 43 – 56. 49, 50
- [95] E. Ronzitti, M. Guillon, V. de Sars, and V. Emiliani, “Lcos nematic slm characterization and modeling for diffraction efficiency optimization, zero and ghost orders suppression,” *Opt. Express* **20** no. 16, (Jul, 2012) 17843–17855. 51
- [96] B. Apté, U. Efron, and E. Bahat-Treidel, “On the fringing-field effect in liquid-crystal beam-steering devices,” *Appl. Opt.* **43** no. 1, (Jan, 2004) 11–19.
- [97] V. Arrizn, E. Carren, and M. Testorf, “Implementation of fourier array illuminators

- using pixelated slm: efficiency limitations,” *Optics Communications* **160** no. 46, (1999) 207 – 213. 51
- [98] D. R. Scherer, C. N. Weiler, T. W. Neely, and B. P. Anderson, “Vortex formation by merging of multiple trapped bose-einstein condensates,” *Phys. Rev. Lett.* **98** (Mar, 2007) 110402. 54
- [99] W. Press, *Numerical Recipes 3rd Edition: The Art of Scientific Computing*. Cambridge University Press, 2007. 55
- [100] P. Revesz, A. Kazimirov, and I. Bazarov, “In situ visualization of thermal distortions of synchrotron radiation optics,” *Nuclear Instruments and Methods in Physics Research Section A: Accelerators, Spectrometers, Detectors and Associated Equipment* **576** no. 23, (2007) 422 – 429. 55
- [101] J. Maxson, H. Lee, A. C. Bartnik, J. Kiefer, and I. Bazarov, “Adaptive electron beam shaping using a photoemission gun and spatial light modulator,” *Phys. Rev. ST Accel. Beams* **18** no. 2, (Feb, 2015) . <http://dx.doi.org/10.1103/PhysRevSTAB.18.023401>. 58, 62
- [102] F. Zhou, A. Brachmann, P. Emma, S. Gilevich, and Z. Huang, “Impact of the spatial laser distribution on photocathode gun operation,” *Phys. Rev. ST Accel. Beams* **15** no. 9, (Sep, 2012) . <http://dx.doi.org/10.1103/PhysRevSTAB.15.090701>. 59
- [103] D. Y. Shchegolkov and E. I. Simakov, “Design of an emittance exchanger for production of special shapes of the electron beam current,” *Phys. Rev. ST Accel. Beams* **17** (Apr, 2014) 041301. 59
- [104] E. I. Simakov, B. E. Carlsten, and D. Y. Shchegolkov, “Possibility for ultra-bright electron beam acceleration in dielectric wakefield accelerators,” *AIP Conference Proceedings* **1507** no. 1, (2012) 634–638. 59
- [105] F. Matsui, S. Goriki, Y. Shimizu, H. Tomizawa, S. Kawato, and T. Kobayashi, “Genetic-algorithm-based method to optimize spatial profile utilizing characteristics of electrostatic actuator deformable mirror,” *Optical Review* **15** no. 3, (2008) 156–161. 59, 61
- [106] R. M. W. van Bijnen, C. Ravensbergen, D. J. Bakker, G. J. Dijk, S. J. J. M. F. Kokkelmans, and E. J. D. Vredenbregt, “Patterned Rydberg excitation and ionisation with a spatial light modulator,” *ArXiv e-prints* (July, 2014) , [arXiv:1407.6856 \[physics.atom-ph\]](https://arxiv.org/abs/1407.6856). 59
- [107] F. Wyrowski, “Diffractive optical elements: iterative calculation of quantized, blazed phase structures,” *J. Opt. Soc. Am. A* **7** no. 6, (Jun, 1990) 961–969. <http://josaa.osa.org/abstract.cfm?URI=josaa-7-6-961>. 59
- [108] B. C. Riddick, E. J. Montgomery, R. B. Fiorito, H. D. Zhang, A. G. Shkvarunets, Z. Pan, and S. A. Khan, “Photocathode quantum efficiency mapping at high resolution using a digital micromirror device,” *Phys. Rev. ST Accel. Beams* **16** no. 6, (Jun, 2013) . <http://dx.doi.org/10.1103/PhysRevSTAB.16.062802>. 61

- [109] H. D. Zhang, R. B. Fiorito, A. G. Shkvarunets, R. A. Kishek, and C. P. Welsch, “Beam halo imaging with a digital optical mask,” *Phys. Rev. ST Accel. Beams* **15** no. 7, (Jul, 2012) . <http://dx.doi.org/10.1103/PhysRevSTAB.15.072803>. 61
- [110] Z. Zhao, A. Bartnik, F. W. Wise, I. V. Bazarov, and B. M. Dunham, “High-power fiber lasers for photocathode electron injectors,” *Phys. Rev. ST Accel. Beams* **17** no. 5, (May, 2014) . <http://dx.doi.org/10.1103/PhysRevSTAB.17.053501>. 61
- [111] C. Mayes, I. Bazarov, S. Belomestnykh, D. Bilderback, M. Billing, J. Brock, E. Chojnacki, J. Crittenden, L. Cultrera, J. Dobbins, B. Dunham, *et al.*, “Cornell erl research and development,” Proceedings of 2011 Particle Accelerator Conference. 2011. 78
- [112] M. Altarelli, R. Brinkmann, M. Chergui, W. Decking, B. Dobson, *et al.*, “Xfel: The european x-ray free-electron laser. technical design report,” tech. rep., DESY, 2006. 78
- [113] M. Ferrario, D. Alesini, A. Bacci, M. Bellaveglia, R. Boni, M. Boscolo, M. Castellano, E. Chiadroni, A. Cianchi, L. Cultrera, and et al., “Experimental demonstration of emittance compensation with velocity bunching,” *Physical Review Letters* **104** no. 5, (Feb, 2010) . <http://dx.doi.org/10.1103/PhysRevLett.104.054801>. 78
- [114] T. Vecchione, I. Ben-Zvi, D. H. Dowell, J. Feng, T. Rao, J. Smedley, W. Wan, and H. A. Padmore, “A low emittance and high efficiency visible light photocathode for high brightness accelerator-based x-ray light sources,” *Appl. Phys. Lett.* **99** no. 3, (2011) 034103. <http://dx.doi.org/10.1063/1.3612916>. 78
- [115] L. Cultrera, S. Karkare, B. Lillard, A. Bartnik, I. Bazarov, B. Dunham, W. Schaff, and K. Smolenski, “Growth and characterization of rugged sodium potassium antimonide photocathodes for high brilliance photoinjector,” *Appl. Phys. Lett.* **103** no. 10, (2013) 103504. <http://dx.doi.org/10.1063/1.4820132>. 78, 79, 85
- [116] L. Cultrera, J. Maxson, I. Bazarov, S. Belomestnykh, J. Dobbins, B. Dunham, S. Karkare, R. Kaplan, V. Kostroun, Y. Li, and et al., “Photocathode behavior during high current running in the cornell energy recovery linac photoinjector,” *Phys. Rev. ST Accel. Beams* **14** no. 12, (Dec, 2011) .
<http://dx.doi.org/10.1103/PhysRevSTAB.14.120101>. 78
- [117] B. Dunham, J. Barley, A. Bartnik, I. Bazarov, L. Cultrera, J. Dobbins, G. Hoffstaetter, B. Johnson, R. Kaplan, S. Karkare, and et al., “Record high-average current from a high-brightness photoinjector,” *Appl. Phys. Lett.* **102** no. 3, (2013) 034105. <http://dx.doi.org/10.1063/1.4789395>. 78
- [118] W. Spicer, “Photoemissive, photoconductive, and optical absorption studies of alkali-antimony compounds,” *Phys. Rev.* **112** no. 1, (Oct, 1958) 114122.
<http://dx.doi.org/10.1103/PhysRev.112.114>. 78
- [119] L. Cultrera, S. Karkare, H. Lee, X. Liu, I. Bazarov, and B. Dunham, “Cold electron beams from cryo-cooled, alkali antimonide photocathodes.” submitted, 2014. 79, 111
- [120] T. Vecchione, D. Dowell, W. Wan, J. Feng, and H. Padmore, “Quantum efficiency

and transverse momentum from metals," Proceedings of FEL2013, New York, NY. 2013. 79

- [121] I. Bazarov, B. Dunham, C. Gulliford, Y. Li, X. Liu, C. Sinclair, K. Soong, and F. Hannon, "Benchmarking of 3D space charge codes using direct phase space measurements from photoemission high voltage dc gun," *Phys. Rev. ST Accel. Beams* **11** no. 10, (Oct, 2008) . <http://dx.doi.org/10.1103/PhysRevSTAB.11.100703>. 81
- [122] W. J. Engelen, M. A. van der Heijden, D. J. Bakker, E. J. D. Vredenbregt, and O. J. Luiten, "High-coherence electron bunches produced by femtosecond photoionization," *Nature Communications* **4** (Apr, 2013) 1693.
<http://dx.doi.org/10.1038/ncomms2700>. 86
- [123] J. M. Maxson, I. V. Bazarov, W. Wan, H. A. Padmore, and C. E. Coleman-Smith, "Fundamental photoemission brightness limit from disorder induced heating," *New Journal of Physics* **15** no. 10, (2013) 103024.
<http://stacks.iop.org/1367-2630/15/i=10/a=103024>. 86, 87
- [124] A. J. McCulloch, D. V. Sheludko, M. Junker, and R. E. Scholten, "High-coherence picosecond electron bunches from cold atoms," *Nature Communications* **4** (Apr, 2013) 1692. <http://dx.doi.org/10.1038/ncomms2699>. 86
- [125] S. D. Saliba, C. T. Putkunz, D. V. Sheludko, A. J. McCulloch, K. A. Nugent, and R. E. Scholten, "Spatial coherence of electron bunches extracted from an arbitrarily shaped cold atom electron source," *Optics Express* **20** no. 4, (2012) 3967.
<http://dx.doi.org/10.1364/OE.20.003967>.
- [126] W. Engelen, E. Smakman, D. Bakker, O. Luiten, and E. Vredenbregt, "Effective temperature of an ultracold electron source based on near-threshold photoionization," *Ultramicroscopy* **136** (Jan, 2014) .
<http://dx.doi.org/10.1016/j.ultramic.2013.07.017>. 86
- [127] R. K. Li and P. Musumeci, "Single-shot mev transmission electron microscopy with picosecond temporal resolution," *Physical Review Applied* **2** no. 2, (Aug, 2014) .
<http://dx.doi.org/10.1103/PhysRevApplied.2.024003>. 86
- [128] S. Pastuszka, D. Kratzmann, D. Schwalm, A. Wolf, and A. S. Terekhov, "Transverse energy spread of photoelectrons emitted from gaas photocathodes with negative electron affinity," *Applied Physics Letters* **71** no. 20, (1997) 2967–2969.
<http://link.aip.org/link/?APL/71/2967/1>. 90
- [129] Z. Liu, Y. Sun, P. Pianetta, and R. F. W. Pease, "Narrow cone emission from negative electron affinity photocathodes," vol. 23, pp. 2758–2762. AVS, 2005.
<http://link.aip.org/link/?JVB/23/2758/1>. 90, 91
- [130] G. Taban, M. P. Reijnders, B. Fleskens, S. B. van der Geer, O. J. Luiten, and E. J. D. Vredenbregt, "Ultracold electron source for single-shot diffraction studies," *EPL (Europhysics Letters)* **91** no. 4, (2010) 46004.
<http://stacks.iop.org/0295-5075/91/i=4/a=46004>. 90

- [131] G. Jansen, *Coulomb interactions in particle beams*. Advances in electronics and electron physics: Supplement. Academic Press, 1990. 92, 94, 95
- [132] G. A. Massey, M. D. Jones, and B. P. Plummer, “Space-charge aberrations in the photoelectron microscope,” *Journal of Applied Physics* **52** no. 6, (1981) 3780–3786. <http://link.aip.org/link/?JAP/52/3780/1>. 94
- [133] S. G. Brush, H. L. Sahlin, and E. Teller, “Monte carlo study of a one-component plasma. i,” *The Journal of Chemical Physics* **45** no. 6, (1966) 2102–2118. <http://link.aip.org/link/?JCP/45/2102/1>. 95
- [134] M. Lyon and S. D. Bergeson, “The influence of electron screening on disorder-induced heating,” *Journal of Physics B: Atomic, Molecular and Optical Physics* **44** no. 18, (2011) 184014. <http://stacks.iop.org/0953-4075/44/i=18/a=184014>. 96
- [135] Y. C. Chen, C. E. Simien, S. Laha, P. Gupta, Y. N. Martinez, P. G. Mickelson, S. B. Nagel, and T. C. Killian, “Electron screening and kinetic-energy oscillations in a strongly coupled plasma,” *Phys. Rev. Lett.* **93** (Dec, 2004) 265003. <http://link.aps.org/doi/10.1103/PhysRevLett.93.265003>. 96, 100
- [136] M. S. Murillo, “Using fermi statistics to create strongly coupled ion plasmas in atom traps,” *Phys. Rev. Lett.* **87** (Aug, 2001) 115003. <http://link.aps.org/doi/10.1103/PhysRevLett.87.115003>. 96, 97
- [137] D. H. E. Dubin and T. M. O’Neil, “Trapped nonneutral plasmas, liquids, and crystals (the thermal equilibrium states),” *Rev. Mod. Phys.* **71** (Jan, 1999) 87–172. <http://link.aps.org/doi/10.1103/RevModPhys.71.87>. 96, 97
- [138] B. Jeon, J. D. Kress, L. A. Collins, N. Grnbech-Jensen, B. Jeon, J. D. Kress, L. A. Collins, and N. Grnbech-Jensen, “Parallel tree code for two-component ultracold plasma analysis,” *Computer Physics Communications* **178** no. 4, (2008) 272 – 279. <http://www.sciencedirect.com/science/article/pii/S0010465507004171>. 98
- [139] “Pulsar physics, general particle tracer v. 3.10.” <http://www.pulsar.nl/gpt/>. 98, 119
- [140] J. Barnes, “Treecode guide, <http://www.ifa.hawaii.edu/~barnes/treecode/treeguide.html>,” Feb., 2001. 98
- [141] J. Barnes and P. Hut, “A hierarchical $O(N \log N)$ force-calculation algorithm,” *Nature* **324** no. 6096, (Dec., 1986) 446–449. <http://dx.doi.org/10.1038/324446a0>. 99
- [142] T. Pohl, T. Pattard, and J. M. Rost, “Relaxation to nonequilibrium in expanding ultracold neutral plasmas,” *Phys. Rev. Lett.* **94** (May, 2005) 205003. <http://link.aps.org/doi/10.1103/PhysRevLett.94.205003>. 102
- [143] M. S. Murillo, “Ultrafast dynamics of strongly coupled plasmas,” *Phys. Rev. Lett.* **96** (Apr, 2006) 165001. <http://link.aps.org/doi/10.1103/PhysRevLett.96.165001>. 102
- [144] E. M. Dianov, “Bismuth-doped optical fibers: a challenging active medium for

- near-IR lasers and optical amplifiers,” *Light Sci Appl* **1** no. 5, (May, 2012) e12. <http://dx.doi.org/10.1038/lsa.2012.12>. 106
- [145] R. Ganter, R. Bakker, C. Gough, S. C. Leemann, M. Paraliev, M. Pedrozzi, F. Le Pimpec, V. Schlott, L. Rivkin, and A. Wrulich, “Laser-photofield emission from needle cathodes for low-emittance electron beams,” *Physical Review Letters* **100** no. 6, (Feb, 2008) . <http://dx.doi.org/10.1103/PhysRevLett.100.064801>. 109
- [146] A. Mustonen, V. Guzenko, C. Spreu, T. Feurer, and S. Tsujino, “High-density metallic nano-emitter arrays and their field emission characteristics,” *Nanotechnology* **25** no. 8, (Feb, 2014) 085203. <http://dx.doi.org/10.1088/0957-4484/25/8/085203>. 110
- [147] C. Gulliford and A. Bartnik, “Operational experience with nanocoulomb bunch charges in the cornell photoinjector,” *Physical Review Special Topics: Accelerators and Beams, submitted* . 112
- [148] K. L. Jensen, Y. Y. Lau, D. W. Feldman, and P. G. OShea, “Electron emission contributions to dark current and its relation to microscopic field enhancement and heating in accelerator structures,” *Phys. Rev. ST Accel. Beams* **11** no. 8, (Aug, 2008) . <http://dx.doi.org/10.1103/PhysRevSTAB.11.081001>. 114
- [149] R. L. Hartman, “Use of boundary element methods in field emission computations,” *J. Vac. Sci. Technol. B* **12** no. 2, (Mar, 1994) 754. <http://dx.doi.org/10.1116/1.587385>. 115, 117